Are Cool Roofs Really Cool?
A Predictive Regression Model for Buildings on Auburn University's Campus

by

Seth Alexander Greer

A thesis submitted to the Graduate Faculty of
Auburn University
in partial fulfillment of the
requirements for the Degree of
Master of Science in Geography

Auburn, Alabama
December 16, 2017

Keywords: Remote Sensing, GIS, Regression Analysis, Geoengineering

Approved by

Chandana Mitra, Chair Associate Professor of Geography
Christopher G. Burton, Assistant Professor of Geography
Duha T. Altindag, Assistant Professor of Economics

Abstract

The natural environment has experienced many transformations into rapidly expanding urban areas. The use of concrete and asphalt has had direct impacts on the urban environment such as land-surface temperature (LST) and atmospheric dynamics. These changes to the climatic variables have long-term and short-term consequences. In this study, the campus of Auburn University is used to accurately measure LST, solar irradiance, and albedo using remotely sensed images and geographic models. In order to determine the effect that this will have on energy use, a statistical model is built to accurately show any relationships among the changes from the natural environment and the urban environment and future impacts that may occur as a result. By establishing the statistical relationships that exist, it will be possible to apply an Urban Heat Island mitigation strategy through the use of installing cool roofs, where albedo can be measured to show factors towards cooling.

Keywords: LST, Auburn-Alabama, Albedo, NDVI, Remote Sensing, Urban Heat Island, Reflectance, LSE, Solar Irradiance, Linear Regression, Ordinary Least Square, Energy Demand, Cool Roofs, UHI Mitigation Strategy, Geoengineering, Climate Change

Acknowledgements

This research would not have been possible without the help of many individuals. As such I would like to give my thanks to all those who have been a part of this journey and have helped bring to pass finalization of data, methods, discussions, and many other opportunities. First I would like to thank the Department of Geoscience and the David W. Icenogle Student Travel Grant, in addition to Dr. Chandana Mitra and Dr. Li Dong, for the financial assistance that they have all provided, without their support this would not have been possible. I would like to thank the staff of the department for the tremendous amount of help that they were able to provide me (Ms. Delaine Tease, Ms. Audrey Hollis). I would like to thank all of the GTAs in the department for the excellent brainstorming discussions we had and for the excellent time spent together. To my committee, I am very grateful to Dr. Burton for our excellent discussions on spatial analysis and his willingness to always work with me on new topics. I wish to thank Dr. Altindag for his help with transforming this research, in addition to his ability to translate regression models. I would again like to thank Dr. Mitra for all of her excellent feedback and support all along the way. I appreciate your courage for trusting me and always being there when it is most needed. Finally, I wish to thank my patient and caring wife for her always being there and understanding.

Table of Contents

List of Tables

List of Figures

List of Abbreviations

AICc	Akaike’s Information Criterion
AU	Auburn University
BRDF	Bidirectional Reflectance Distribution Function
C	Celsius
CRS	Coordinate Reference System
DEM	Digital Elevation Model
DSM	Digital Surface Model
EPSG	European Petroleum Survey Group
ESRI	Environmental Systems Research Institute
ETM+	Enhanced Thematic Mapper Plus
F	Fahrenheit
GHGs	Green House Gases
GIS	Geographic Information System
GRASS	Geographic Resources Analysis Support System
GWR	Geographic Weighted Regression
IDW	Inverse Distance Weighting
LiDAR	Light Detection and Ranging
LSE	Land Surface Emissivity
LST	Land Surface Temperature

LULCC	Land Use and Land Cover Change
MODIS	Moderate Resolution Imaging Spectroradiometer
NASA	National Aeronautics and Space Administration
NDVI	Normalized Difference Vegetation Index
OLI	Operational Land Imager
OLS	Ordinary Least Squares
QGIS	Quantum GIS
RMSE	Root Mean Square Error
RS	Remote Sensing
SAGA	System for Automated Geoscientific Analyses
SMARTS	Simple Model of the Atmospheric Radiative Transfer of Sunshine
SR	Surface Reflectance
TIRS	Thermal Infrared Sensor
TM	Thematic Mapper
TOA	Top of Atmosphere Reflectance
UHII	Urban Heat Island Intensity
USGS	United States Geological Survey
UTM	Universal Transverse Mercator
VIF	Variance Inflation Factor
WRS	World Reference System

Chapter 1. Introduction

The land use/land cover changes (LULCC) of the natural surfaces to concrete structures have given rise to variability in land surface temperature, atmospheric humidity, and energy usage in the urban environment. This intensification of anthropogenic effect may be mitigated from geoengineering applications such as developing methods for land surfaces to reflect more of the incoming solar radiation. This application of direct solar reflectance can further be applied onto the rooftops of urban buildings, thus effectively lowering the absorbed heat that would otherwise occur. By analyzing the relational effects between the urban environment and the natural climate, such as the reflective properties of rooftops in Auburn's campus, a model can be constructed that can be applied to individual buildings in regional southern climates. The primary goal of this research is to develop a predictive model that can effectively be used for making buildings more energy efficient. A secondary goal was further developed which proposes an empirical overview of the adoption of calculating Albedo values in regards to Landsat 8 OLI images. Specifically, this research pursues the following research objectives.

1. Successfully measure the LST, Albedo, & Incoming Solar Insolation of Auburn University campus buildings using remotely processed images for the summer day of July 28th, 2015.
2. Utilize a GIS platform, such as QGIS (http://www.qgis.org/en/site/), to interpret remotely sensed data in order to quantify meaningful geographic results, with the successful use of image resampling, and shapefile analysis.

3. Finalize meaningful results of the effects of climate variables, such as were discovered using Remotely Sensed techniques, to overlay a predictive statistical model in order to interpret the energy use relationship of Auburn University’s campus buildings.

The objectives of this study were achieved through the collection and analysis of land-surface temperature, albedo, solar irradiance, and energy consumption, which were used as the inputs for a regression analysis over the campus of Auburn University, by using 97 physically and spatially diverse buildings’ rooftops.

1.1 Thesis Structure

The structure of this thesis adopts an approach that presents an accessible method for peer review research. Chapter 1 begins with an introduction to the environment that this research takes place and why it might be a worthwhile endeavor to pursue such research. Chapter 1 also discusses the importance of the study area chosen and why the date of the study area should be considered. A brief introduction to the methodological approach to research questions along with the data sources as well. The goal of this chapter is to help the reader become familiar with a broad overview of the thesis structure as to support cognitive recognition when reading the future chapters.

Chapter 2 is used as a key introduction on much of the prerequisite background information required for the successful understanding of the research employed. Many of the topics that are studied are explained in great detail in Chapter 2, as well as key ideas and concepts that apply to the research in this study. It is strongly encouraged that a solid foundation in chapter 2 is attained before reading the following chapters.

Chapter 3 is detailed with the technical nature of the methodology of the research undertaken. It is in this chapter that a detailed explanation is created that allows for the greater understanding of the scientific knowledge required to understand much of the physical phenomena that occur. This chapter discusses the scientific methods used in order to calculate LST with remotely sensed images. After the discussion on LST, the next part details the developmental method for estimating Albedo in addition to providing statistical evidence for the chosen method. The final section of chapter 3 explains the processes for the model used to simulate the incoming solar radiation for the study.

Chapter 4 acts as an extension of the methods employed in chapter 3. It is in chapter 4 where the statistical interpretations are connected to the data created from chapter 3. This chapter sets up the final results and how they are significant to this study. Chapter 4 is the binding chapter that helps culminates all the deliverables from previous research questions.

Chapter 5 contains the conclusive comments and discusses the meaningful results from chapter 4. It is here, where suggestions and future directions are mentioned.

1.2 Study Area

The campus buildings of Auburn University were chosen as the study area for this research (See figure below). By choosing Auburn University, this research benefitted tremendously from the open availability of energy data, which was recorded by Auburn University's facilities management. Ninety-seven buildings were selected to study for this research (Appendix 1). The selection of these buildings includes diverse building characteristics, such as age and square footage of the buildings, geographic location, and the type of building. It can be deduced that smaller buildings would benefit more from cool roofs due to the proportional size of its roof in relation to the rest of the building (Bozonnet *et al.* 2011). Additionally, buildings with more active populations, where body temperature adds to the thermal equilibrium balance of the environment, may benefit less since there is an additional origin of heat energy being added into the system (Stolwijk 1980). Geographic properties also can play a large role in the intermittency of heat energy, for example, buildings that are further away from the urban center areas might not benefit as much as those that remain in the urban center, due to the thermal geometric properties, such as heat becoming trapped from the walls of other buildings, related to UHII (King *et al.* 1961). A geographic weighted regression (Brunsdon *et al.* 1996) can be used to indicate whether such geographic differences exists. With these considerations, 97 spatially separated buildings were chosen on Auburn University's campus, which all include energy demand data for cooling.

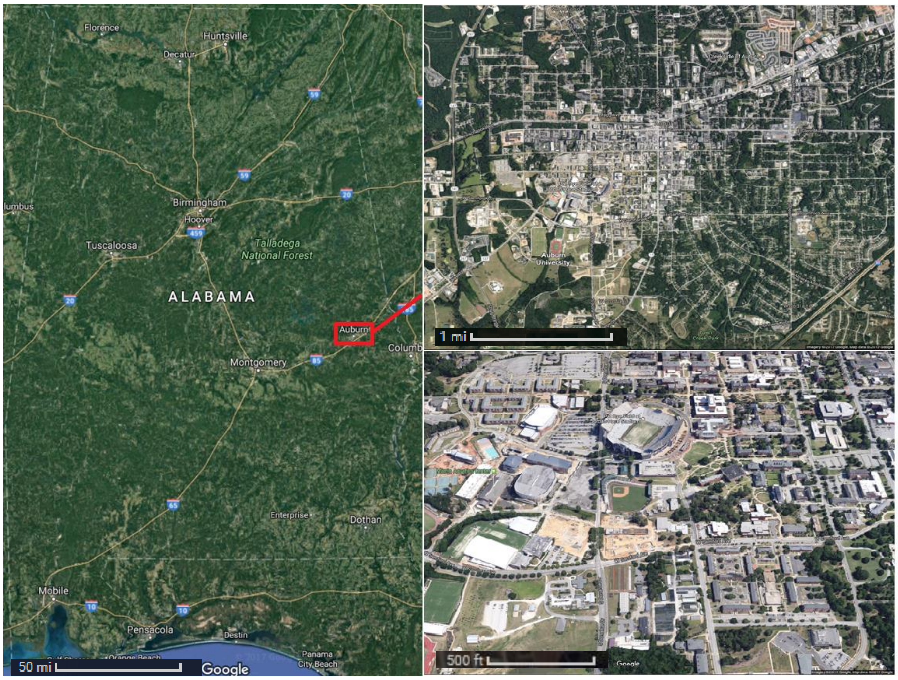

Figure 1: The study area includes the central campus of Auburn University, with several spatially and variable diverse building characteristics (Google Maps 2017).

1.3 The Date of Study

The day of July 28th, 2015, was an important date for several reasons. The first reason was to obtain a valid approximation of an average Auburn summer day, so that ideal climate conditions are being accurately modeled. According to weather station data, this date matches well with the expected average temperature of the Month. The monthly average mean temperature was 81 degrees F, with a high of 91 degrees F and a low of 72 degrees F. The average monthly dew point for July was at 70 degrees F. For 28th July 2015, the mean temperature was 86 degrees F, with a high of 97 degrees F and a low of 75 degrees F. The dew point for this date was 71 degrees F. This was a record high of temperature tying with the 1981 high of the same 97 degrees F high. By selecting this date, it was possible to understand in a best-case scenario if cool roofs could be used as an effective mitigation strategy against UHII effects. If it was determined from a hot day during July that cool roofs are effective mitigation strategies, then further analysis could be conducted for the wintertime, when there would be a wintertime heating penalty (Akbari *et al.* 2001).

A second reason was to obtain a cloud-free Landsat 8 image. The state of Alabama is classified as humid subtropical (Cfa) under the Köppen-Geiger climate classification (Kotteck *et al.* 2006) (See figure below). The humid subtropical region experiences warm temperatures while being fully humid and having hot summers. Thunderstorms and heavy cloud developments can occur throughout the year in this climate, however, the most common occurrence of such events tend to be during the summer months. This makes the entire state of Alabama a difficult area to obtain remotely sensed images in general due to the lacking of cloud-free days. It was determined from USGS EarthExplorer website, which lists the cloud cover percentage of each image, that this date was the most cloud-free day that remained suitable for study.

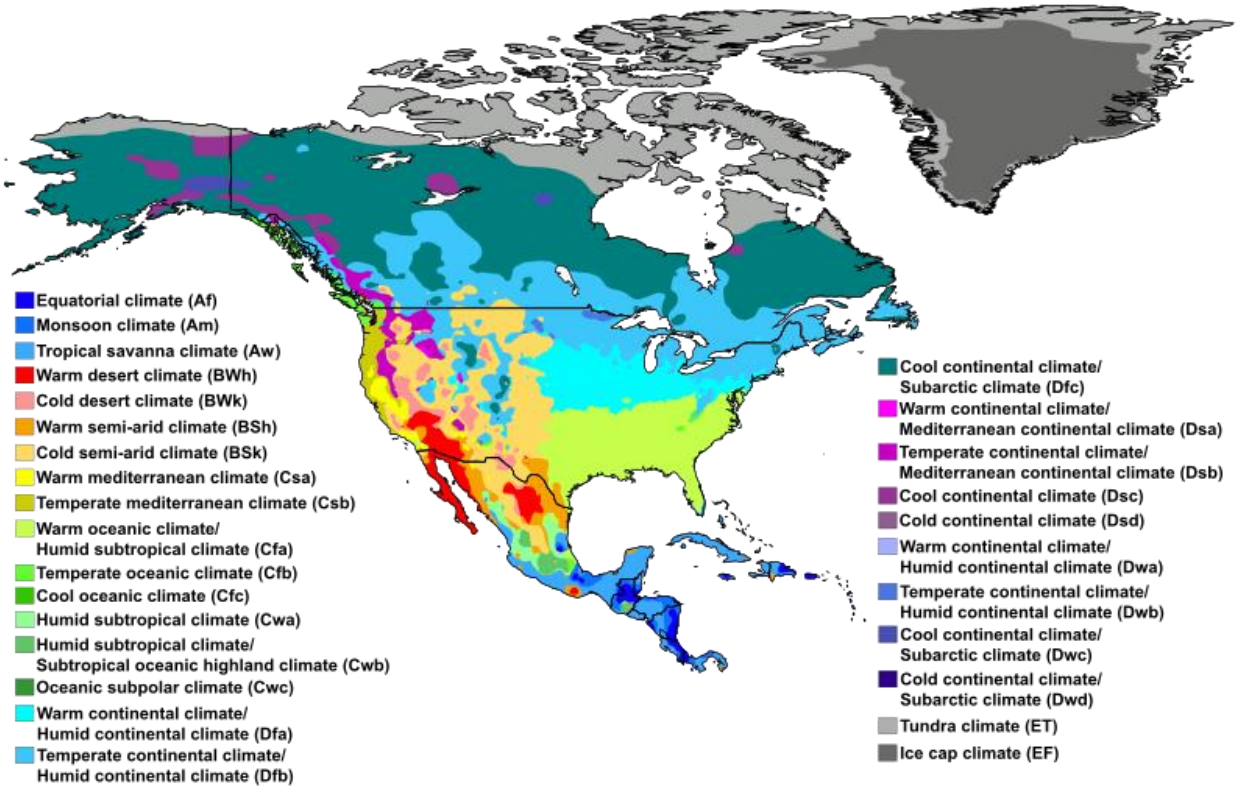

Figure 2: This map details the Köppen climate classification of North America. Note that Alabama, including the entirety of the Southeast Region of the US, is classified as a humid subtropical climate (Cfa) (Peel *et al.* 2007).

1.4 Methodology

There are a number of different methodologies that have been applied for this study. Data collection was derived from both primary and secondary sources. Geographic information systems (GIS) for spatial data processing had to be employed over the study area of Auburn University’s campus. In order to calculate incoming solar irradiance, an existing model developed by physical geographers has been used (Hofierka *et al.* 2002) within a dedicated GIS framework. These cumulative methods also included in the use of a built predictive model, which used a regression analysis, in order to be able to validate the application for the data values from this study.

1.5 Data collection

In order to complete the primary objectives of this study remotely sensed imagery was initially used. The first set of images was collected from open access datasets available from the USGS EarthExplorer website (https://earthexplorer.usgs.gov/). As mentioned in the previous section, in order to accurately determine LST values cloud-free images were needed during the day of July 28th, 2015 from NASA's Landsat satellite. The satellite had an overpass time of 16:12:46 GMT (11:12 A.M.) with the WRS path of 19 and a WRS row of 38. The cloud cover was calculated at 4.52% of the total image.

Airborne LiDAR data was obtained from the municipal city of Auburn for the study time period, which was used to model elevation and surface terrain properties as well as solar insolation. This was given as a raster file which was compatible with the use of the GIS when processing the solar irradiance model.

Table 1: Data Sources and Uses

Datasets	Data source	Date	Detail	Description
Landsat 8 OLI Landsat Archive Collection 1 Level – 1 / L8 OLI/TIRS	USGS EarthExplorer	7.28.2015	The resolution for bands 1 – 9, excluding 7 are 30 meters. For thermal bands 10 & 11, the original resolution is 100 meters, but are resampled to 30 meters.	Image LST Albedo NDVI
Google Earth/ OpenStreetMap	Google/ OpenStreetFoundation	Same as above	Natural/True color image, < 3m	Image Classification
Auburn Map Shapefile	Auburn University – Office of the University Architect	Same as above	1:100,000	Classification Spatial Statistics
Auburn Energy Management	Auburn Facilities	Same as above	Excel	Classification Spatial Statistics
LiDAR	Auburn Municipality	1.1.2015	<3m spatial resolution	DSM Solar Irradiance

The fulfillment of the second objective in this study was accomplished through the use of polygon shapefiles for the buildings that were being investigated. These shapefiles were obtained through Auburn's office of the University Architect, which allowed building information to be further spatially analyzed. This task was accomplished through Quantum GIS (QGIS) with the added data from the web service of the OpenStreetMap Foundation and Google Maps, which were both used as spatial references to ensure accuracy.

Additionally, Auburn University's energy management office provided energy data for all buildings being studied on campus. Auburn University's campus buildings have energy meters installed that collect the energy usage for heating and cooling. This data was in an Excel file format and had to be reorganized in order to isolate the necessary variables of the study so that it could be used for GIS processing (See appendix). The variables of the energy data include the buildings' names, types, energy consumption due to heating, energy consumption due to cooling, and energy prices (See appendix).

The third and final objective was fulfilled with the use of the statistical toolbox application within ArcMap for the use by the Environmental Systems Research Institute, also known as ESRI, from the desktop suite of ArcGIS. Within ArcMap, previously processed data was further configured into the development suite of ArcGIS to create statistical reports and new shapefiles from within the applied toolbox, which allowed for the newly created data to be easily interpreted to accomplish this studies research goals.

My research will contribute to the broader scientific knowledge by modeling impacts caused from cool roofs within an urban area of the Southeastern region of the US. It will use real-time energy data, as well as much higher resolution data and models than the global models used in previous studies. The benefits from a local scale study such as this is that area specific details can become derived to suitable areas. Such an instance is in the case of having a study area in the climate classification of Cfa, humid subtropical, which accounts for the entire Southeastern US.

Chapter 2. Background

Due to the adverse effects of UHI (Oke 1997), there are considerable interests in developing cost-effective measures in mitigating this phenomenon. One such suggestion has been to implement cool roofs, or roofs which have high solar reflectance values (albedo) and/or thermal emittance properties, so that thermal temperatures decrease (Akbari 2008). Cool roofs are able to achieve this by either being painted white, another solar reflective color, or built with engineered materials that can give off heat very quickly (high emissivity). Although green roofs, roofs with vegetative cover, have been shown to also effectively mitigate temperature effects related to UHI (Susca *et al.* 2011), they are not considered the same as cool roofs due to the differences between the cost of the initial installation and maintenance. Georgescu *et al.* (2014) studied the urban landform and consequences to the regional climate and concluded from global climate models that cool roofs would counteract the UHI effect in terms of increased greenhouse gases (GHGs). However, it was also shown in this same research that the benefits of white roofs vary drastically depending on the geographic region. This is due from the increased heating that will occur for winter months, which are more common in northern cities, in the US. By factoring in differences, such as passive cooling, this counterbalance effect will be mitigated. Research from the Lawrence Berkeley National Laboratory discovered a series of different tests that white roofs are the most economically viable option, as it was shown to reduce energy demanded as well as reducing the greenhouse impact caused from urban cities (Rosenfeld *et al.* 1998).

There is some disagreement, however, with the beneficial potential of cool roofs, which is the rooftops ability to reflect energy thus decreasing the thermal load of a building. In 2011, it was shown through an engineered model that the total climate response to white roofs and other urban surfaces may, in fact, contribute to more global warming (Jacobson *et al.* 2012). The model showed that although there is local cooling, a lower atmospheric UHI would create fewer cloud formations and that the reflected solar energy could potentially become scattered, by common urban pollutants such as aerosols, as it travels back up to the atmosphere.

In response, the Heat Island Group, researchers from the Lawrence Berkeley Lab, used a detailed global land surface model from NASA Goddard Space Flight Center to research the validating of the critiques proposed against cool roofs. Contained within this model was regional information on surface variables, such as topography, evaporation, radiation, and temperature, as well as on cloud cover. For the northern hemisphere during the summer, it was concluded that increasing the reflectivity of roof and pavement materials in cities with a population greater than 1 million would achieve a one-time offset of 57 gigatons of CO_2 emissions. For comparison, the worldwide CO_2 emissions in 2006 were 28 gigatons (Akbari *et al.* 2009).

2.1 Urban Heat Island Intensity

Urbanization has led to the rapid development of natural landscapes into concrete structures and asphalt roads within the past century (Arnfield 2003). Many of these urban and suburban areas also experience elevated temperatures compared to their surrounding rural areas; this temperature difference is what creates an Urban Heat Island Intensity (Wong *et al.* 2011). It has been shown by measurements taken from space that temperature differences for urban climates can reach as high as 22°F (12°C) (Oke 2002). Since temperature is a comparative measurement, it is important to distinguish the difference between surface and atmospheric Urban Heat Island Intensities (UHII).

2.2 Surface UHII

During a typical summer day, urban surfaces, such as roofs, can have temperature differences much higher than the surrounding air temperatures (Pomerantz *et al.* 2000). A major difference that exists between surface UHIIs and atmospheric UHIIs is that surface UHIIs are usually present both during the day and night times, with the strongest difference in temperature tending to be present during the daytime when the sun is brightest. It has been shown that daytime surface temperatures varied as much as 18 to 27°F (10 to 15°C), and nighttime surface temperatures varied between 9 to 18°F (5 to 10°C) (Voogt *et al.* 2003). Urban Heat Island Intensities are strongest when there is no clouds present and the wind is at its calmest. Clouds can interfere by blocking the incoming solar radiation, and strong winds can increase the atmospheric mixing of the differing temperatures (Morris *et al.* 2001). Surface UHII is typically measured indirectly by the use of remote sensing, where estimates of the land surface temperature are either collected or reproduced (Voogt *et al.* 2003). From the remotely sensed data, thermal images can be created to show these temperature differences.

2.3 Atmospheric UHII

Air temperature is usually warmer in urban areas compared to the air in the surrounding rural areas, and this difference creates the atmospheric UHII. When studying atmosphere it is important to define where in relation to elevation the temperature is being studied, and in most cases, meteorology stations take air temperature measurements at 1.5-2 meters (5-6.5 feet) above the surface (Ahrens 2007). Whereas the surface has one layer, the atmosphere consists of multiple layers and as the area being studied continues in elevation, the temperature differences from surface UHII will be much greater (Oke 1982). Atmospheric UHII is often weak during the late morning and day but becomes strongest after the sun has set, this is opposed to what occurs for surface UHII where the temperature difference occurs from the conductive properties of the storage of heat that occurs throughout the day, known as ground heat flux, which is slowly released at night (Oke 1973). There exist much fewer interferences for the atmosphere than what exists for the surface, therefore this enables air temperatures to quickly become mixed within the atmosphere, and therefore will show less variance in temperature (Oke 1973). On average, a typical large city can show an atmospheric UHII range of 1.8 to 5.4°F (1 to 3°C) warmer than the surrounding rural area (Oke 1997). Measurements for air temperature are usually taken directly from fixed weather station data, and because there exists a relationship between surface and atmospheric UHII the two can be comparatively studied, albeit with consideration for statistical differences (Lui and Zhang 2011), such as using root mean square error (RMSE) tests.

2.4 Solar Reflectance (Albedo)

When studying UHII, a direct consequence of the strength of a UHII depends on the difference between how much energy from the sun is arriving onto the Earth and how much is being reflected back into space. Albedo is measured as the percentage of solar energy that is reflected by a surface, in relation to total solar energy (Budikova *et al.* 2010). Solar energy is composed of ultraviolet (UV) rays, visible light, and infrared energy, which all arrive on Earth’s surface in differing percentages. Most of the solar energy that produces heat is found within the infrared spectrum (700nm-1mm). In addition to infrared energy, nearly as much energy that reaches the Earth is within the spectrum of visible light (400-700nm) (Arnfield 2003) (See figure below). Due to this phenomenon, lighter colored surfaces tend to have much higher solar reflectance than do darker colored surfaces. Urban areas tend to have surface materials that have lower albedo values than surrounding rural areas, reflecting less solar energy, thus absorbing more solar energy, which contributes to greater surface temperatures (Taha *et al.* 1988).

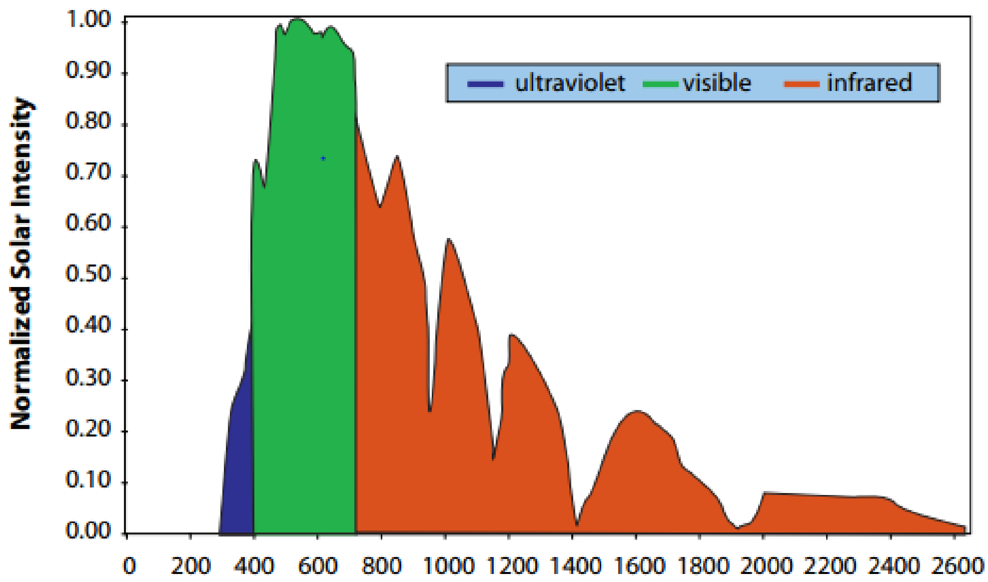

Figure 3: Note that solar energy intensity varies over wavelengths from about 250 to 2500 nanometers.

2.5 Solar Irradiance

Albedo is one such variable that can be directly controlled by engineered methods, however, the incoming solar energy produced from the sun is a constant 1367 W/m^2 (Bard *et al.* 2000). This output changes seasonally depending on the solar position, such as Earth's angle to the position of the Sun's incoming radiation. During the winter in the Northern Hemisphere, the Sun's Azimuth, or angle of position is at 23.5° with Earth's axis tilted away from the Sun, meaning that less direct solar radiation reaches the surface, but is diffused across the area of the surface instead (Pinker and Laszlo 1992) (See appendix 3 & 4).

However as this incoming solar radiation travels through Earth's atmosphere and eventually touches the surface, much of the energy becomes absorbed, scattered, and reflected. During cloud-free days incoming solar energy comes in by direct solar irradiance, meaning that almost no scattering occurs. Thus, during cloudy days, diffused solar radiation reaches the Earth in scattered forms of energy (Madronich *et al.* 1999)(See figure below). Some interferences of incoming solar irradiance can occur from the surface elevation itself, which causes a shadowing effect to occur (Hofierka *et al.* 2002).

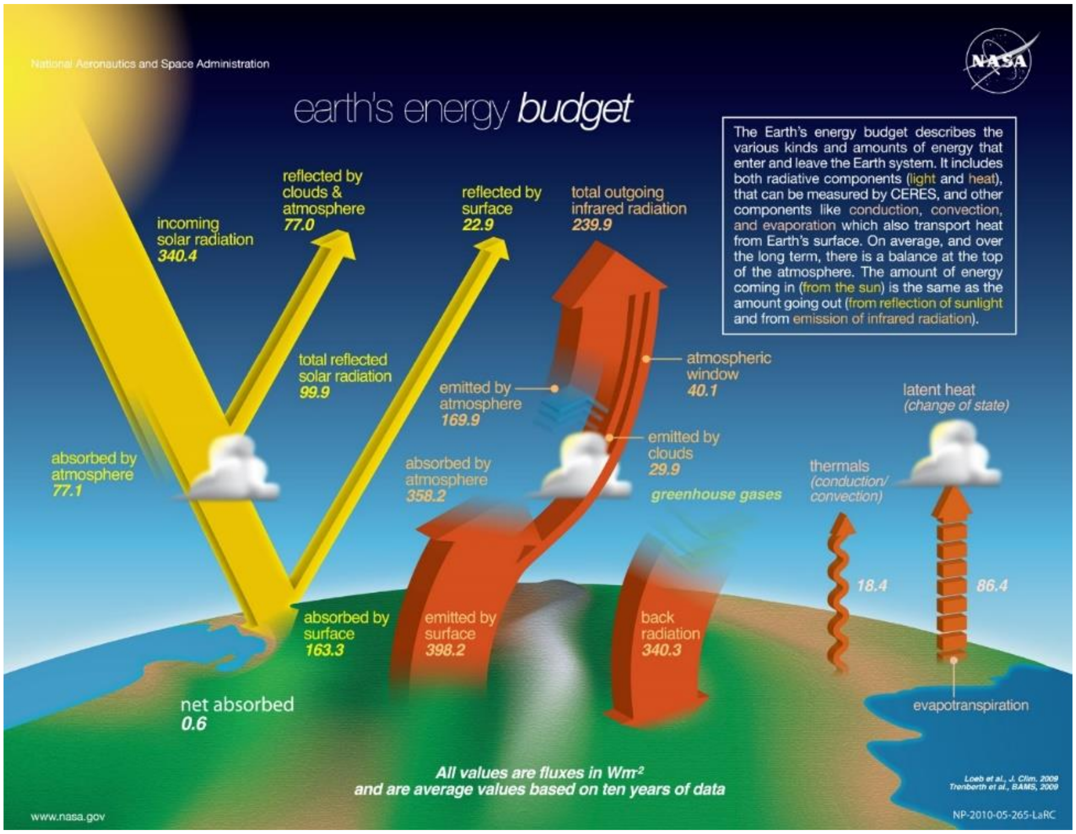

The Earth's energy budget describes the various kinds and amounts of energy that enter and leave the Earth system. It includes both radiative components (light and heat), that can be measured by CERES, and other components like conduction, convection, and evaporation which also transport heat from Earth's surface. On average, and over the long term, there is a balance at the top of the atmosphere. The amount of energy coming in (from the sun) is the same as the amount going out (from reflection of sunlight and from emission of infrared radiation).

Figure 4: From 100% incoming solar radiation, 30% is lost in space due to scattering and reflectance, another 19% is absorbed in the atmosphere, due to absorption by water vapor, aerosols, clouds and particles, and 51% is absorbed in the surface as direct and indirect radiation (irradiance) (Nasa 2010) https://science-edu.larc.nasa.gov/energy_budget/.

2.6 Anthropogenic Effects from Energy Use

Although UHII is largely determined from the percentage of energy that arrives from the Sun, there is also a significant amount that can be produced by human activity. These activities can include the running of air conditioners, used for cooling interiors, among other processes. Heat is generated from these processes which lead to the anthropogenic effects of raising land surface temperatures much higher than they would otherwise occur naturally (Kimura *et al.* 1991). This is especially worrisome as it could lead to a positive feedback effect to occur, where the increased added heat from the use of air conditioning leads to an increased need for the use of additional cooling. Furthermore, it is estimated that due to the UHI effect, demand for electricity has increased 5 to 10 percent (Sailor *et al.* 2003) (See figure below).

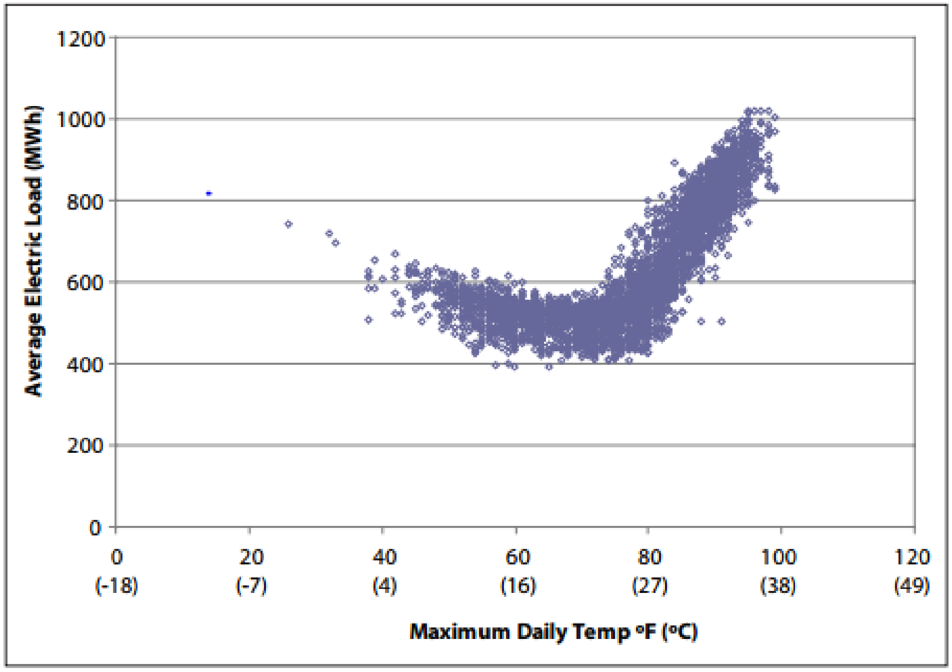

Figure 5: As shown in this example from New Orleans, electrical load can increase steadily once temperatures begin to exceed about 68 to 77 degrees F (20 to 20 degrees C). Other areas of the country show similar demand curves as temperature increases (Sailor *et al.* 2003).

2.7 Mitigation Strategies to Reduce UHII

There are several ways in which city planners, businesses, communities, governments, and individuals can adapt against the adverse effects of UHII. An obvious solution is to replace materials that absorb a lot of solar energy, such as concrete and asphalt, with vegetation. This can even be accomplished by the placement of green roofs, which are traditional roofs that have been replaced with vegetation (Takebayashi *et al.* 2007). Other mitigation strategies include making surfaces more reflective by either applying a light colored paint or by replacing surfaces with high emissivity materials (Rosenfeld *et al.* 1998). Some procedures are still in development and costs for different alternatives vary widely. The best strategies should consider the region, scope, scale, and place of the surface (Levinson *et al.* 2005).

2.8 Cool Roofs

One of the most cost-effective methods for mitigating the effects of UHII is through the process of having cool roofing on a building (Rosenfeld *et al.* 1998). Cool roofs are made up of materials that are usually highly reflective and/or highly emissive, meaning gives off heat quickly. Cool roofs are especially important in mitigation strategies because, in the US, a typical roof during peak summer temperatures can reach upwards to 150 to 185°F (66-85°C) (Konopacki 2010). Having cool roofs, such as whiter roofs, the solar reflectance will be much higher than the values for traditional roofs (65 percent compared to 5-15 percent), meaning that they will absorb much less energy, thus reflecting most of that energy back towards the atmosphere (Scherba *et al.* 2011).

Since cool roofs mitigate the effects of UHII, many benefits that accompany such mitigation might include reduced demand for energy use, lowered amounts of air pollution and

GHGs, and improved human health and comfort. The most beneficial would be the reduced demand for energy used for cooling. Because less solar energy actually reaches the roof, the transfer of this energy to the rest of the building is significantly lessened, with the average amount of energy saved from the installation of a cool roof amounting to 20 percent (Haberl and Cho 2004). This reduced energy demand also has the added benefit of reduced air pollution and GHG emissions, due to the fact that much of the energy comes from the burning of fossil fuels. The production of this energy causes many pollutants to be put into the air, and can very negatively impact human health (Haines *et al.* 2006).

Although the benefits are numerous, there are limitations to having a cool roof. The largest adverse effect of a cool roof is the wintertime heating penalty. This occurs in colder climates where the heating degree days (HDD), that is the days that energy is needed for heating, far outnumber the cooling degree days (CDD). Within the Southeastern regions of the US, this penalty is almost non-existent (Synnefa *et al*. 2007). Additionally, during the summertime versus the wintertime, the Sun is at a different angle which causes days to last at differing lengths (Pinker and Laszlo 1992) (See Appendix 3 & 4). With the days being shorter during winter, taken as less incoming solar irradiance, the effects of cool roofs are less impactful than it would be during the summer. Wintertime also tends to have more cloudy days (Castanho *et al.* 2001) and in northern climates where white snow may potentially cover areas, both will act to reflect the Sun's energy from otherwise reaching the roof.

Chapter 3. Methodology

All of the satellite images were processed from raw data in order to obtain valid LST, albedo, and solar irradiance data. As a first step, several raster analysis were performed through open source software such as QGIS, Geographic Resource Analysis Support System (GRASS), and System for Automated Geoscientific Analysis (SAGA). In order to accurately measure LST, the raw data that is stored from the satellite must be downloaded (https://earthexplorer.usgs.gov/) and converted into quantifiable data (Roy *et al.* 2014). This process can be converted into any number of physical parameters such as radiance or reflectance taken from the multi-spectral image that is received at the sensor (Landsat 2011). If it is taken as the top of the atmosphere, this means that no atmospheric effects have been accounted, such as scattering and absorption. However, if the image is captured at the top of the canopy, an appropriate method of atmospheric correction has been applied (Fleming 2003).

Once the image is taken as radiance or reflectance, then this image is able to be used in a geographic analysis. In order to calculate LST, there are several methods which can be used. The method chosen in this study was the inverse-plank function, due to the widespread use and strong support of documentation that could be followed within the scientific literature (Isaya *et al.* 2016). However, by calculating LST using this method, two values are needed. These values must include brightness temperature, the theoretical temperature achieved if the surface is assumed to be a blackbody (a perfect emitter), and land surface emissivity (LSE), which is the thermal property of a surface describing how quickly that surface can give off heat (See appendix 5 & 6). Where the calculation of brightness temperature is much more uniform, the calculation of emissivity is much more diverse. Some approaches to estimating emissivity are through land-based classification of multi-spectral images, which are then given an associated emissivity value for the given classification (Snyder *et al.* 1998). For example, soil, vegetation, urban build-up, and water would all have an associated emissivity value that would be different from one another.

Other methods to calculate emissivity include direct measurements by using tools such as pyrometers and infrared cameras (Crawford *et al.* 1999). Often the use of such methods makes the calculation of LSE too costly due to the employment of the technology, can introduce errors due to human judgment of land-based classification, or presents a limited feasibility for the study area when under consideration from time constraints. Therefore the method used for this study was to first calculate the normalized difference vegetation index (NDVI) and then apply an algorithm to each pixel depending on the given output value (Weier 2000). This method has been developed by climate scientists and experts in the field of remote sensing (Xiao *et al.* 2007).

Because LST only gives one picture of the entire energy system that occurs on earth (See Appendix 2), albedo is also calculated to show the percentage of energy that is being reflected. Albedo can be calculated using multi-spectral images, meaning images with several bands or spectral frequency readings. In addition, the final consideration of this study for the energy budget includes incoming solar irradiance (insolation), which has been modeled with consideration given to the shadowing effect that occurs due to the elevation and topographic features of the land surface. All three of these variables, LST, albedo, and incoming solar irradiance, contribute to a complete picture of the dynamics of the energy system that are being transferred across the spatial-temporal dimension of Auburn University's campus. These procedures are captured in the following flowchart.

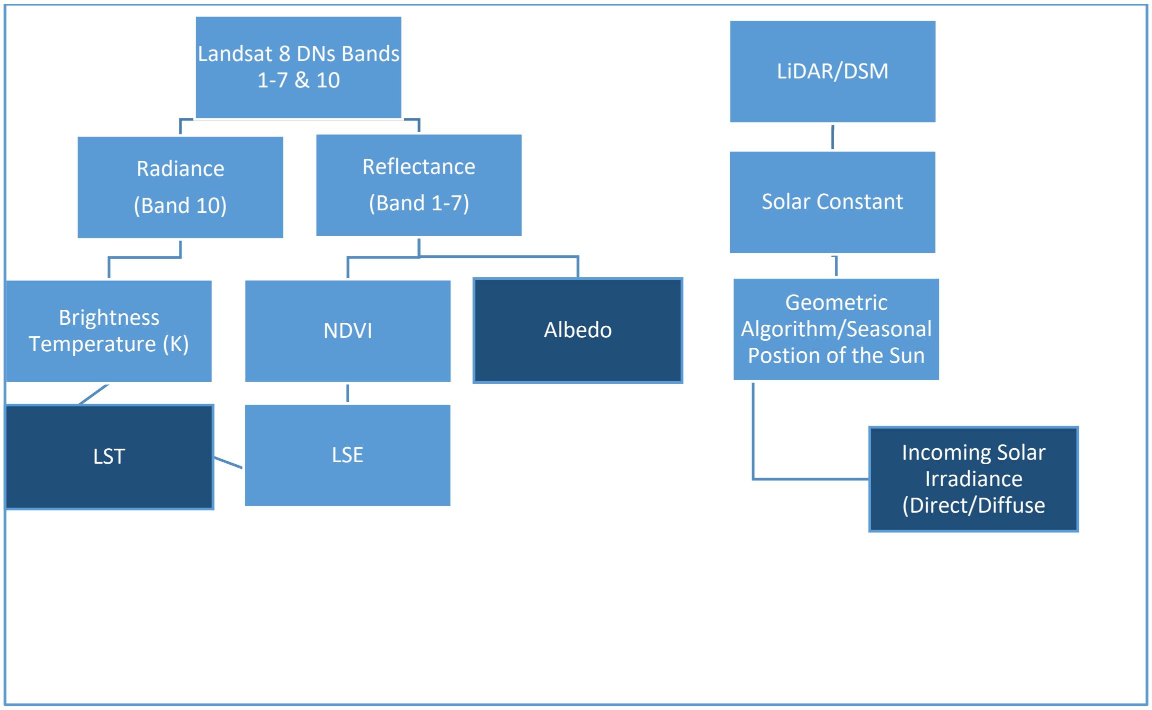

Figure 6: Landsat and elevation data is processed through several algorithms for the outputs of LST, albedo, and solar irradiance.

A predictive linear model has been built that takes the above variables including energy consumption data, which is monitored by Auburn University's facilities management, with an attempt to limit any distortion or bias that the three variables may give towards their relational effect on energy consumption. This has been accomplished by performing and ordinary-least square regression, which accounts for the standard residuals (instances where the predicted outcomes were over/underestimated) of the model, and a geographically weighted regression.

Table 2 will help cement how each variable was derived for use within the model. All of the initial processing was done through QGIS, however, SAGA GIS was also used for calculating Solar Insolation, and the created raster was exported into QGIS so that all of the variables could be worked with simultaneously, which resulted in a more manageable workflow. Within QGIS, the raster calculator function can be used with all of the associated formulas noted in this study, however, through the use of an already built-in PyQGIS plugin, much of the processing was automated for calculating LST.

Table 2: Software Requirements for Model Variables

Variable	Software Used	Notes
Radiance	QGIS – PyQGIS Plugin	DN is downloaded from USGS' website
Brightness Temperature	QGIS – PyQGIS Plugin	
NDVI	QGIS – PyQGIS Plugin	Reflectance is downloaded from USGS' website
LSE (Emissivity)	QGIS – PyQGIS Plugin	
LST (Temperature)	QGIS – PyQGIS Plugin	
Albedo	QGIS – Raster Calculator	Microsoft Excel used for RMSE analysis
Solar Irradiance	SAGA – Potential Incoming Solar Radiation	Output raster was imported into QGIS after being modeled in SAGA GIS.

As was previously shown, the process begins with two geographic source datasets (Landsat 8 OLI/TIRS & Auburn's Aerial LiDAR/DEM). Landsat collects spectral data from radiation such as light, whereas the Aerial LiDAR has modeled surface elevation characteristics. Since temperature is a form of radiation, it was necessary for radiance to be used. However, since LST is derived from the radiant temperature (brightness temperature), and the thermal properties of the surface (LSE) both are used to calculate the final LST. By using images calculated as reflectance the surface characteristics became more easily identified (http://www.harrisgeospatial.com/Home/NewsUpdates/TabId/170/ArtMID/735/ArticleID/13592/Digital-Number-Radiance-and-Reflectance.aspx). Therefore, the use of the reflectance value is preferred when calculating NDVI and Albedo, both which are surface characteristics (USGS 2017). In order to calculate the incoming solar radiation arriving on the surface, the geometric position of the Earth and Sun is modeled (Hofierka *et al.* 2002). Additionally, any shadowing effects that occur due to elevation is considered within the algorithm to give the output of solar irradiance. The separation of data processes allows the outputs to be checked independently from one another. The finalized outputs are LST, albedo, and solar irradiance, all of which has given the differing thermal-radiative quantities of physical characteristics of the Earth.

3.1 Conversion DN to Radiance

The thermal data in the Landsat satellite imagery is stored as Digital Numbers (DNs). In order to have accurately estimated LST, the DNs first needed to become converted into radiance values. This process was done through QGIS python plugin – Land Surface Temperature Estimation Using Landsat (See figure 7).

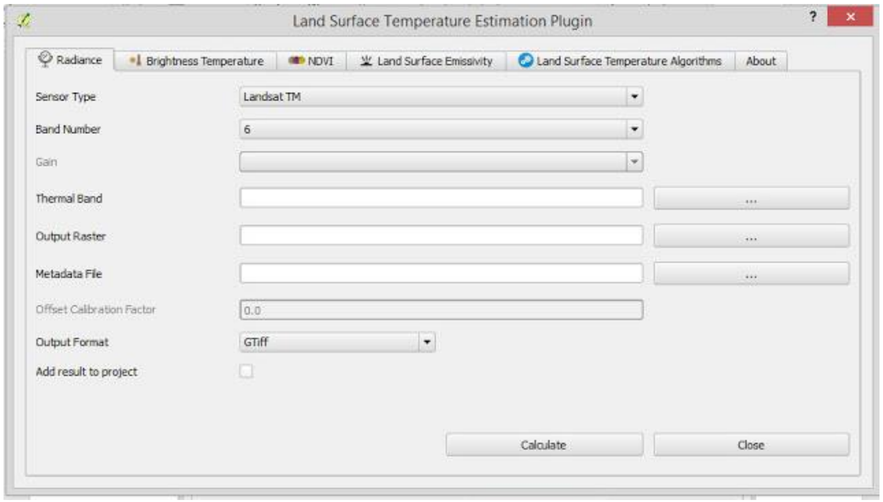

Sensor Type: Landsat TM
Band Number: 6
Offset Calibration Factor: 0.0
Output Format: GTiff

Figure 7: A PyQGIS plugin for Land Surface Temperature Estimation Using Landsat Images

The use for the offset calibration of the image, O_i, was given as the value of -0.29. This calibration offset is valid only for Landsat 8 TIRS band 10, and not TIRS band 11, due to uncertainty in the band's value. (Isaya *et al.* 2016). The use of such a method required the following formula:

$$L_\lambda = M_L Q_{cal} + A_L - O_i$$

Where:

L_λ is Top-of-Atmosphere (TOA) spectral radiance
M_L is the band specific multiplicative rescaling factor from the metadata file
QCAL is the digital number, such as the quantized and calibrated standard product pixel values
A_L is the band specific additive rescaling factor from the metadata file
O_i is the offsets issued by USGS for the calibration of the TIRS bands

Through the use of the PyQGIS plugin, the final output raster for Radiance is shown in the figure below. This image is what a satellite would see from TOA. It is the amount of energy that is being captured from the aperture of the satellite's sensor. By calculating radiance values, other thermal characteristics can become derived, such as brightness temperature.

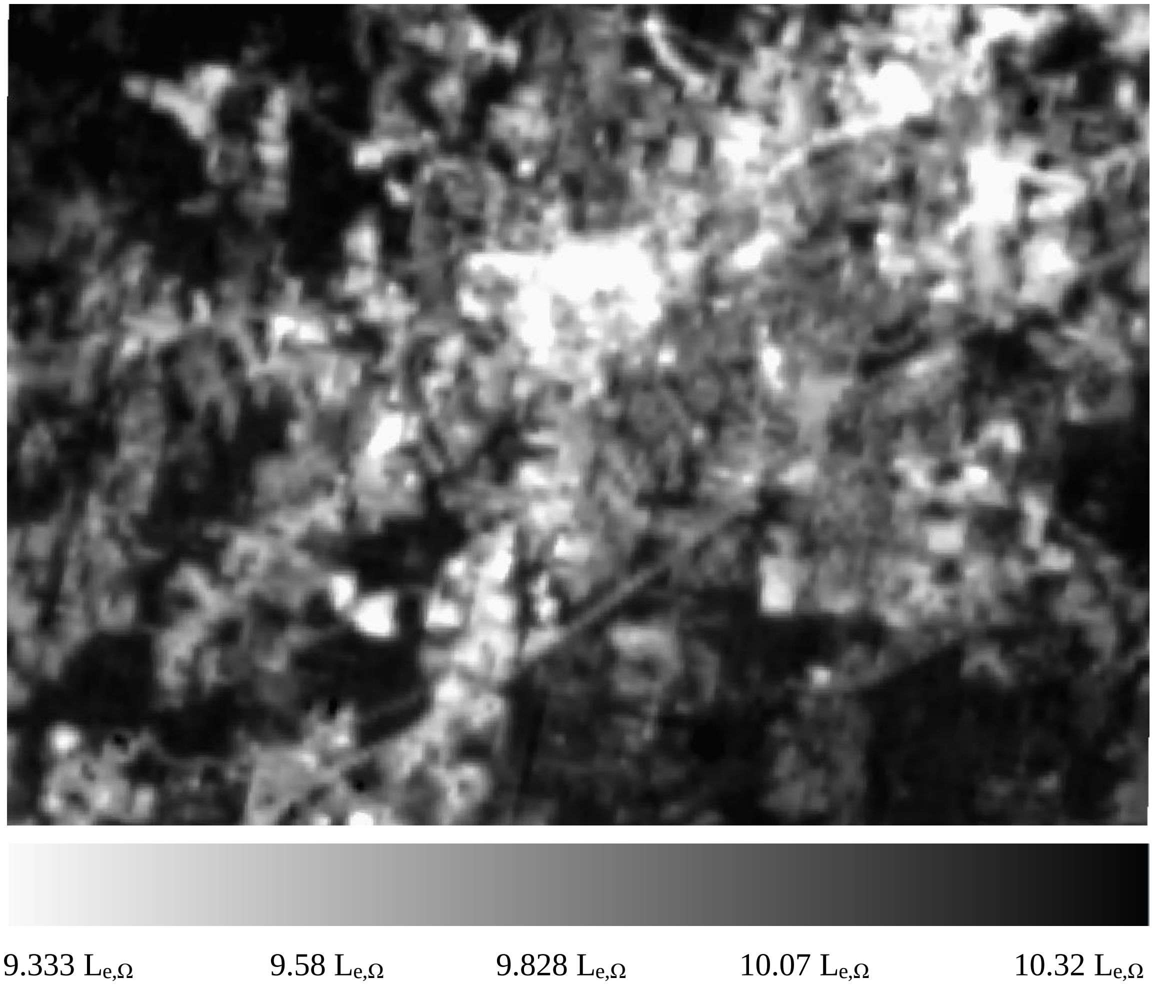

Figure 8: This image gives an example of what type of reflectance or brightness energy appears to the remote sensor of the satellite.

3.2 Conversion of Radiance to Brightness Temperature (K)

Brightness temperature is the temperature that a blackbody needs in order for it to emit the same amount of radiation of surface area to its surroundings. It is important to note that although brightness temperature can represent temperature measurements, it still lacks important characteristics from being actual physical temperature. After the radiance values have been determined the processed image, which is the raster output, can be converted to brightness temperature by using Planck's Radiance Function. This is again accomplished by the use of the PyQGIS plugin which was used previously. The below formula is included in the plugin:

$$B_{\lambda}(T) = \frac{C_1}{\lambda^5(e^{\frac{C_2}{\lambda T}} - 1)}$$

Where:

B_{λ} *(T)* is spectral radiance of the blackbody in W/ (m^2 sr µm)
λ is a wavelength in meters
C1 is a constant (=1.19104356 × 10−16W m2)
C2 is a constant (= 1.43876869 × 10−2m K)
T is the temperature in Kelvin

Within the context of remotely sensed images, the following formula can be used by obtaining the thermal constants that are included in the Landsat metadata file.

$$T = \frac{K2}{\ln(\frac{K1}{L_{\lambda}} + 1)}$$

Where:

T is the effective at-sensor brightness temperature (K)
K2 is the calibration constant 2 (K)
K1 is the calibration constant 1 [W/(m^2 sr µm)]
L_{λ} is the spectral radiance at the sensor's aperture [W/m^2 sr µm)]
Ln is the natural logarithm

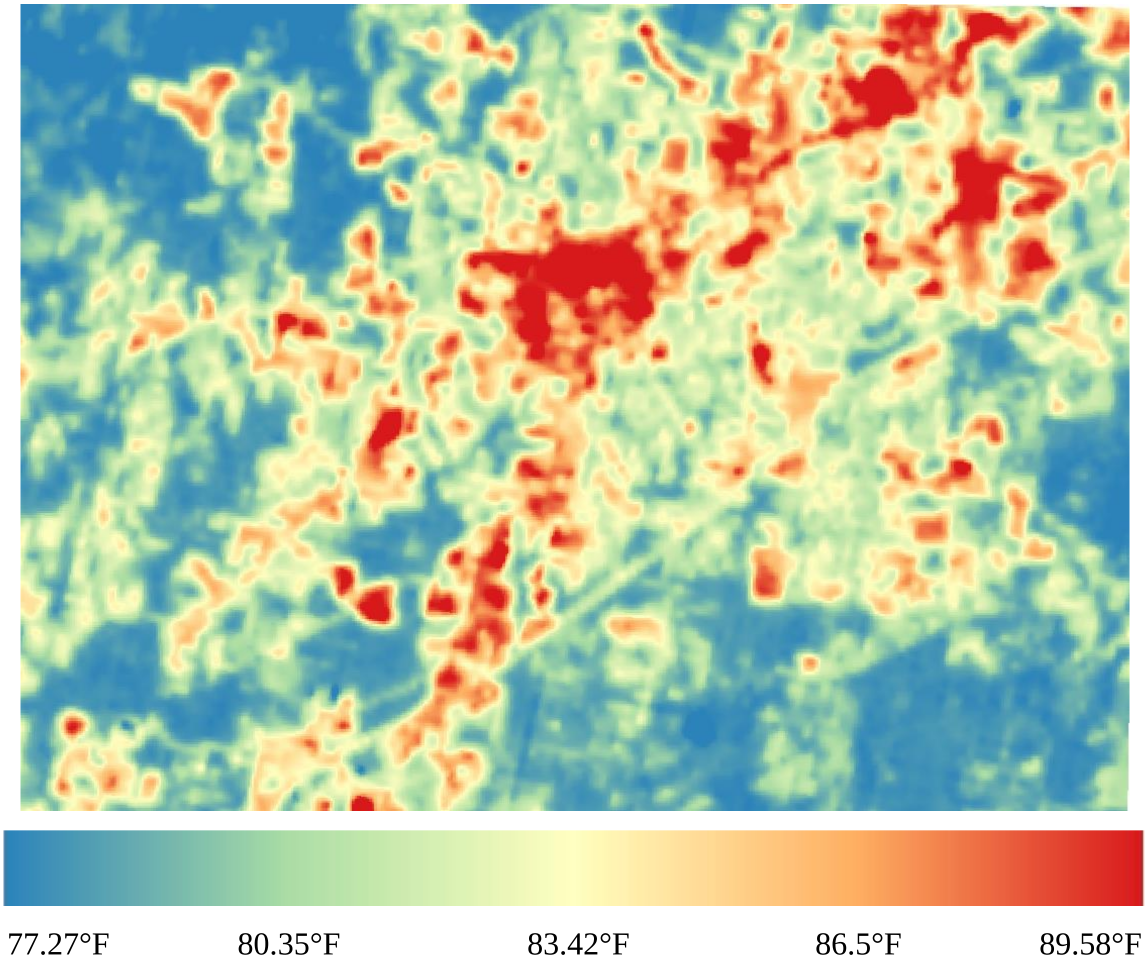

Figure 9: This image shows the theoretical temperature if all of the surfaces was a perfect emitter. This can give insight as to what temperature differences exist for one main characteristic of cool roofs. Note for comparison, the brightness temperature is converted into Fahrenheit degrees, it is usually the case for brightness temperature to be left in Kelvin.

An important characteristic of Brightness temperature is that it is almost exclusively given in Degrees Kelvin (K). This is due to the fact of objective conformity within the scientific community. However, sometimes, it may be common to transform the original Kelvin values to other temperature values, for ease of comparison. In order to convert Kelvin to Celsius, it is necessary to add the value of 273.15 to what is given as the Kelvin value. Thus making absolute zero (0 degrees K), -273.15 degrees Celsius. In order to derive the Fahrenheit values, a ratio of 9/5 is taken against the Celsius value, if only given the Kelvin value then it can become easily converted by the addition of the 273.15 value to it, with the addition of the positive integer 32. Thus represented as:

$$Degrees\ F = \frac{9}{5}(Degrees\ C) + 32$$

$$Degrees\ F = \frac{9}{5}(K - 273.15) + 32$$

3.3 Calculation of the Normalized Difference Vegetation Index (NDVI)

One of the earliest calculations developed for remotely sensed images was that of the normalized difference vegetation index (Weier 2000). This index is able to determine the amount of vegetation that inhabits an area of land. The calculation of NDVI uses bands 4 (Red – 0.636-0.673) and bands 5 (Near Infrared (NIR) 0.851-0.879) for Landsat OLI. NDVI can be defined mathematically as:

$$NDVI = \frac{(NIR - RED)}{(NIR + RED)}$$

Where:

NIR is the spectral reflectance in the near-infrared region
RED is the spectral reflectance in the red region

The QGIS plugin already has built-in functionality to obtain this calculation. The processed image of NDVI gives a vegetation index for an entire study area. It can accurately determine vegetative cover as well as the health of the vegetation being studied. The red areas that are shown in the figure below indicates urban built-up. There also exist other methods to classifying urban areas, such as creating training sites from supervised classification techniques, however, such methods do require much more resources, where the accuracy is directly relational to the number of training sites and spectral frequencies analyzed, which can create much variance in the accuracy of the image classification (Foody 2002). Additionally, this approach to the image classification was necessary due to its future use for algorithmically calculating land surface emissivity.

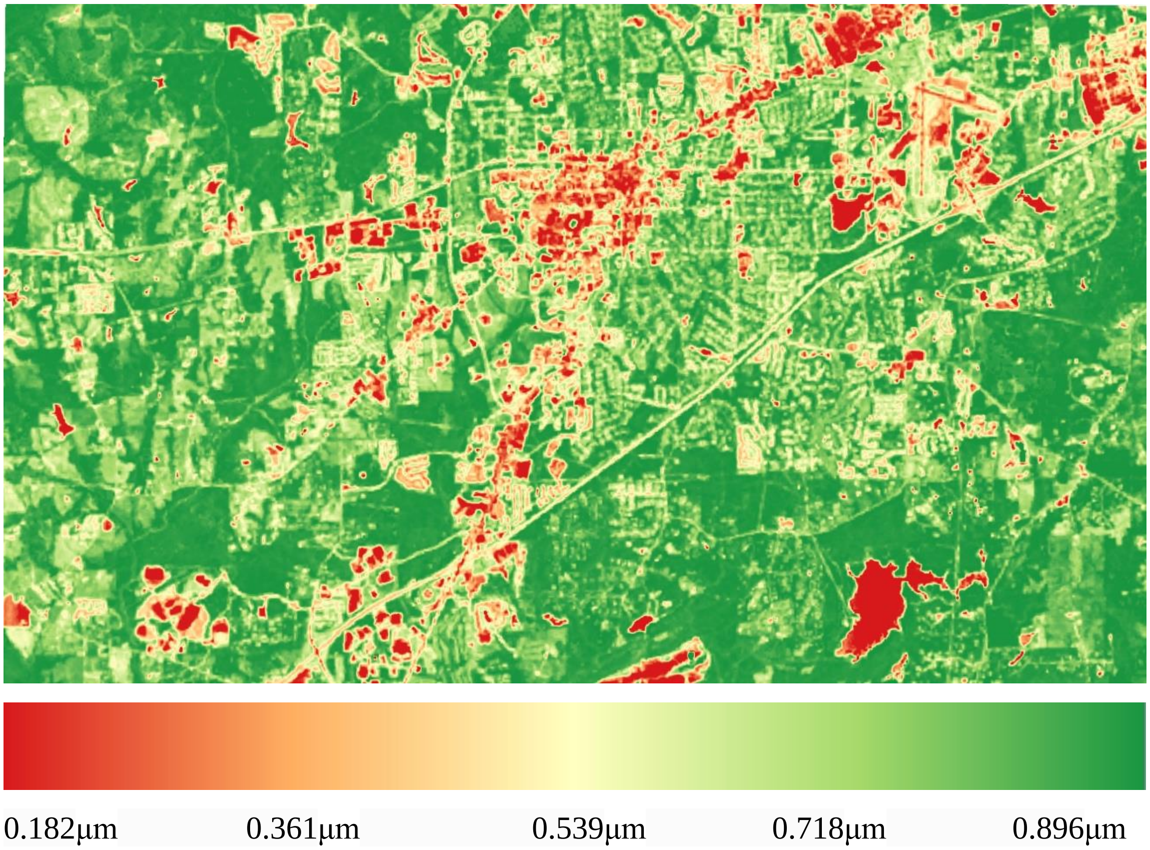

Figure 10: NDVI gives details as to where vegetation exists in an image. Green indicates the most thriving instances of vegetation, whereas red would indicate in situ of urban build-up.

3.4 Estimating Land Surface Emissivity (LSE)

Although the brightness temperature can give a general estimate of temperature, it should not be used as a replacement for LST. In order to derive LST, the material properties of the Earth need to be considered for their emissivity values. The most accurate approach to calculating LSE is to visually check the ground and perform the direct calculation of the area of study, but often this is too costly or too impractical, especially for larger study areas. The estimation of LSE within this project uses the NDVI based approach. This approach was introduced by Sobrino et al (2004). In Sobrino *et al.* (2004), the following formula for emissivity was calculated as:

$$\varepsilon = \varepsilon_v P_v + \varepsilon_S (1 - P_v) + d\varepsilon$$

Where:

ε_v is the vegetation of the emissivity

ε_s is the soil emissivity

P_v is the vegetation proportion obtained from the formula proposed by Carlson & Ripley, 1997.

$$P_v = (\frac{NDVI - NDVI_{\min}}{NDVI_{max} - NDVI_{min}})^2$$

Where:

$NDVI_{max}$ is 0.5

$NDVI_{min}$ is 0.2

This method was later adopted by Xiao *et al.* (2007) where an algorithm was further developed for calculating LSE. The authors presented that when the NDVI value of a certain pixel falls within a certain range, then emissivity can be applied to this pixel to determine the classification of the area being studied. In order to estimate LST, emissivity must be estimated. According to Xiao *et al*. if the normalized vegetation index (NDVI) is known, then it will be possible to estimate the emissivity of the pixel depending on the value of the cell this pixel falls under in relation to its NDVI value. Most of all the surface of Earth has an emissivity above 0.9

and is usually within 0.96 to 0.98 (Brewster 1992). If the NDVI value of a pixel value falls below -0.185, then an emissivity value of 0.995 will be assigned. If the NDVI value for the pixel falls between -0.185 and 0.157, then it will be assigned an emissivity value of 9.70. A logarithmic emissivity value is assigned for the NDVI pixel values between 0.157 and 0.727. Finally, if the pixel value for NDVI is above 0.727 then the assigned emissivity value is 0.990, as noted in the table below.

Table 3: Estimation Algorithm of Emissivity using NDVI

NDVI	Land surface emissivity (εi)
$NDVI < -0.185$	0.995
$-0.185 \leq NDVI < 0.157$	0.970
$0.157 \leq NDVI \leq 0.727$	$1.009\,4 + 0.047\ln(NDVI)$
$NDVI > 0.727$	0.990

The final processed image is shown below. Note that the emissivity values all fall within the expected range of 0.9 – 0.99, and also that the urban areas exhibit a much lower emissivity value than the surrounding rural area. This signifies that the urban areas will give off heat much more slowly than the vegetative rural area, which would contribute to a greater UHII occurring during the day and continuing through the night. Note that it is also possible to derive the temperature difference from emissivity between brightness temperature values and LST values (See figure 9 & 12). From such an analysis it is possible to obtain a theoretical limit of how much cooling can occur from replacing all surface characteristics as perfect emitters (Black

Bodies). When comparing such results, it is shown that the temperature minimums for both brightness temperature and LST are 77.27°F versus 78.3°F and the maximums are 89.58°F versus 94.63°F. This signifies that the theoretical maximum temperature that can be saved from the installation of a perfectly emissive surface would only be marginal, yet would undoubtedly be very costly.

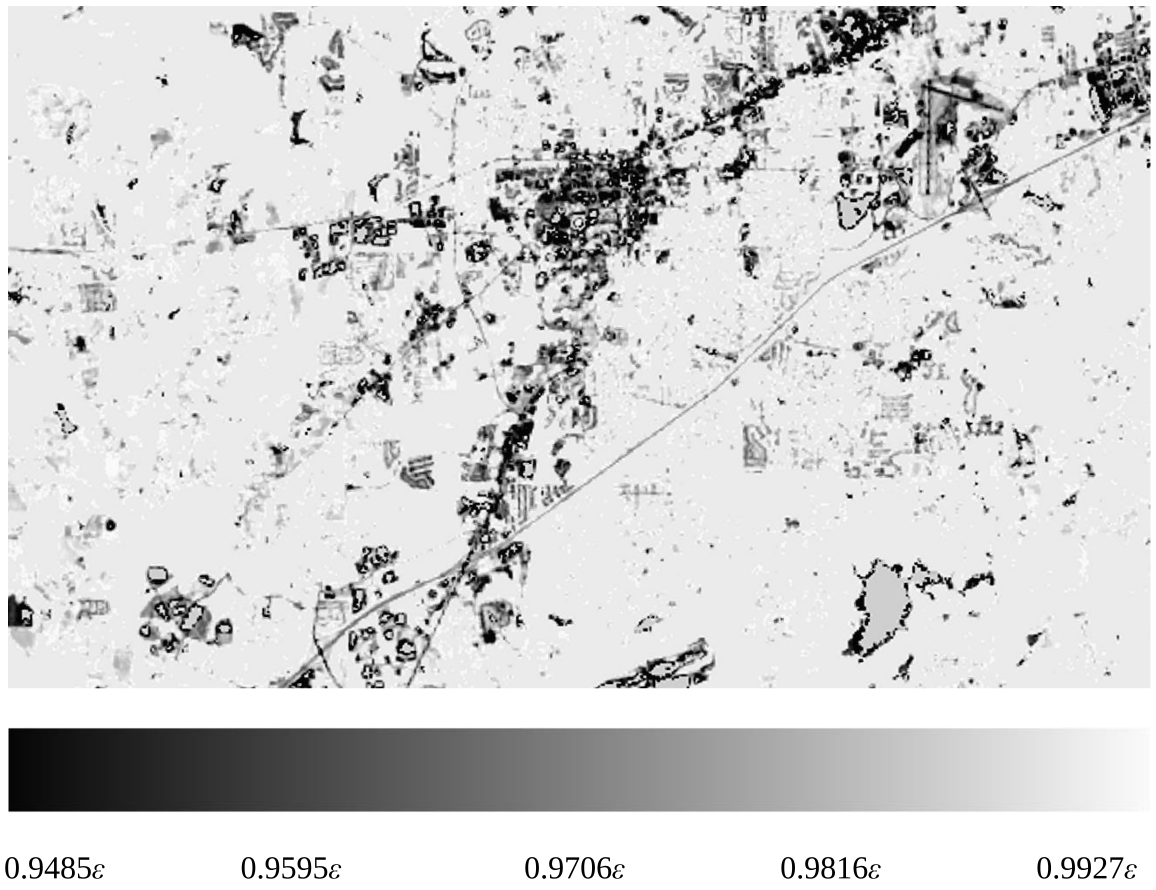

Figure 11: This image portrays the emissivity characteristics of the surface properties on Earth. A higher emissivity value means that the surface can give off heat at a faster rate than otherwise if it had a lower emissivity value.

3.5 Estimation of Land Surface Temperature (LST)

When computing LST through the PyQGIS plugin, the previously processed brightness temperature is corrected against LSE in addition to atmospheric effects. Within the PyQGIS plugin, there exist several valid methods to calculating LST, including using the mono-window algorithm, radiative transfer equation, the single-channel algorithm (Landsat/ASTER), and the split window algorithm (ASTER) (Isaya *et al.* 2016). Within this study, the inverse Planck function was used due to its simplicity and strong establishment among scientists. The formula for using Plank's equations is as follows:

$$T_S = \frac{BT}{\{1 + \left[\frac{\lambda * BT}{\rho}\right] * ln\varepsilon\}}$$

Where:

T_S is the land surface temperature (K)
BT is the at-sensor brightness temperature (K)
λ is the wavelength of the emitted radiance
ρ is the (h* c/σ), which equals $1.438 * 10^{-2}$ mK
ε is the spectral emissivity

After the following algorithmic formula is applied to each pixel value in all the combined images, a final LST image is processed (See figure below). This processed LST image shows the prominent UHI effect from the temperature difference between the urban versus the rural area, a surface temperature difference of 16.33°F (94.63-78.3). The hottest areas are related to the urban areas, while the lowest temperature areas are associated with outermost rural areas, which is what is expected from prior UHII studies. It is also shown by comparing the LST image against the image that shows brightness temperature, that the LST image is shown to have higher temperatures, which is also expected due to the factoring of the lower emissivity leading to warming. It is also important to note that the weather station data is corroborated with the processed LST image values, where it was shown that for the date of July 28th, 2015, there was a temperature high of 97 degrees F, and a temperature low of 75 degrees F. The processed image, in comparison, shows a temperature high of 94.63 degrees F, and a temperature low of 78.3 degrees F, which shows that the temperature is within an acceptable range, considering time and temperature acquisition differences. The temperature difference that does exist between LST and the weather station data would be caused by the variation of time when the data was recorded, the remotely sensed image of LST is taken at one point in time, the evening, and the weather station data has recorded the highest temperature point of the day. An additional factor to consider is the surface to the air temperature differences, where the weather station records temperature in a Stevenson screen at 1.25-2.0 meters above the ground (Bewoor 2009). The significance of such results are expected as the time period of the image capture is during the evening, which would be near, but not exactly the highest temperature point of the day.

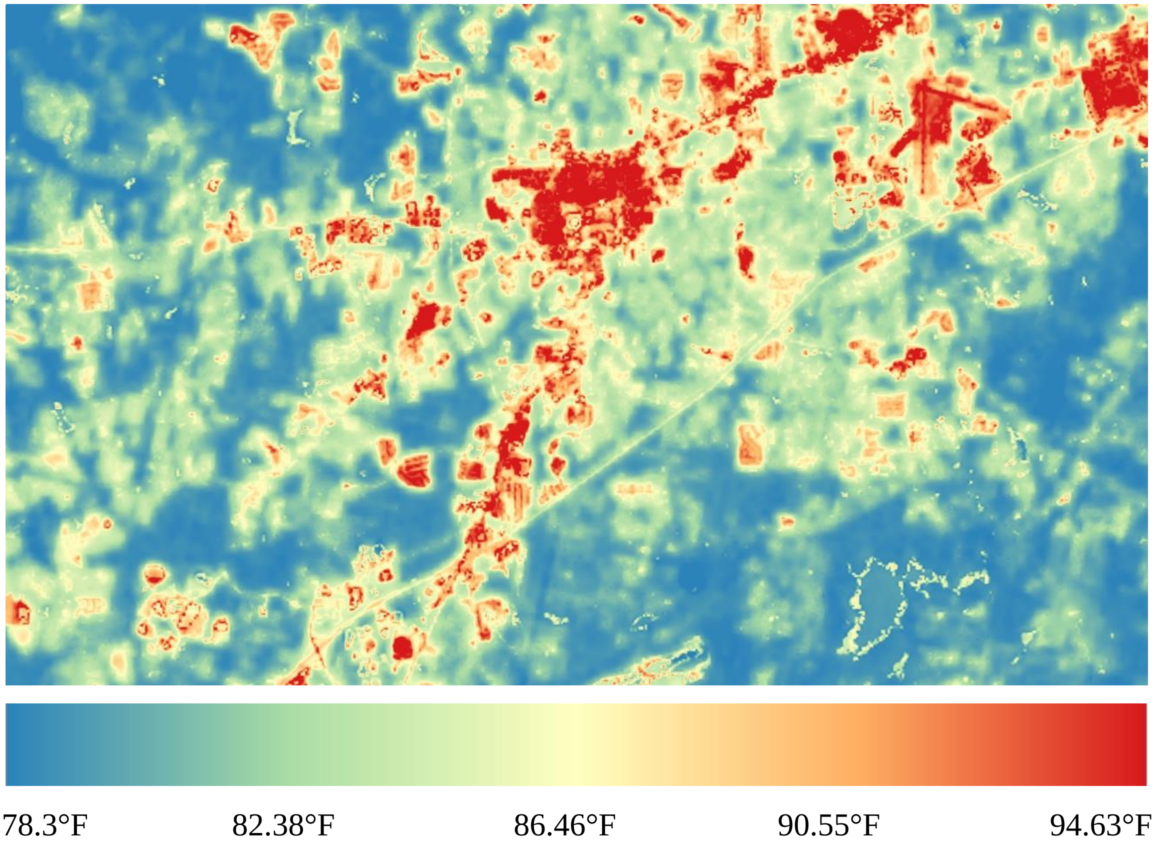

Figure 12: This image captures the temperature differences that exist within an Urban-Rural landscape.

3.6 Estimating Albedo

Albedo gives important information to be able to analyze Earth's surface energy budget (Trenberth *et al.* 2009). It is given as a ratio value between 0 and 1.0, which vary from land cover to land cover. To be able to calculate outgoing short-wave albedo with Landsat OLI/TIRS, the stored DNs must first be converted to either top of atmosphere (TOA) reflectance, which can be corrected with the atmospheric effects, or surface reflectance. Reflectance is the ratio of the power and radiant energy that is being reflected from a surface material. TOA reflectance can account for atmospheric effects, with the use of such methods as dark object subtraction (DOS) or other similarly developed algorithms. This study used the USGS Level-2 Landsat Surface

Reflectance product. TOA reflectance uses the below formula to convert images from DNs into radiance:

$$\rho_p = (\pi * L_\lambda * d^2)/(ESUN_\lambda * cos\theta_s)$$

Where:

L_λ is the spectral radiance at the sensor's aperture (at-satellite radiance)
d is the Earth-Sun distance in astronomical units (provided with Landsat metadata file
$ESUN_\lambda$ is the mean solar exo-atmospheric irradiances
θ_s is the solar zenith angle in degrees, which is equal to $\theta_s = 90^\circ \theta_e$ where θ_e is the Sun elevation

Since the deployment of Landsat 8 OLI, the development for an algorithm to calculate albedo has not yet been accepted within the scientific community. Due to currently not having a scientific consensus on what method of calculation works best for obtaining albedo values for Landsat 8, this study chose to employ four well known algorithms for calculating albedo within QGIS raster calculator and run a root-mean-square error (RMSE) analysis in Microsoft Excel in order to compare and validate which of the methods showed the least error and thus gave the most accurate results. Albedo values obtained and corrected from MODIS product MCD43A series was used as the initial infrastructure to test the following output variables against one another.

MODIS MC43A1 Version 6 Bidirectional reflectance distribution function and Albedo (BRDF/Albedo) Model Parameters data set is a 500 meter daily 16-day product, therefore observations are weighted to estimate Albedo for a given day. NASA employs the use of the MCD43A1 algorithm, which chooses the best representative pixel that includes all the acquisitions from both the Terra and Aqua sensors from the retrieval period. The function of the MCD43AI data is its ability to provide weighting parameters (coefficient variables) for three models, which include isotropic, volumetric, and geometric parameters. These weights are each associated with MODIS bands 1 through 7, as well as the spectral frequency wavelengths that are associated with the visible, near infrared, and shortwave bands. Together when the coefficient's weights are multiplied by the spectral wavelength of the associated bands, the product creates the image for an Albedo and BRDF, which are then derived to create separate MODIS products, such as MCD43A3 and MCD43A4. An additional parameter is layered specifically for each of bands 10 which are the Mandatory Quality layers. This layer acts to validate that the relational characteristics of the Earth are being accurately modeled, with the currently achieved validation being stage 3 (NASA 2015) for the above products.

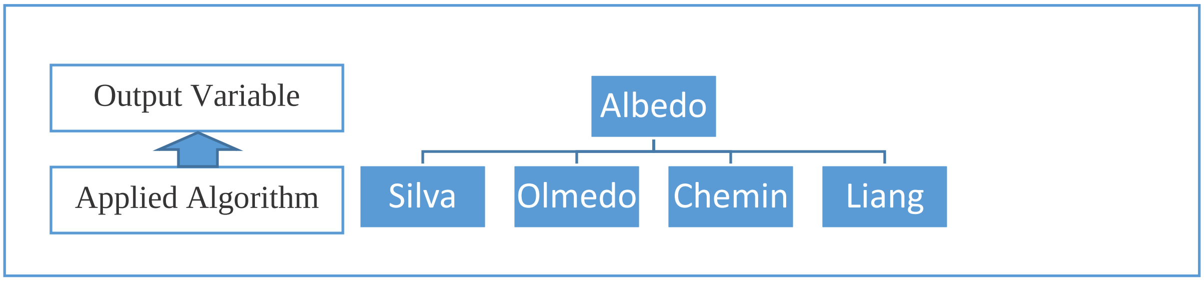

Figure 13: Differing methods used to calculate Albedo values for Landsat.

As can be seen in the above flowchart, in order to establish an albedo value to be used within the predictive model, several methods were tested and compared against each other. These methods are named from the principle scientists that developed the algorithms that are used. Two of the methods shown, Silva and Olmedo, have been proposed for use with the Landsat 8 multispectral bands. The other two methods, Chemin and Liang, have been established for use with the Landsat 5 & 7 multispectral bands. Therefore the objective established, was to analyze the compatibility of the scientifically accepted weighted coefficients from the Landsat 7 algorithms against the unsubstantiated yet updated Landsat 8 algorithms.

3.6.1 The Silva Method

Although there exist numerous methods for calculating albedo for Landsat TM and ETM+ (5 & 7 respectively), there does not currently exist an established method for calculating albedo for Landsat OLI/TIRS (8) (Silva et al. 2013). Researchers from Brazil attempted to establish such a procedure that could be used with the latest Landsat OLI/TIRS. In their study, they used the river basin in the semiarid region of Northeastern Brazil and compared several methods used for calculating albedo. One of the main challenges in calculating albedo with the new bands established for Landsat 8 is determining how much weight should be applied to each band using multiplicative properties (See table below). The below formula was recommended as a suitable method that could be used to calculate albedo from this study, which can be done through QGIS's raster calculator:

$$\alpha_{short} = 0.300\rho_2 + 0.277\rho_3 + 0.233\rho_4 + 0.143\rho_5 + 0.036\rho_6 + 0.012\rho_7$$

Where:

ρ represents Landsat OLI/TIRS bands 2,3,4,5,6, and 7.

Table 3: Multiplicative properties of Landsat 8 multispectral Bands

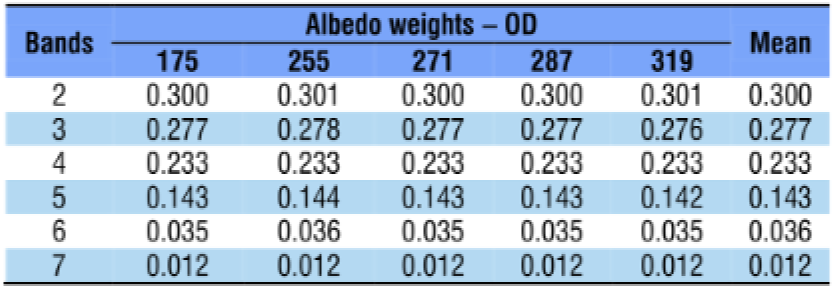

Bands	Albedo weights – OD					Mean
	175	255	271	287	319	
2	0.300	0.301	0.300	0.300	0.301	0.300
3	0.277	0.278	0.277	0.277	0.276	0.277
4	0.233	0.233	0.233	0.233	0.233	0.233
5	0.143	0.144	0.143	0.143	0.142	0.143
6	0.035	0.036	0.035	0.035	0.035	0.036
7	0.012	0.012	0.012	0.012	0.012	0.012

This table details the associated weights that were applied to each spectral band within the Landsat 8 OLI satellite.

3.6.2 The Olmedo Method

‘Water’ is an open source package that can be installed in the R programming environment suite that includes several tools and built-in functions in order to calculate actual evapotranspiration using surface energy balance models such as METRIC. One of the functions used inside this package is the calculation of albedo with Landsat 8 OLI/TIRS. In developing the associated weights for the coefficient values, prior studies described by Tasumi et al. (2008), and Liang (2001), in addition to The Simple Model of the Atmospheric Radiative Transfer of Sunshine (SMARTS2), was used as a foundation as to further the construction of a new model. The following formula for the use of this method, which can be used in QGIS raster calculator, is the following:

$$\alpha_{short} = 0.246\rho_2 + 0.146\rho_3 + 0.191\rho_4 + 0.304\rho_5 + 0.105\rho_6 + 0.008\rho_7$$

Where:

ρ represents Landsat OLI/TIRS bands 2,3,4,5,6, and 7.

3.6.3 The Chemin Method

Yann Chemin developed an algorithm for the GIS platform GRASS through the built-in image processing function “i.albedo”. Through this application, it is possible to compute broadband albedo from surface reflectance. Due to the calculation of shortwave surface reflectance the chosen range includes the spectral frequencies of 0.3µm to 3.0µm. It is noted within the documentation that for Landsat 8, a temporary algorithm is applied that calculates the weighted average of the reflectance. Within the QGIS raster calculator, the following formula was used in order to derive albedo from this method:

$$\alpha_{short} = 0.058674 + 2.153642\rho_1 - 2.242688\rho_2 - 0.520669\rho_3 + 0.622670\rho_4 + 0.129979\rho_5 - 0.047970\rho_6 + 0.15228\rho_7$$

Where:

ρ represents Landsat OLI/TIRS bands 1,2,3,4,5,6, and 7.

3.6.4 The Liang "Normalized" Method

One of the most established methods for calculating albedo for Landsat 7 ETM+, is through the weighted coefficient methods that were established by Liang (2003). This method uses the following formula, which has been normalized to include only the in-range values:

$$\alpha_{short} = \frac{0.356\rho_1 + 0.130\rho_3 + 0.373\rho_4 + 0.085\rho_5 + 0.072\rho_7 - 0.0018}{0.356 + 0.130 + 0.373 + 0.085 + 0.072}$$

Where:

ρ represents Landsat 7 bands 1,3,4,5, and 7. Note that Landsat band 2 (green) is not used.

However, since the deployment of Landsat 8 OLI/TIRS, the band classification went through a more severe change (See the following tables below). This change was much greater than the previous change to Landsat 7 ETM+ from Landsat 5 TM, meaning in order to reproduce image processing the newly associated wavelengths for each of the multispectral bands needed to become ported, or updated to match. Many of the multispectral bands fall within similar classification and wavelengths between Landsat 7 & 5, however, as shown in the below tables, the above formula can be shown to be closely associated with the band numbers for Landsat 8 (Barsi 2014).

Table 5: Landsat Thematic Mapper (TM) band designation with associated Wavelength.

Landsat 4-5 Thematic Mapper (TM)	Bands	Wavelength (micrometers)	Resolution (meters)
	Band 1 - Blue	0.45-0.52	30
	Band 2 - Green	0.52-0.60	30
	Band 3 - Red	0.63-0.69	30
	Band 4 - Near Infrared (NIR)	0.76-0.90	30
	Band 5 - Shortwave Infrared (SWIR) 1	1.55-1.75	30
	Band 6 - Thermal	10.40-12.50	120* (30)
	Band 7 - Shortwave Infrared (SWIR) 2	2.08-2.35	30

*** TM Band 6 was acquired at 120-meter resolution, but products are resampled to 30-meter pixels.**

Table 6: Landsat Enhanced Thematic Mapper (ETM+) band designation with associated Wavelength.

Landsat 7 Enhanced Thematic Mapper Plus (ETM+)	Bands	Wavelength (micrometers)	Resolution (meters)
	Band 1 - Blue	0.45-0.52	30
	Band 2 - Green	0.52-0.60	30
	Band 3 - Red	0.63-0.69	30
	Band 4 - Near Infrared (NIR)	0.77-0.90	30
	Band 5 - Shortwave Infrared (SWIR) 1	1.55-1.75	30
	Band 6 - Thermal	10.40-12.50	60 * (30)
	Band 7 - Shortwave Infrared (SWIR) 2	2.09-2.35	30
	Band 8 - Panchromatic	.52-.90	15

*** ETM+ Band 6 is acquired at 60-meter resolution, but products are resampled to 30-meter pixels.**

Table 7: Landsat 8 Operational Land Imager (OLI) and Thermal Infrared Sensor (TIRS) band designation with associated Wavelength.

Landsat 8	**Bands**	**Wavelength (micrometers)**	**Resolution (meters)**
Operational Land Imager (OLI) and Thermal Infrared Sensor (TIRS)	Band 1 - Ultra Blue (coastal/aerosol)	0.435 - 0.451	30
	Band 2 - Blue	0.452 - 0.512	30
	Band 3 - Green	0.533 - 0.590	30
	Band 4 - Red	0.636 - 0.673	30
	Band 5 - Near Infrared (NIR)	0.851 - 0.879	30
	Band 6 - Shortwave Infrared (SWIR) 1	1.566 - 1.651	30
	Band 7 - Shortwave Infrared (SWIR) 2	2.107 - 2.294	30
	Band 8 - Panchromatic	0.503 - 0.676	15
	Band 9 - Cirrus	1.363 - 1.384	30
	Band 10 - Thermal Infrared (TIRS) 1	10.60 - 11.19	100 * (30)
	Band 11 - Thermal Infrared (TIRS) 2	11.50 - 12.51	100 * (30)

*** TIRS bands are acquired at 100-meter resolution but are resampled to 30 meters in delivered data product.**

Note that in the above tables, there occur shifts between the various versions of the Landsat satellite for the various bands needed to calculate albedo, which includes the blue, red, near infrared, shortwave infrared 1, and shortwave infrared 2 bands. Using only the blue band as an example, the associated wavelengths for Landsat 5 (TM) and Landsat 7(ETM+) are the same (0.45-0.52). When comparing this wavelength value to the newer Landsat 8 (OLI/TIRS) there exists a subtle difference (0.452 - 0.512). This difference accounts for less than a 2 percent margin, which signifies that the adoption of such a prior method being used to calculating albedo for the newer wavelengths bands of Landsat 8 (OLI/TIRS) should also show a communicated 2 percent difference from the margin. Therefore, it may also be the case, that by finding the ratio difference between all of the various bands needed to calculate albedo, a new weight can be multiplied by this exact ratio difference to limit the subtle distortion effect that may be caused.

By following the above tables, a suitable conversion was developed for the Liang method to calculating albedo for Landsat 7 was created:

$$\alpha_{short} = \frac{0.356\rho_2 + 0.130\rho_4 + 0.373\rho_5 + 0.085\rho_6 + 0.072\rho_7 - 0.0018}{0.356 + 0.130 + 0.373 + 0.085 + 0.072}$$

Where:

ρ represents Landsat OLI/TIRS bands 2,4,5,6, and 7. Note Landsat band 3 (green) is not used.

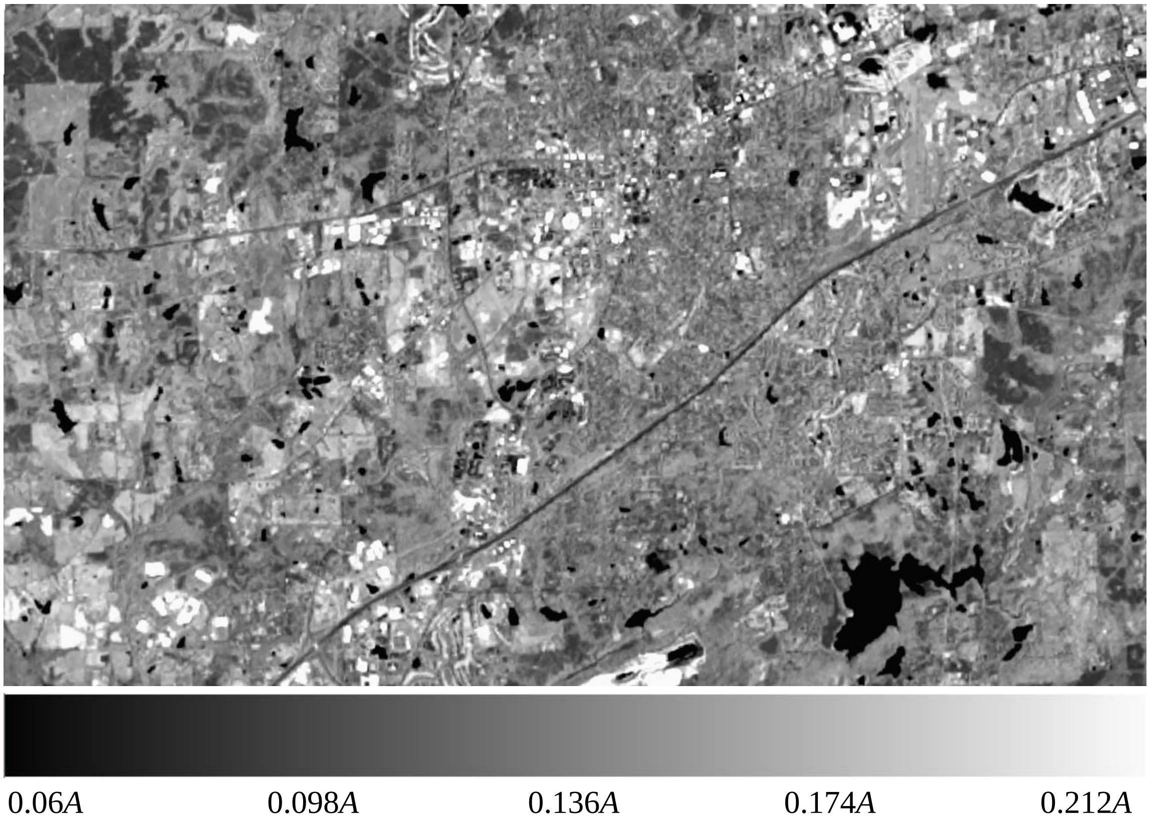

Figure 14: This image portrays the percentage or radiant solar energy reflected in portion to what is received, known as albedo. A high albedo value, say 1, means that 100% energy is reflected, in the case of Auburn University, the high is 21.2% energy reflected.

It can be seen in the above image, that the albedo values for the area of Auburn do not exceed 0.212, which is also associated with urban areas, a minority area which may grow in the future. The representation of such data leads to the implication of greater potential for increasing surface reflectance, with the maximum being 1.0. This represents a 0.788 or 78.8% opportunity of reflectance difference.

3.6.5 Albedo RMSE Analysis

As shown in the below table, the Liang or normalized method to calculate albedo outperformed the other three with a significant margin. Using the Liang method gave a RMSE of 0.029277 or 2.9%. The next best results were given by using the Silva method which had a RMSE of .23 or 23%. This was followed by the Olmedo method which had a RMSE of .237471 or 23.7%. The lowest ranking RMSE score was obtained from using the Chemins Method which gave a RMSE of .60589 or 60.6%.

Table 8: RMSE Results of Differing Albedo Methods

Albedo Method	RMSE Result
Silva	.2300084
Olmedo	.2374712
Chemins	.6058908
Liang	.0292770

As previously discussed, The Liang method was adopted for this study, showing the results that were expected, which assumed nearly a 2% margin, due to the subtle variance associated with the newer band wavelength values. Future studies which account for this 2% difference may build upon the algorithm developed by Liang for Landsat 7, which will be able to improve significantly the corrected values of albedo for Landsat 8. In order to account for such differences, however, a relationship must be defined that shows the statistical difference as well as percentage change from the spectral wavelength functions of Landsat 7 to Landsat 8.

As of an additional note, there does exist one other method for calculating albedo, which is the Tasumi method (Tasumi et al 2008). The reason this method was not chosen as a suitable method is that it is of the author’s opinion that the Olmedo has built upon Tasumi through updated weights, nevertheless, the following method can still be used with the below formula:

$$\alpha_{short} = 0.254\rho_2 + 0.149\rho_3 + 0.147\rho_4 + 0.311\rho_5 + 0.103\rho_6 + 0.036\rho_7$$

Where:

ρ represents Landsat OLI/TIRS bands 2,3,4,5,6, and 7.

3.7 Potential Incoming Solar Radiation

The Sun is the principal energy source for all of the activity on the Earth. Roughly 1370 watts per square meter (solar constant) is constantly being radiated onto Earth’s atmosphere, however, most of this energy never even reach the surface.

Net radiation at the surface is given by:

$$R_n = S_n + L_n$$

Where:

R_n is the net radiation at the surface
S_n is the net shortwave radiation
L_n is the net longwave radiation

There exist three factors affecting the amount of solar radiation that reaches Earth’s surface 1) orientation of the Earth relative to the position of the sun, 2) clouds and other atmospheric interferences and 3) topography. The Earth revolves around the Sun in an elliptical orbit making a complete orbit every 365.25 days, and it is through this orbit that the seasons are caused on the surface. In addition to the Earth revolving around the sun, the Earth is also constantly rotating around its axis turning face toward and away from the sun every 12 hours, creating the day/night cycle. Other planetary characteristics that may occur that can intercept the radiant energy from being absorbed completely on Earth occurs through eclipses. This is an event that occurs when the moon is placed between the Sun and the Earth, but due to the relatively small size of the moon to the Earth, this has a minimal effect.

When the solar energy reaches the top of Earth's atmosphere, this is only the beginning of the process of energy being absorbed. Immediately some of the radiant energy is bounced back into space and some continue inward toward the Earth. Earth's atmosphere is made up of many chemicals and gases, including nitrogen, oxygen, CO_2, and H_20, which each can act upon the incoming radiant energy from the Sun. All of this energy will be reflected back, absorbed within the atmosphere, or absorbed by the surface of Earth. For a more detailed analysis of incoming solar irradiance and the interaction among various surface and atmospheric properties, the appendix of this thesis includes several visual illustrations (See appendix 2, 3, and 4).

Finally, the leftover solar energy that arrives onto the surface of Earth can also act to disrupt any incoming solar radiation. This can include shadows being cast onto the surface property by trees, buildings, mountains or hills. For example, a valley that is obstructed by competing hills will shade the interior of the surface for much of the time when the sun is not directly overhead, causing its solar rays to be able to penetrate within the valley.

By taking into consideration all three of the solar properties and how solar energy can become disrupted, a solar irradiance model created by Hofierka *et al.* (2002) was used for the calculation of incoming solar energy. The model accounts for topography whereby an elevation perimeter may be used, such as a digital elevation model (DEM) or a LiDAR-derived digital surface model (DSM) image. Additionally, the model is able to allow for atmospheric interactions and albedo as well. After the perimeters have been set, the model accounts for the solar position of the inputted time and date perimeters to create output solar radiation values. For this study, a 0.3-meter resolution LiDAR DSM was chosen as the principal perimeter, corresponding to the same date and time captured previously from the Landsat OLI/TIRS satellite, July 28th, 2015. The atmospheric transference rate was chosen as 70%, which is what is expected from reasonableness tests. The model calculated for an entire day (24-hour period), with a temporal resolution set at every half hour increments (0.5h). There is a cost due to processing if a higher temporal resolution is needed, and thus the time period must be chosen to correspond to what both may accurately, and realistically measure the incoming solar radiation. The output given by the model included both diffuse (scattered) and direct solar irradiance and isolation. This process was done through SAGA GIS lighting library, using the module for calculating “Potential Incoming Solar Radiation.” (Böhner 2009)

It was shown in the output images that were created from the solar model, that the campus of Auburn includes many suitable areas for solar insolation. During a typical summer day, most of Auburn’s campus buildings can receive on average 8.01 kWh/m^2 of total incoming solar energy. The results indicate that sufficient energy arrives onto auburn’s surface that could potentially be used to offset radiative heating effects, from solar recapture technologies, such as the installation of solar panels (See figure below). These results are expected, due to the fact that Auburn’s campus is a relatively homogenous elevated area, with little to no shading ever occurring. In addition to this fact, the added dimension that many buildings on campus are not sufficiently elevated as to induce shading to other buildings gives further explanation to the results.

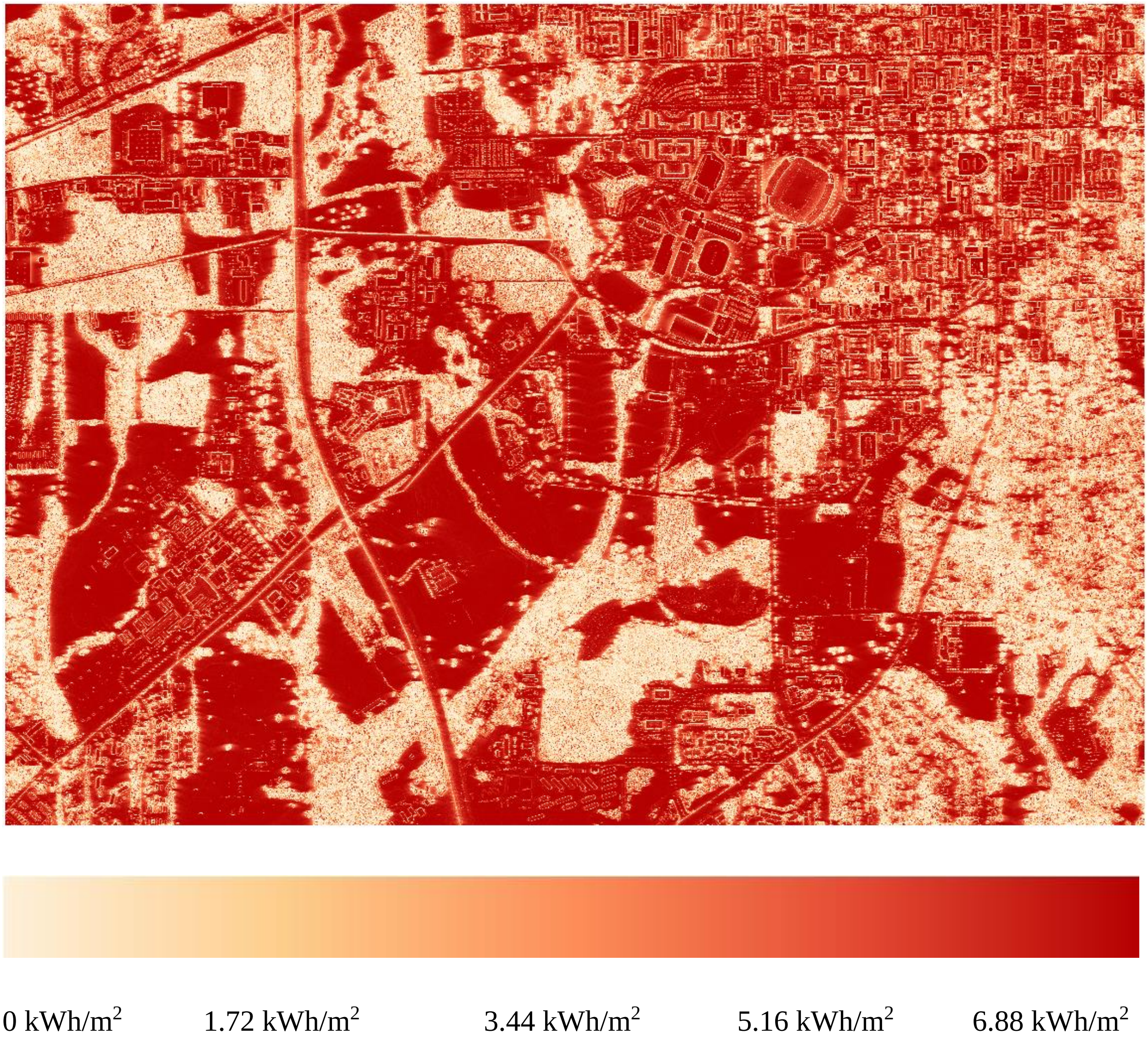

Figure 15: This image captures the direct incoming solar radiation. The temporal resolution of this image is the detail of capture for every 30 minutes on July 28th, 2015. The model also assumes an atmospheric transmittance of 70%.

Diffused radiation indicates the amount of energy that would become refracted onto the surface of the study area. Such type of energy would be expected to be significantly lessened due to the phenomena of absorption that would principally occur from the initial occurrence of solar radiance, which is captured in direct solar insolation (see figures above).

Figure 16: This image captures the diffuse incoming solar radiation. Like the image above, the temporal resolution is at the detail of capture for every 30 minutes on July 28th, 2015. In addition, the model assumes an atmospheric transmittance of 70%.

The importance of having both direct and diffused incoming solar insolation allows for the variable addition of total incoming solar radiation. If only looking at direct solar radiation, then there would be a missing percentage of redirected solar energy being factored into the climate-energy model that gets reabsorbed back into the surface. Thus by factoring both characteristics a more accurate determination can exist.

3.8 Resampling Methods

All of the previously processed images that have been finalized are given at an output of 30-meter by 30-meter resolution per pixel. Nevertheless at this scale, when analyzing rooftops there are several misclassified pixels due to merging having taken place. In order to obtain an even higher resolution, therefore to achieve an even greater depth of analysis, several resampling techniques, which included Bilinear, Bicubic, B-Spline, and Inverse Distance Weighting interpolation, were employed and compared against one another using a RMSE analysis.

In order to resample the processed images containing continuous data (such as temperature, and elevation, or slope) specific techniques are employed, this is due to interpolations generally being applied to “fill in” unknown pixel values effectively downscaling the original image to an even greater resolution. For instance a 30-meter by 30-meters per pixel resolution may accurately be resampled to a 1-meter by 1-meter per pixel resolution image. This task is accomplished by employing a resampling algorithm to all of the pixels of the image, this is usually accomplished by having each pixel being multiplied by a certain weighting factor, which is to say that pixels closer to each other have stronger weights or relationships than pixels that are further from each other (Hwang *et al.* 2004). Additionally, depending on which interpolation method is used, the final processed image will be given as smoother or coarser.

In order to choose the resampling method which exhibit the model’s best fit, an exploratory method of comparing four separate interpolation methods was performed. As shown in the figure below, all of the model’s variables, which were originally outputted by a 30m by 30m spatial resolution were resampled to a 1m by 1m spatial resolution, and were then compared against one another through the use of a RMSE analysis.

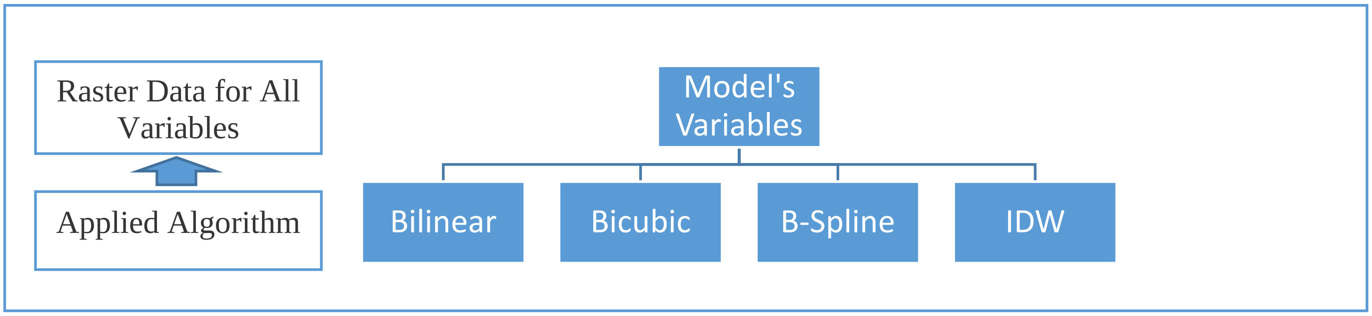

Figure 17: Process of resampling methods employed for each of the model’s variables.

All of the resampling techniques were done after processing the satellite images into the necessary model variables of brightness temperature, NDVI, LSE, LST, and albedo. This was accomplished through the QGIS platform, more specifically within the built-in raster tool functionality of the SAGA Geoalgorithms that is found in the processing toolbox of QGIS.

3.8.1 Bilinear Interpolation

A bilinear interpolation was initially performed as a foundational base of study. When performing a bilinear interpolation, pixel value data is created or filled in, causing the final image to become much smoother. This is accomplished by having the new value of a cell based on an average weighted distance of the four nearest known pixel values (Hwang *et al.* 2004).

This technique is especially useful for continuous data such as elevation and temperature, as is the case for LST and albedo raster.

In order to understand the intuition better for the weighting method being used, it is necessary to think of how the pixels are being filled, which is to say that an empty pixel value within an associated pixel value will be given a weighted output depending on the distance of the other pixels. For instance, if you have a 2x2 pixel frame, with the values 100 and 200 that needs to be downscaled 4x4, this method will fill in those pixels from using the additive of various averages, hence the “bi” in bilinear, in relation to the location of the pixel. An example may be if it is needed to find a pixel value that is a third of the way to the second known pixel value, using 100 and 200 as examples, then 100 is multiplied by 2/3 and 200 is multiplied by 1/3 with the product getting added together, which equals 133. 32.

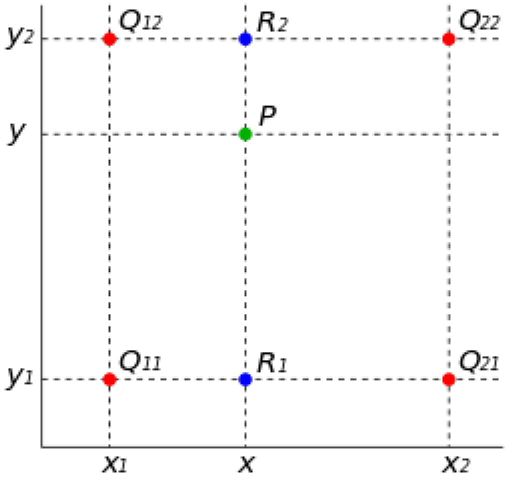

Figure 18: Here is an example of four known pixels’ values (Q_{11} Q_{12} Q_{21} & Q_{22}). In order to interpolate for point P, R_1 & R_2 are averaged on both the X & Y axis (Jitse Nielson 2004).

In the above figure, it is shown how a visual representation might be considered in the context of having 4 known pixel values (Q_{11}, Q_{12}, Q_{21}, and Q_{22}), with the intention of discovering what a predicted or probabilistic value (P) would look like at the interpolation layer (R_1, and R_2). Another important characteristic of bilinear interpolation is the fact that it obtains the pixel samples from a linear set of values, where the pixels are connected in straight lines. Note that in the above image, that no outside pixel values are being calculated for the interpolated pixel value, therefore a linear relationship remains.

3.8.2 Bicubic Spline Interpolation

The use of a bicubic spline interpolation was chosen as a suitable alternative to the bilinear interpolation and was applied to the original raster images. When performing a bicubic interpolation, the new value of a cell, that is a pixel, will be based on fitting a smooth curve through the 16 nearest input cell centers. Through this method, more factors are weighted against the new pixel value, and the plotting of those pixels will appear smooth. Although the use of bicubic interpolation is appropriate for continuous data, it may calculate results that contain values that are outside the range of the original pixels. However, the use of such methods does prove to be geometrically less distorted than the raster achieved by running the nearest neighbor resampling algorithm. With the introduction of nearly four times more calculations per pixel than with bilinear interpolation, employing this method of interpolation does prove to be much more computationally demanding, thus having the disadvantage of requiring more processing time.

Bicubic interpolation is similar to bilinear interpolation except that it uses a polynomial equation which factors in the gradient of the curve of a given pixel. This allows for the two curves of the connecting pixels to become combined into a much more smooth value as well as produce more complexity within values (See figure below). Unlike in nearest-neighbor interpolation, where all of the original pixel values remain intact, both bilinear and bicubic interpolations gives a much smoother image quality. In nearest-neighbor, the reason behind the fact that every original pixel is kept is due to the plotting of each pixel value. These original plots set the upper and lower limits of what will be assigned to any future pixel value. In the case of bilinear interpolation, the plotted lines are connected by slopes and new values can be created in the process, this is also true of bicubic interpolation, except in the latter case, the plotted lines are mathematically much more complex, factoring examples such as derivatives.

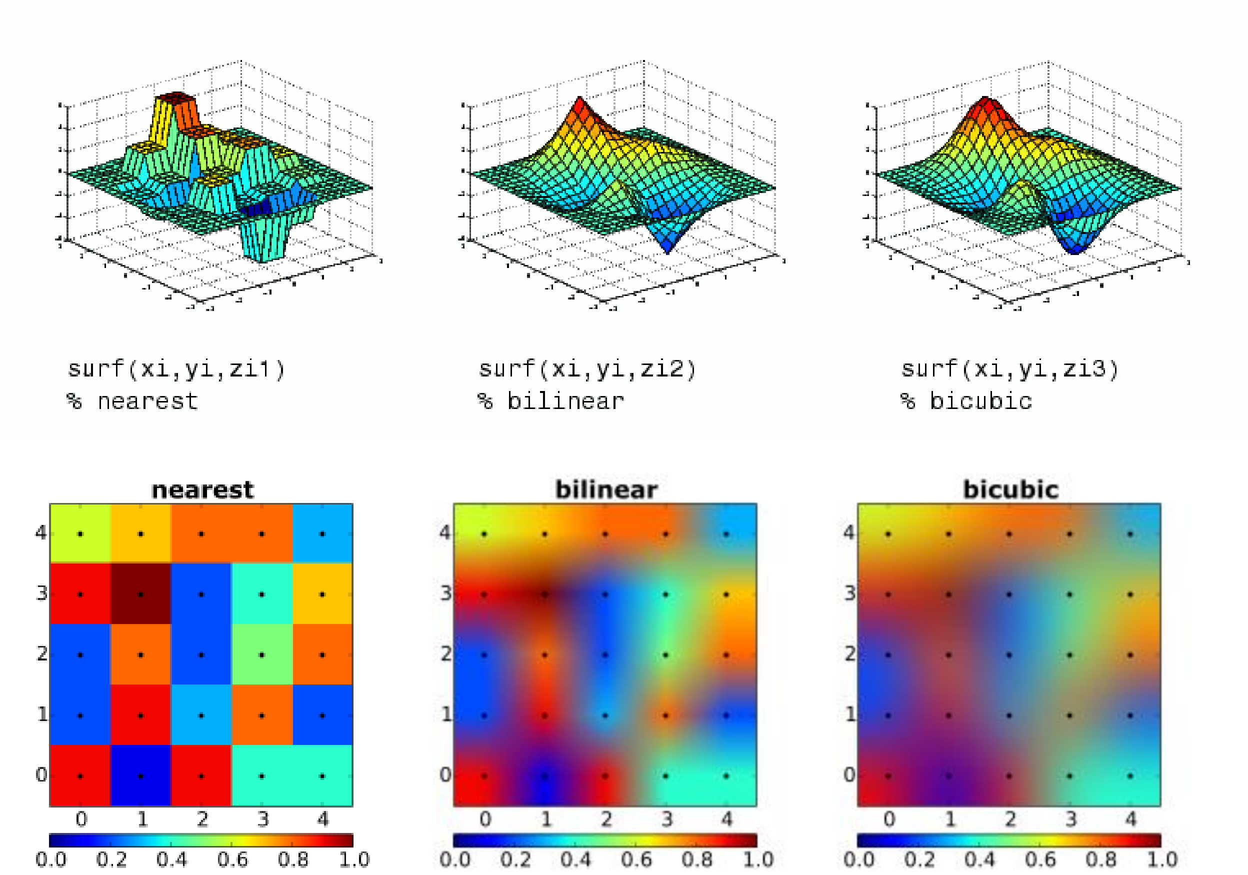

Figure 19: This figure clearly shows the differences, through a visual intuition. Note the differences between the smoothness of the differing methods.

3.8.3 B-Spline Interpolation

Next, in order to obtain data from a more complex interpolation (most smoothing-least artifacts), thus creating variety within the study a B-Spline interpolation was also applied to the raster images. Whereas in the previous two methods of interpolation, namely bilinear and bicubic, a b-spline interpolation can involve n-order or a number of differing situational polygons, it may not be limited to either 4 or 16. A spline is essentially a small section of a curve that goes between two endpoints. These joining points connecting the various polygons are called knots and are what separates splines from other types of interpolations. The overall function of using a spline is to minimize as much surface curvature as possible while creating a smooth surface that passes through every point in the original input. As with Bicubic interpolation, this smoothing represents much more accurately the natural environment, and in the instance of urban areas, where there exists “sharp” drop off points from what is natural and what is man-made, these methods may overemphasize the smoothness of the image.

3.8.4 Inverse Distance Interpolation

Lastly, the original raster files were resampled using an inverse distance weighted (IDW) interpolation. The intuition behind the IDW method for interpolation is simple. Each of the sample points that are available is weighted, which determines the effect of influence one point might have on another relative to their location to each other. The farther away from this point the less influence this point will have on the other to be estimated point. The way in which these sample points are weighted is through the use of being given a weighting coefficient, which controls the perimeter and influence that this will have on the estimated points. Meaning that points nearer the weighted point will be more similar and the points that are farthest away will take on the characteristics of those closer points. As might already be noticed, there are some major limitations to this method. First, if the distribution of weighted points are uneven, where you may have just a few points on the outside and the great majority of points are concentrated in one small area, then obviously the concentrated region will be the more accurate. Another major consideration is that the maximum and minimum values are set at the weighted values, whether this is true or not.

3.8.5 Interpolation Comparison Analysis

In order to compare the four different methods, a RMSE analysis was used. The process included taking the original 30-meter by 30-meter pixel and downscaling the image using SAGA’s resampling algorithm built into the QGIS framework, which gave four separate raster images. 2205 random points were created for each of the 441 original buildings, which were then compared to their residual values, which is the difference between the actual values. The sum of the squares was divided by n, the sample, which then had to be squared to get the RMSE value. Of the four above methods, the inverse distance weight interpolation showed the lowest RMSE of 0.005. This was followed by the bilinear interpolation method with a RMSE of 0.0062. The last two, B-spline and Bicubic spline interpolation methods were equal with a RMSE of 0.0097. In conclusion, the inverse method was chosen as the principal method used to downscale the original 30-meter by 30-meter pixel image to a 1-meter by 1-meter pixel image.

Table 9: Resampling RMSE Comparison Values

Resampling (Interpolation)	RMSE Value
Bilinear	0.0062
Bicubic	0.0097
B-Spline	0.0097
Inverse Distance Weighting	0.005

***172 point values were observed from the original Landsat OLI/TIRS image.**

3.9 Shapefile Data Merge in Research Methods

In order to further analysis the raster output files, it was necessary to combine all values into a master shapefile. The procedure was accomplished through the research tool and zonal statistics function of QGIS. The first procedure was to merge the characteristics of the campus buildings shapefile, and the table for energy use data. All of the Landsat values (NDVI, BT, LSE, LST, & Albedo) had the same coordinate reference system of EPSG: 32616, WGS 84 / UTM zone 16N. In order to merge the raster values with the campus buildings' shapefile the projection of both items needed to be compared against one another. After which, the addition of the solar insolation raster values also needed to become merged into the new shapefile. Since the output raster files employed different methods, the Coordinate Reference System (CRS) was different for the solar insolation values. A reprojection of the shapefile was performed so as to add the new solar energy values. After verifying that all the layers, of both the shapefile attributes to the raster data values, matched, a final merge through the use of zonal statistics was accomplished. The use of the zonal statistics plugin allowed several new values to become merged onto the primary shapefile for study, such as pixel count, sum, mean, median, standard deviation, minimum/maximum values, etc. These procedures finalized the merging of all necessary attribute files to be studied.

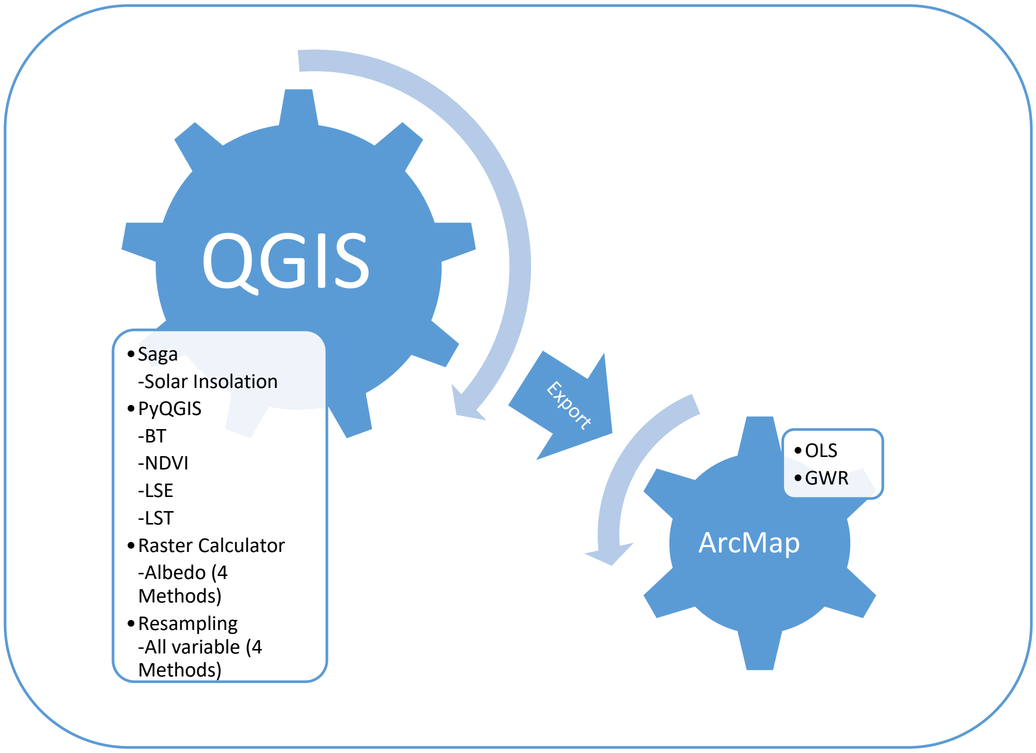

Figure 20: Workflow Process of the relationship between software, variables, and methods.

The two major platforms of research were finalized on QGIS and ArcMap. Remote sensing, image processing, and shapefile data merges were accomplished on QGIS. Afterwards, the final shapefile, which then contained all of the processed raster data, was able to be exported into ArcMap, where statistical methods were applied to obtain meaning from the data originally processed within QGIS.

Chapter 4. Regression of Energy

An ordinary least square (OLS) regression is applied to the study area to find a predictive correlation between LST, albedo, and energy use. The output can be visualized in a chart or graph. The formula that is used is the following:

$$y = \beta_0 + \beta_1 X_1 + \varepsilon$$

Where:

y is the dependent variable
β is the coefficient's weight
X_1 is explanatory variable(s)
ε is the error term or residual value

By employing a regression model, it is possible to explore the spatial relationship of different factors, or variables, in order to be used for future predictions. All regression models include dependent variables (Y), which is what is trying to be predicted, explanatory variables (X), which are variables that hold the influence on the outcome of the dependent variable, coefficients (β), which act as weights toward the explanatory variables (X) relationship to the dependent variable (Y), and finally residuals (ε), which portrays the portion of the dependent variable (Y) that isn't being explained by the model, more specifically, it is where the model has shown under predictions and over predictions from the predicted outcome of the dependent variable.

4.1 Regression Using Ordinary-Least Squares (OLS)

By using OLS as a starting point in the regression analysis, it was possible to test predicted energy values, by testing the dependent variable: Energy Use (for cooling), against the explanatory variables, the following were used: gross area, NDVI, LSE, Albedo, LST, Total Solar Insolation, Elevation, and Age (of Building). OLS provides a global model of the variables, meaning that all variables are included together to explain the predicted outputs. Homogeneity is assumed within this type of analysis. One way of testing this is through spatial autocorrelation. However, before spatial correlation can be tested, it is necessary to set up an initial test to show if the predictive statistical model could benefit from the further use of a spatial regression. This is used for assessing if any relationship exists between the associated variables from the results of the OLS regression. Principally this was accomplished through a scatterplot matrix graph (see figure below)

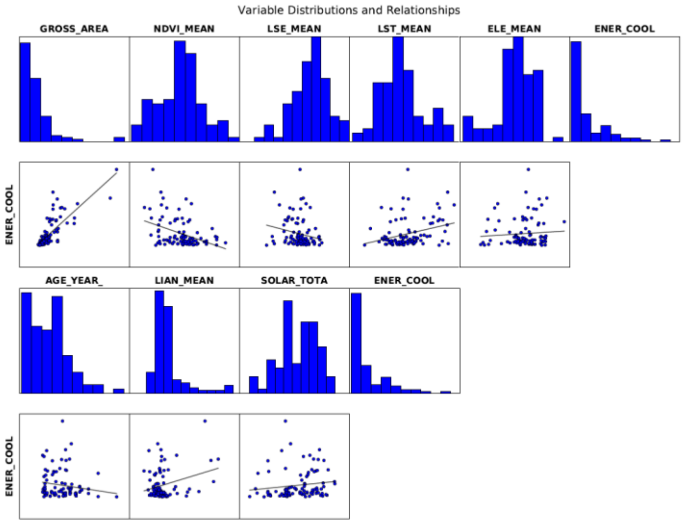

Figure 21: This scatterplot matrix shows the correlational effect between the dependent and independent variables. The diagonal line indicates if the relationship if positive (upwards sloped) or negative (downwards sloped.) in addition to the strength of correlation (degree of slope for the line). Note that there exists a very strong positive correlation between the gross area for the buildings and energy used for cooling.

By running a scatterplot analysis, it was possible to visualize the associated relationship between the dependent variables among all of the independent variables. Of all the independent variables, gross area of buildings showed the strongest correlation. NDVI, LSE, LST, and Albedo showed somewhat moderate correlation. In order to understand all of these relationships better, OLS regression was performed in addition to various statistical tests, including Variance Inflation Factor (VIF), Adjusted R-Squared, Akaike's Information Criterion (AICc), Joint-F and Wald Statistics, Koenker (BP) Statistics, and Jarque-Bera Statistics. Results from this analysis indicated key explanations (See tables below).

Table 10: Summary of OLS Results – Model Variables

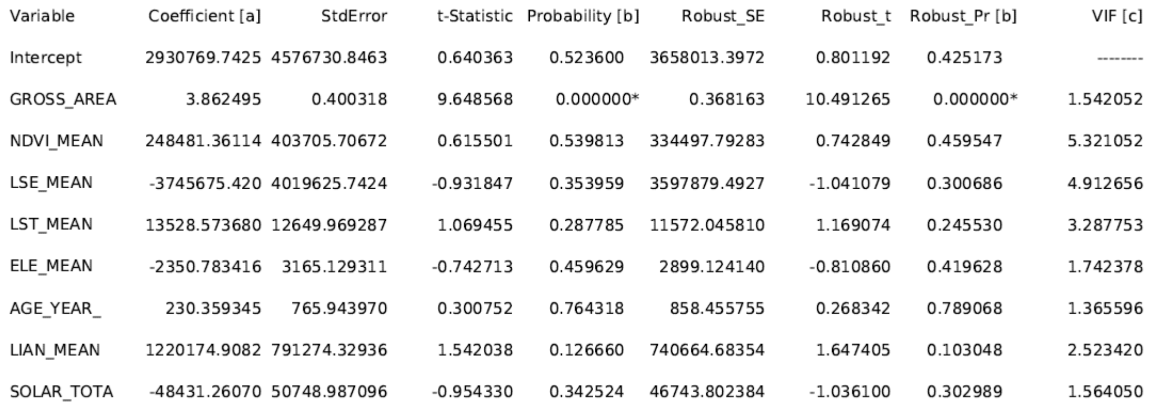

Variable	Coefficient [a]	StdError	t-Statistic	Probability [b]	Robust_SE	Robust_t	Robust_Pr [b]	VIF [c]
Intercept	2930769.7425	4576730.8463	0.640363	0.523600	3658013.3972	0.801192	0.425173	--------
GROSS_AREA	3.862495	0.400318	9.648568	0.000000*	0.368163	10.491265	0.000000*	1.542052
NDVI_MEAN	248481.36114	403705.70672	0.615501	0.539813	334497.79283	0.742849	0.459547	5.321052
LSE_MEAN	-3745675.420	4019625.7424	-0.931847	0.353959	3597879.4927	-1.041079	0.300686	4.912656
LST_MEAN	13528.573680	12649.969287	1.069455	0.287785	11572.045810	1.169074	0.245530	3.287753
ELE_MEAN	-2350.783416	3165.129311	-0.742713	0.459629	2899.124140	-0.810860	0.419628	1.742378
AGE_YEAR_	230.359345	765.943970	0.300752	0.764318	858.455755	0.268342	0.789068	1.365596
LIAN_MEAN	1220174.9082	791274.32936	1.542038	0.126660	740664.68354	1.647405	0.103048	2.523420
SOLAR_TOTA	-48431.26070	50748.987096	-0.954330	0.342524	46743.802384	-1.036100	0.302989	1.564050

This table indicates the variables related to the dependent variable.

Table 11: OLS Diagnostic Tests

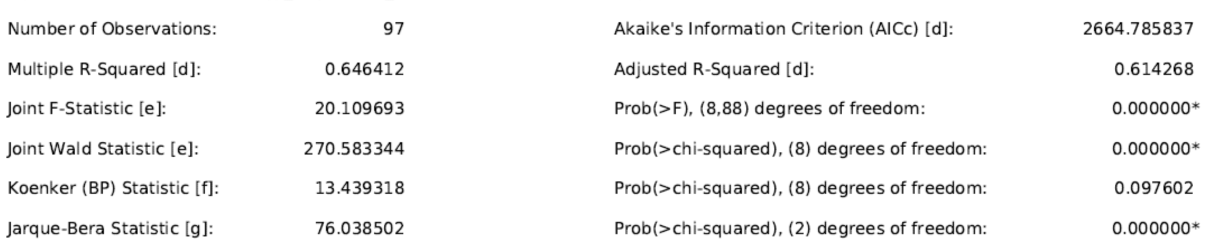

Input Features:	Energy_Regression_4	Dependent Variable:	ENER_COOL
Number of Observations:	97	Akaike's Information Criterion (AICc) [d]:	2664.785837
Multiple R-Squared [d]:	0.646412	Adjusted R-Squared [d]:	0.614268
Joint F-Statistic [e]:	20.109693	Prob(>F), (8,88) degrees of freedom:	0.000000*
Joint Wald Statistic [e]:	270.583344	Prob(>chi-squared), (8) degrees of freedom:	0.000000*
Koenker (BP) Statistic [f]:	13.439318	Prob(>chi-squared), (8) degrees of freedom:	0.097602
Jarque-Bera Statistic [g]:	76.038502	Prob(>chi-squared), (2) degrees of freedom:	0.000000*

Note that within the above diagnostic test, an asterisk symbol (*) indicates statistical significance.

The first check was to accept whether or not the independent variables exhibited the hypothesized relationship. Gross area showed a positive relationship meaning that the larger the building the more energy was used. NDVI also showed a positive relationship, which is expected in relation to the spectral wavelength in consideration. NDVI would be unreliable in the context of classifying “true” urban areas, as this index was originally intended for vegetation only, and thus used primarily for the purpose of urban classification, will show little evidence of correlational effects on the variables. LSE showed a negative relationship with energy use, which is expected, because if an object has a lower emissivity, then this object would be less efficient at transferring the absorbed heat, resulting in more absorbed heat into the energy system. LST showed a positive relationship, which was also expected, due to the fact that a hotter temperature would require more energy used for cooling. Elevation showed a negative relationship, meaning the lower the object was the more energy was used, which could mean that heat is becoming “trapped”, such as occurs during the phenomenon of the urban canyon effect, where wind cannot act as a cooling force. However, this would only somewhat be offset by the fact that higher elevated areas would reach more incoming solar insolation and thus act to provide shade to lower lying areas. Age was shown to have a positive relationship with energy use, meaning that the older the building is, the more energy used, and expected result due to wear and tear occurring in the building with the passage of time leading to greater thermal efficiencies, especially in windows, walls, doors, and roofs. Another important characteristic of the age variable was that it had the second lowest weighting factor coefficient of 230.4, among all of the variables, with the gross area having the lowest coefficient’s weight and thus most significant of 3.8. Albedo was shown to have a positive relationship, which would seem unexpected since a high albedo would signify that more energy is being reflected thus preventing energy from ever becoming absorbed in the first place, but it is also the case that the more industrial/utility building on campus also showed the highest albedo values whereas the smaller residential buildings showed the lowest albedo. It is important to not consider this variable in isolation and as such within this context, it does make sense as to why a higher albedo would show a positive correlation. Finally, total incoming solar insolation, which has been modeled as incoming solar radiation (both direct and diffuse), was shown to have a negative correlation with energy use. Another seemingly unexpected result in isolation, but by understanding the situation occurring, the same effect causing elevation to show a negative relationship will also be the same phenomenon acting on the solar isolation variable (See tables above).

The VIF value signals whether or not the model’s variables show the relationship of multicollinearity, meaning that there may be redundancy among variables both explaining similar, if not the same, instances. A smaller VIF value means that there is less of a chance of an over-count bias, where any variables larger than 7.5 (ESRI 2017) would need to be removed. All of the variables are shown to be safe from bias, however, it is noted that both the variables of NDVI and LSE do appear to be explaining similar incidents within the model, but not so much as to lead to bias. This is very much accepted due to how LSE was calculated strongly linearly based off of NDVI, with only a small portion becoming logarithmically different within the algorithms’ context. It is, however, evidenced that the urban areas would show the largest gains from these differences, which is why the two variables are clear from bias.

The last test that can be used on all of the variables is a test of significance. As already been stated, with the exception of the gross area variable, all of the rest of the variables were not shown to be statistically significant in helping explain the models' behavior outputs, however, due to the principle nature of this study, the importance of such variables were needed to be included as to be able to demonstrate the climatological relationship of energy use. If the only goal was to understand energy use, then it could be argued that such variables are not needed and thus may be removed.

A fundamental method of assessing the model's performance or explanatory power is by identifying the Multiple R-Squared and Adjusted R-Squared value. Although the Multiple R-Squared value will always be higher than the Adjusted R-Squared value, due to the reflection of complexity being modeled, an Adjusted R-Squared value reasonable gives what percentage is being explained by the model. In this test, the Adjusted R-Squared was shown to be 0.614268, meaning that the variables are acting to explain nearly 61 percent of the independent variable's outcome. Generally, an Adjusted R-Squared value of 0.5 or higher, is considered a well-behaved model, because at least half of the model is being explained, nevertheless, depending on the complexity of the system being studied, this value is subjective and can be determined on a case by case basis. This model has a predictive capability of 61 percent, however, there is the limitation of having only one variable shown to have overall statistical significance, which is Gross_Area (of the building). More studies will be needed as to show whether or not an adjusted R-Squared value of .61 should be considered an overall good predictor, although it seems acceptable within the context of this study. Nevertheless, this model's predictive capability is stated at being at nearly 61 percent of the energy used for cooling. Additionally, it is possible to choose the best performing model by comparing different models to the Akaike's Information

Criterion (AICc) value. In this test, the model returned an AICc value of 2664.785837. In the absence of any comparative model, this does not add to the analysis of this study.

Furthering the analysis, it is shown that both the Joint F-Statistic and Joint Wald Statistic are statistically significant. This finding must be checked against the Koenker (BP) Statistic for statistical significance as well. Since it is shown that the Koenker (BP) Statistic is not statistically significant, then it means both the Joint F-Statistic and the Joint Wald Statistic, which are tests of the models overall statistical significance, can be accepted for the study. Furthermore, the Koenker (BP) Statistic (Koenker's studentized Bruesch-Pagan statistic) is used to assess stationarity, meaning that all statistical properties are constant over space and time. If it was shown that the Koenker (BP) Statistic was statistically significant as well, then it would signify that at least some, if not all, of the independent variables and the dependent variable, are non-stationary, meaning that some of the explanatory power of the variables may be stronger or weaker depending on geographic space or time. Regression tests that show the Koenker (BP) Statistic as being statistically significant can be further analyzed by performing a Geographic Weighted Regression (GWR). Since this is not the case in this situation, all of the explanatory variables are stationary, and operate consistently regardless of the specific geographic location being studied.

In the context of OLS regression being used in spatial statistics, the Jarque-Bera Statistic tests whether or not the residuals are normally distributed when plotted as a curve function. If when plotted, the residuals do show a Gaussian distribution or a "normal" bell curve, then the model is not biased, and the Jarque-Bera Statistic would not be statically significant. Another importance of the Jarque-Bera Statistic test, is the indication of whether or not the model has been misspecified (meaning a key variable is missing from the model) when tested together with Spatial Autocorrelation, or if the model is trying to define for a nonlinear relationship, which would be shown when key explanatory variables show strong heteroscedasticity or skewness of the curve. It is important to note that in the case of nonlinear relationships, OLS, which is a linear regression model, should be suspended instead for the use of a nonlinear regression model, otherwise the variables may be recomputed, so as to be transformed usually logarithmically or exponentially. Since the analysis has shown the Jarque-Bera Statistic is statically significant, further analysis must be completed, upon whether or not spatial autocorrelation exists. Therefore it may be assumed that there are sufficiently key variables that are not being used to show predicted outcomes of the dependent variable, which has already been shown by the adjusted R-squared, explaining 61% of the model’s outputs. These unknown variables may include other building characteristics, such as window, wall, and roof thermal insulation properties (R-values). Additionally, none of the variables appear to exhibit strong heteroscedasticity, indication that a nonlinear relationship does not exist.

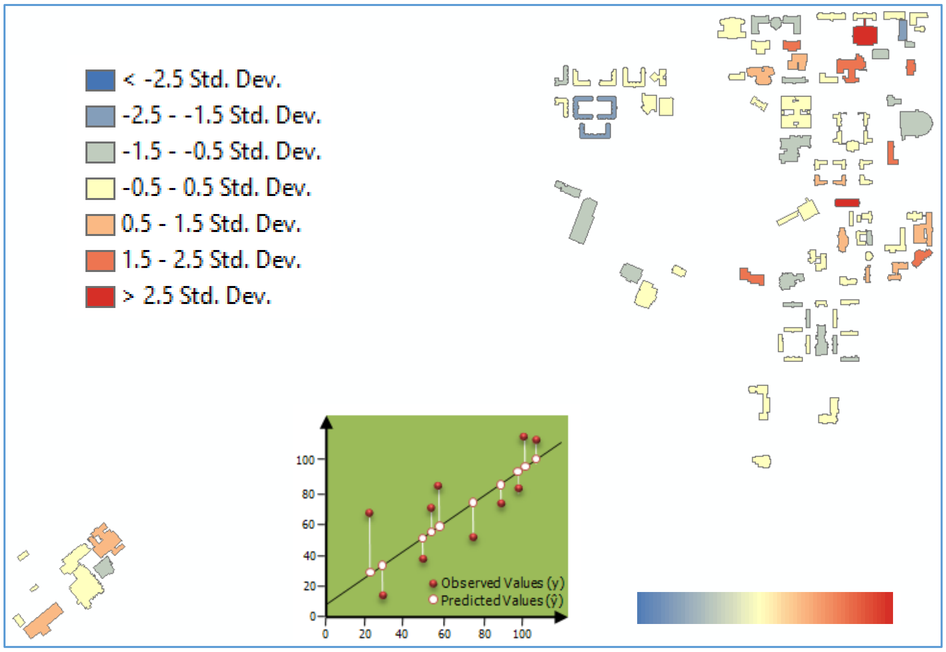

Figure 22: Residual map showing greatest deviation has occurred for over/under predictions.

In order to test for residual spatial autocorrelation, it is possible to compute Global Moran's I (Index) to be able to understand if clustering is occurring. Sometimes it is possible to be able to look at a map of the residuals (See figure above) to visually notice whether or not spatial clustering is occurring, but a more objective, and thus trusted method, is by deriving the actual Moran's I value. If it is true that statistically, significant clustering is occurring for the residuals of the regression outcome, then a key variable is missing, thus it is said that the model is misspecified.

This study's results have shown that the Critical Value (z-score) is 1.038557, which fall within the level of randomness needed for statistically significant clustering to not occur. The value that is needed to ensure statically testing is met is for the range of values to fall between -1.65 to +1.65 (See figure below).

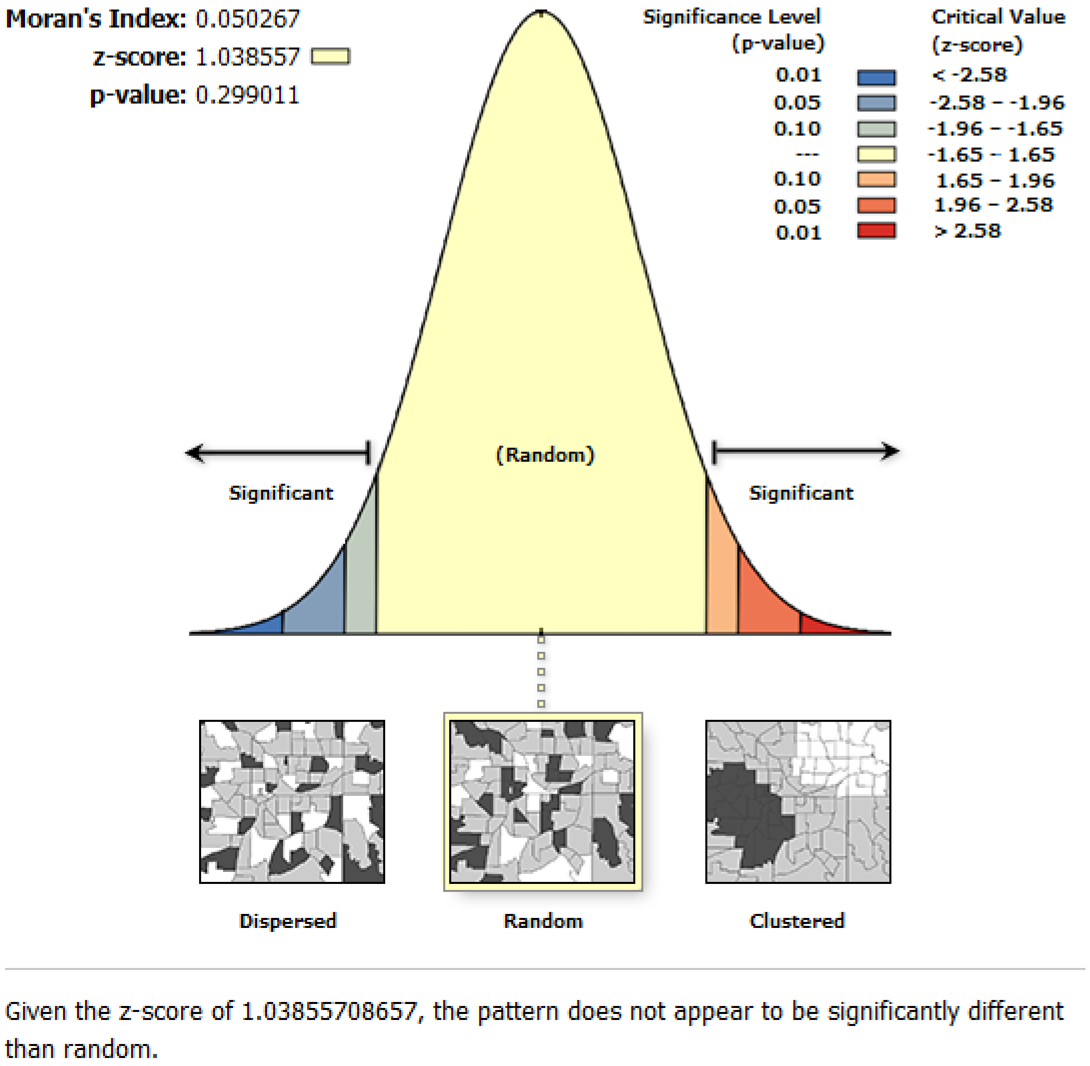

Moran's Index: 0.050267

z-score: 1.038557 🟨

p-value: 0.299011

Significance Level (p-value)		Critical Value (z-score)
0.01	🟦	< -2.58
0.05	🟦	-2.58 - -1.96
0.10	🟩	-1.96 - -1.65
---	🟨	-1.65 - 1.65
0.10	🟧	1.65 - 1.96
0.05	🟧	1.96 - 2.58
0.01	🟥	> 2.58

Given the z-score of 1.03855708657, the pattern does not appear to be significantly different than random.

Figure 23: Moran's I Spatial Autocorrelation graph signifying whether the model exists clustering.

By plotting a graph of the residuals, it is possible to determine if the statistical model that has been developed is properly specified. The shape of these residuals, where the model has underpredicted values and over predicted values, should be random and take the shape of a bell curve. Although no model will ever be perfect, nevertheless, the shape from the plotted residuals should achieve as close as random as what is reasonable. In figure 24, the residuals do give the appearance of a bell curve, which is shown from the blue "normal" curve line. In addition to a visual histogram, this should be checked in relation to the given value of determining from the Jarque-Bera test.

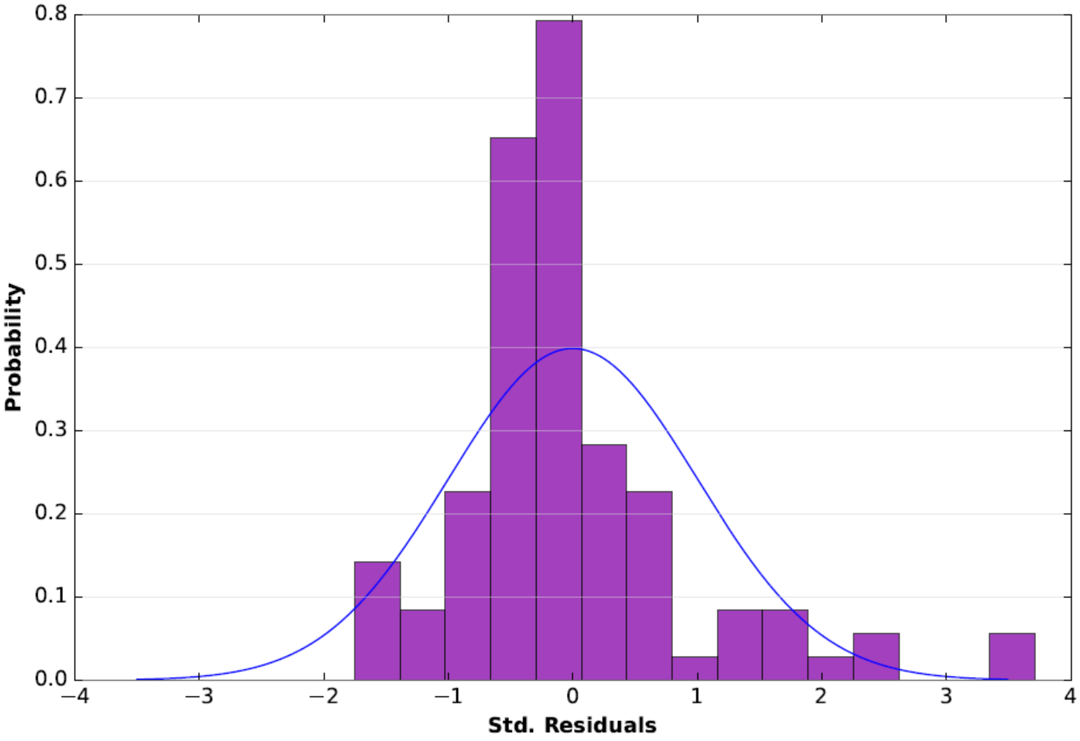

Figure 24: The purple bars presented the plotted distribution of the residuals. These can be compared against the ideal Gaussian distribution, which is represented as a blue curve line. Since the two appear to match it can be said that the explanatory variable in this model is properly specified.

The figure shows the graphical representation that is derived from the Koenker diagnostic test, which details the relational changes that are being modeled through the study area or stationarity. The plotted dots from the residual outputs should show a random distribution, with no shaping occurring, such as is the case in the figure. If it were determined that there existed a clear heteroscedasticity from the plotted residuals, such as a cone shape forming to the left, then the model would be exhibiting nonstationarity (i.e. residuals that vary intrinsically across space).

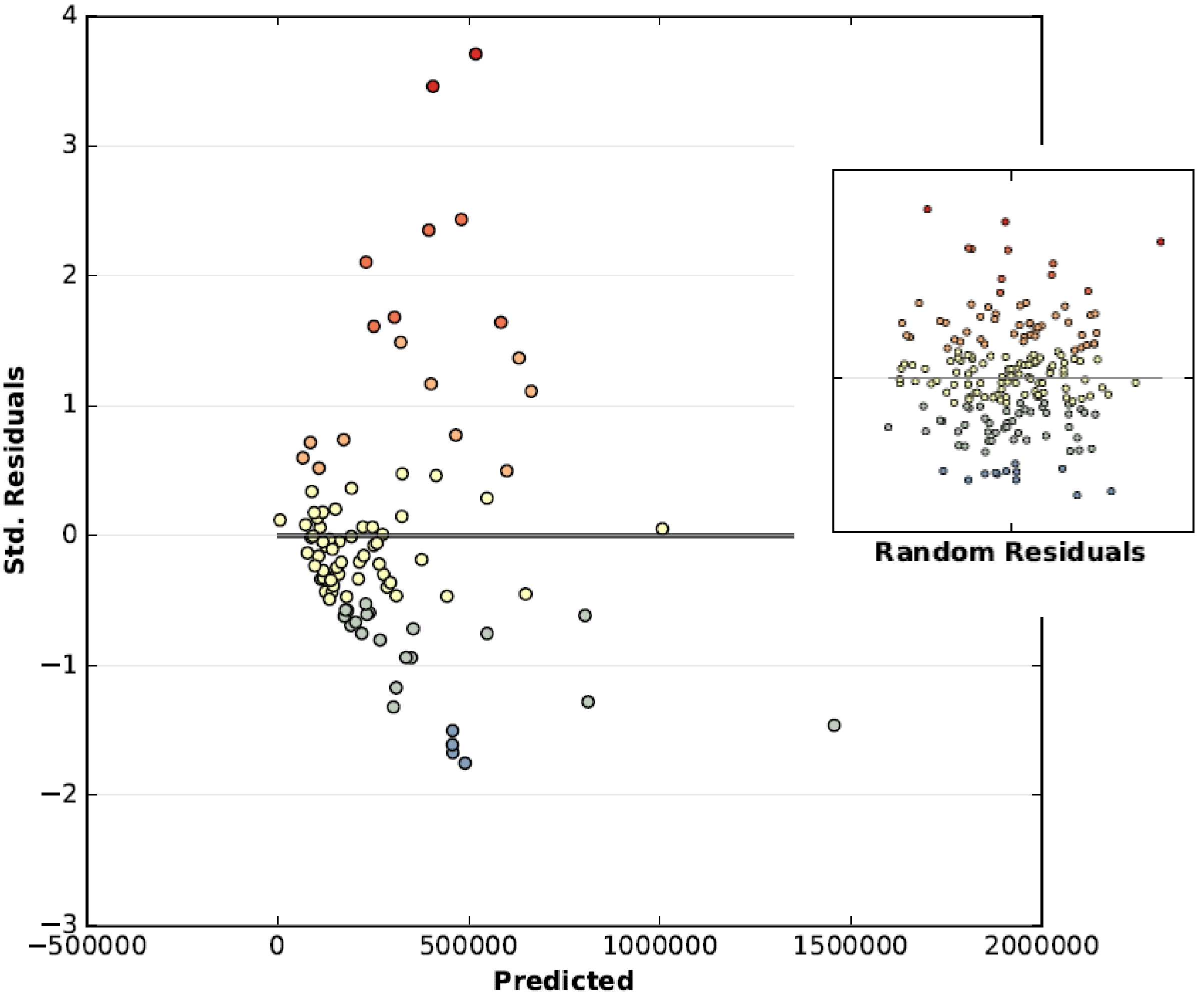

Figure 25: This graph shows the plots of the residuals from the model. When a model is properly specified, this graph shows almost no structure and appears to be random. Otherwise, nonstationarity may be occurring, which could have the benefit of running a GWR. Note how a random plot of residuals may appear on the right.

Note that the above image does not show any true bias occurring. The residuals do appear random and do not show shape, such as the shape of a cone. This pattern indicates that the model is properly fitted and that indeterminate to geographic space, the residual outputs will look evenly distributed.

4.2 Regression Model Comparison

Due to the specification of the prior model's results, a logarithmic transformation was performed on the variable of gross building area, to shift the heteroscedasticity to measure with a normal distribution curve. The process of this transformation did, in fact, shift one of the most important variables in the prior model to the right as seen in the below figure.

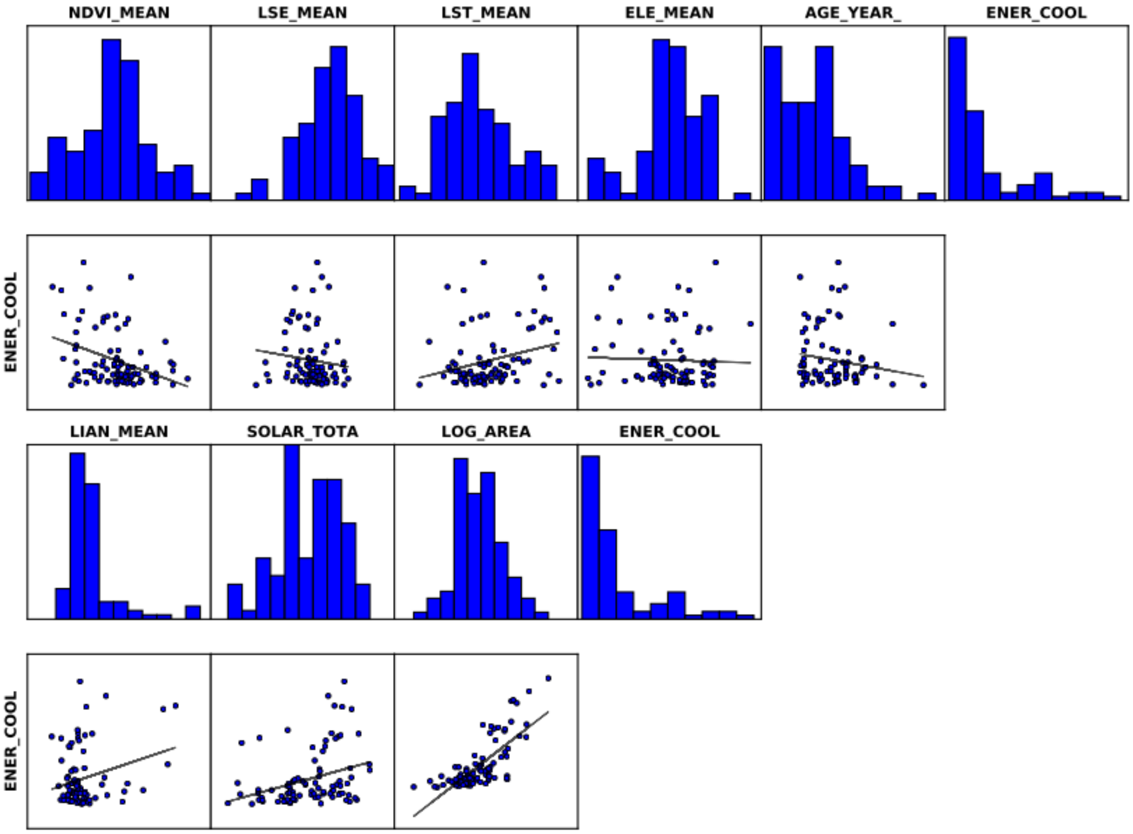

Figure 26: Transformed Building Gross Area Variable Scatterplot

The model was able to outperform the prior model's results as shown from the table below. As noted, the AICc value is lowered by a significant margin, showing a stronger model in general. In addition, prediction power of the model, through the Adjusted R-Squared value is shown to be lowered, however, it still remains in a suitable range. Biases of the residuals are not present in either model. Another significant discoverable difference is that of the stationarity of both models. Where the original model A was shown to be stationary from the Koenker (BP) Statistic, the new transformed model B is shown to be non-stationary, meaning that the explanatory variables may hold some degree of variance in regards to predictability against the dependent variable in regards to specific location. This can be further analyzed through a geographically weighted regression. The other significance of the Koenker (BP) Statistic is in the refutation of both the Joint F Statistic and the Joint Wald Statistic, which can only assess the models overall statistical significance if and only if the Koenker (BP) Statistic is shown to not be statistically significant. The final difference that exists from both models is the results from the Jarque-Bera Statistic. Having the Jarque-Bera Statistic measure as not being statistically significant details the facts that the model is being properly specified (key variables are not missing), and that a nonlinear relationship does not exist.

Table 12: Comparison of OLS Models

Statistics	Original Model A	Transformed Model B
Akaike's (AICc)	2664.785837	2454.956981
Adjusted R-Squared	0.614268	0.589439
Z-Score	1.560348 (Non Biased)	1.249627 (Non Biased)
Joint F-Statistic	Statistically Significant	Statistically Significant
Joint Wald Statistic	Statistically Significant	Statistically Significant
Koenker (BP) Statistic	Not Statistically Significant	Statistically Significant
Jarque-Bera Statistic	Statistically Significant	Not Statistically Significant

4.3 Regression Using Geographically Weighted Regression (GWR)

As already been noted, the first order to running a GWR (Brunsdon *et al.* 1996), is to first run an OLS regression, where it is possible to run a Koenker test in order to see if all the variables are non-stationary. GWR can help in explaining whether or not the explanatory variables have a strong predictive relationship with the dependent variable in certain geographic locations. In the case of LST, it might be reasonable to assume the case that LSE will show a strong predictive relationship downtown, where an associated Urban Heat Island Intensity (UHII) would be strongest. In the original Model A OLS analysis, it was shown through the Koenker (BP) Statistic that all of the key explanatory variables were stationary. Therefore the model would not benefit significantly by performing a GWR. However, through the transformed variable Model B, the Koenker (BP) Statistic was shown to have instances of non-stationarity.

It was possible to run a GWR analysis through only one key explanatory variable, which was the logarithmically transformed gross area of buildings. When other explanatory variables were used, there most probably existed severe local multicollinearity within the model's design, signifying that there were key explanatory variables overlapping in their predictive power, thus creating redundancy within the GWR analysis. Once the design problems were fixed, the residual map output showed geographically where the gross area of the buildings played a more significant role on the energy use of the campus (See figure below).

Figure 27: A residual map indicating geographic influences from the model predicted outcomes.

The results of the GWR analysis were performed with the Bandwidth parameter chosen from the AICc method. This output gives the smoothness of the representation being presented, with a fixed distance measured in meters. The output, therefore, was calculated as 18,095.08 meters. The residual squares test indicates the model's fit to the actual observed data. A smaller number indicates a better overall fit. A number of 2,598,177,193,250.9873 would be considered very high. The effective number value can be used for further diagnostic measures and reflects the tradeoff within the model's overall fit. Sigma values indicate the estimated standard deviation of the residuals, where a smaller value is preferred. A value of 171,133.7875 would be considered as also being very high. Again the AICc value helps to determine the overall model's performance, which is shown as to not have improvement, with a value of 2455.6712. Lastly, the

R2 Adjusted value also give detail to the model's performance, however, in the case of a GWR analysis, the AICc value would become more reliable of a measure (See table below).

Table 13: GWR Diagnostic Test

Statistics	Score
Bandwidth (Neighbors)	18095.077005254832
Residual Squares	2598177193250.9873
Effective Number	2.2849621634233452
Sigma	171133.78745271239
AICc	2455.671201751858
R2 Adjusted	0.54325974475834582

In conclusion, the additional information provided from the GWR regression is still limited. Although it can be shown that non-stationarity exists, meaning that the model's parameters exhibit a total better fit in certain geographic spaces above other occurrences on the map, the overall parameters are still limited, as shown by the evidence of missing variables, which are still key to accurately determining the energy-use modeling of Auburn's campus. Therefore more data is necessary in order to derive significant results that can be used in decision making.

Chapter 5. Significance

Primarily, it has been shown that the use of a cool roof may not be a suitable mitigation strategy against Urban Heat Island intensity as originally intended. The properly specified regression model showed little relationship between the variables of Albedo, LST, Solar Insolation and Energy Use. This would signify that a more reflective roof would contribute little to lowering the energy use for the buildings on Auburn University's campus, which would not disrupt the feedback effect of an Urban Heat Island to continue to occur.

Secondly, due to the results of the regression models test for stationarity, it would not seem that some buildings would benefit significantly from the adoption of cool roofs to others. Therefore, even overall cool roofs do not seem to be a suitable geoengineering technique for use of the buildings on the campus of Auburn University.

Thirdly, a suitable method has been established for the use of calculating albedo with Landsat 8 data, which was previously reserved for prior Landsat data or alternative methods of calculating reflectance, such as the use of tasseled cap brightness.

5.1 Future Studies

It is reasonable to expect the thermal insulation factors of the buildings' properties to play a more significant effect on energy use than climatic environmental factors. Due to this phenomenon, it is necessary to include other building characteristics to future studies. Some such building characteristics may include number and size of windows, the building's material, thermal insulation property (R-Factor), and the building's population (number of daily residents with traffic in and out of the building).

Additionally, due to the large exposure on both direct and diffuse solar insolation, the marginal benefit from the installing of cool roofs may not outperform the energy capture from the installation of solar energy panels. Due to the continued decrease in costs for solar energy, it may become much more feasible to choose to install solar roofing. The achieved outcome of such work may be such that, the energy saved from installing cool roofs, will be much less than the energy gained from the capture of solar energy panels.

The primary goal of finding the relationship between LST, albedo, solar irradiance, and energy has been determined by using statistical regression. These results can provide details on the type of buildings which may be best for adopting UHI mitigation strategies. By applying a regression analysis, trend data can be used to set predictors and estimators that will allow researchers and decision makers the ability to observe energy consumption patterns as it relates to the natural climate and anthropogenic effects as well.

5.2 Conclusion

The beneficial use of cool roofs have been proposed in areas like California and even Chicago, yet the data for Auburn University does not seem to exhibit the same benefit from cool roofs. The reason for some of this difference may be in the regional differences from Auburn's climate to the others. Other factors to consider are that cool roofs in this study are being modeled, with the goal to find a relationship between Albedo and energy use, meaning that the defined "Cool Roofs" are not being directly studied. There exist no cool roofs on Auburn University's campus, and so the hypothetical value must be modeled through regression.

However, it has been shown by the temperature difference between the remotely sensed images of brightness temperature and LST, that there exists a significant temperature difference. This signifies that emissivity, one part of the equation for cool roofs, does play a large role in the actual LST of Auburn's campus, and as such may act to mitigate against UHII effects. This process, however, would be costly, and may only become accepted during the process of new roof construction or roof repair and reconstruction.

Nevertheless, the increasing use of energy in urban areas will continue to pressure the sustainable development of these areas. Pollution that is being emitted from the increased energy use will continue to present real tangible problems, adding to the intensification of UHI through the positive feedback effect of the creation of GHGs which act to trap more heat, that needs to be offset by increased energy demand used for cooling, thus creating more GHGs and pollutants (Menon *et al.* 2010). By looking at solutions of reducing energy use, these sustained negative effects can be turned around, which will greatly reduce energy use and therefore reduce the associated negative effects caused by UHII. Although it has been shown that the installation of cool roofs for Auburn University does not significantly counteract the UHII problem, there may be other solutions in the form of increased energy efficiency of the building's construction, and the installation of solar panels on the building's rooftops. Both of these circumstances would act to positively counteract the negative balance caused from UHII, by capturing more energy on sunny days, which would be when energy use would be highest, as well as having the ability to retain cooler internal building temperatures from increased thermal efficiencies.

The era in which we currently live has been termed the Anthropocene period (Crutzen 2006), a time when humans have had the greatest impact on their natural environment, more so than any other time in history. This human impact on the natural environment has led to devastating consequential effects that if left unchecked, will surely continue to escalate. Never has the case been so relevant than within the study of UHII, where the rapid pace of urbanization in the 21st century is causing environmental stress to be placed on the microclimates of the world. The necessity to employ mitigation strategies to ameliorate these harmful effects has never been of more paramount importance and demands immediate action. Cool roofs may still play an instrumental role in the future for solving the UHII problem, however, it has been shown for Auburn University that it may no longer be considered a suitable alternative from the investment of resources from building insulation and solar roofing.

References

Ahrens, C. Donald. "Meteorology today." *An Introduction to Weather, Climate, and the Environment, 8th ed., Thomson Brooks/Cole, Belmont, California, USA* (2007).

Akbari, Hashem. "Energy Saving Potentials and Air Quality Benefits of Urban Heat island mitigation." *Lawrence Berkeley National Laboratory* (2005).

Akbari, Hashem, Surabi Menon, and Arthur Rosenfeld. "Global cooling: effect of urban albedo on global temperature." *Lawrence Berkeley National Laboratory* (2008).

Akbari, Hashem, Surabi Menon, and Arthur Rosenfeld. "Global cooling: increasing world-wide urban albedos to offset CO 2." *Climatic Change* 94, no. 3 (2009): 275-286.

Arnfield, A. John. "Two decades of urban climate research: a review of turbulence, exchanges of energy and water, and the Urban Heat Island." *International journal of climatology* 23, no. 1 (2003): 1-26.

Bard, Edouard, Grant Raisbeck, Françoise Yiou, and Jean Jouzel. "Solar irradiance during the last 1200 years based on cosmogenic nuclides." *Tellus B* 52, no. 3 (2000): 985-992.

Barsi, Julia A., Kenton Lee, Geir Kvaran, Brian L. Markham, and Jeffrey A. Pedelty. "The spectral response of the Landsat-8 operational land imager." *Remote Sensing* 6, no. 10 (2014): 10232-10251.

Berdahl, Paul, and Sarah E. Bretz. "Preliminary survey of the solar reflectance of cool roofing materials." *Energy and Buildings* 25, no. 2 (1997): 149-158.

Bewoor, Anand K., and Vinay A. Kulkarni. *Metrology and measurement*. McGraw-Hill Education, 2009.

Böhner, Jürgen, and Oleg Antonić. "Land-surface parameters specific to topo-climatology." *Developments in soil science* 33 (2009): 195-226.

Bozonnet, Emmanuel, Maxime Doya, and F. Allard. "Cool roofs impact on building thermal response: A French case study." *Energy and Buildings* 43, no. 11 (2011): 3006-3012.

Brunsdon, Chris, A. Stewart Fotheringham, and Martin E. Charlton. "Geographically weighted regression: a method for exploring spatial nonstationarity." *Geographical analysis* 28, no. 4 (1996): 281-298.

Budikova, Dagmar, C. M. Hogan, M. Hall-Beyer, G. Hassan, and M. Pidwirny. "Albedo. The Encyclopedia of Earth." *Washington, DC: Environmental Information Coalition, National Council for Science and the Environment* (2010).

Castanho, Andréa DA, and Paulo Artaxo. "Wintertime and summertime São Paulo aerosol source apportionment study." *Atmospheric Environment* 35, no. 29 (2001): 4889-4902.

Chander, Gyanesh, Brian L. Markham, and Julia A. Barsi. "Revised Landsat-5 thematic mapper radiometric calibration." *IEEE Geoscience and remote sensing letters* 4, no. 3 (2007): 490-494.

Crawford, Todd M., and Claude E. Duchon. "An improved parameterization for estimating effective atmospheric emissivity for use in calculating daytime downwelling longwave radiation." *Journal of Applied Meteorology* 38, no. 4 (1999): 474-480.

Conrad, O., Bechtel, B., Bock, M., Dietrich, H., Fischer, E., Gerlitz, L., Wehberg, J., Wichmann, V., and Böhner, J. (2015): System for Automated Geoscientific Analyses (SAGA) v. 2.1.4, Geosci. Model Dev., 8, 1991-2007, doi:10.5194/gmd-8-1991-2015.

Crutzen, Paul J. "The “Anthropocene”." In *Earth system science in the Anthropocene*, pp. 13-18. Springer Berlin Heidelberg, 2006.

Fleming, David. "Ikonos DN value conversion to planetary reflectance." *CRESS Project Paper, Commercial Remote Sensing for Systems Science, Maryland, US., Available online at http://www. geog. umd. edu/cress/papers/guide _dn2pr. pdf* (2003).

Foody, Giles M. "Status of land cover classification accuracy assessment." *Remote sensing of environment* 80, no. 1 (2002): 185-201.

Georgescu, Matei, Philip E. Morefield, Britta G. Bierwagen, and Christopher P. Weaver. "Urban adaptation can roll back warming of emerging megapolitan regions." *Proceedings of the National Academy of Sciences* 111, no. 8 (2014): 2909-2914.

Haberl, J., and S. Cho. 2004. Literature Review of Uncertainty of Analysis Methods (Cool Roofs), Report to the Texas Commission on Environmental Quality. Energy Systems Laboratory, Texas A&M University, College Station, TX.

Haines, Andy, R. Sari Kovats, Diarmid Campbell-Lendrum, and Carlos Corvalán. "Climate change and human health: impacts, vulnerability, and public health." *Public health* 120, no. 7 (2006): 585-596.

Hofierka, Jaroslav, and Marcel Suri. "The solar radiation model for Open source GIS: implementation and applications." In *Proceedings of the Open source GIS-GRASS users conference,* vol. 2002, pp. 51-70. 2002.

Hwang, Jung Woo, and Hwang Soo Lee. "Adaptive image interpolation based on local gradient features." *IEEE Signal Processing Letters* 11, no. 3 (2004): 359-362.

Isaya Ndossi, Milton, and Ugur Avdan. "Application of open source coding technologies in the production of land surface temperature (LST) maps from Landsat: A PYQGIS plugin." *Remote Sensing* 8, no. 5 (2016): 413.

Jacobson, Mark Z., and John E. Ten Hoeve. "Effects of urban surfaces and white roofs on global and regional climate." *Journal of Climate* 25, no. 3 (2012): 1028-1044.

King, James R., and Donald S. Farner. "Energy metabolism, thermoregulation and body temperature." *Biology and comparative physiology of birds* 2 (1961): 215-288.

Kimura, Fujio, and Shunji Takahashi. "The effects of land-use and anthropogenic heating on the surface temperature in the Tokyo metropolitan area: A numerical experiment." *Atmospheric Environment. Part B. Urban Atmosphere* 25, no. 2 (1991): 155-164.

Konopacki, S. "Demonstration of energy savings of cool roofs." *Lawrence Berkeley National Laboratory* (2010).

Kottek, Markus, Jürgen Grieser, Christoph Beck, Bruno Rudolf, and Franz Rubel. "World map of the Köppen-Geiger climate classification updated." *Meteorologische Zeitschrift* 15, no. 3 (2006): 259-263.

Landsat, NASA "Science Data Users Handbook." *2011-03-11]. http://landsathandbook. gsfc. nasa. gov/inst_cal/prog_sect8_2. html* (7).

Levinson, Ronnen, Hashem Akbari, Steve Konopacki, and Sarah Bretz. "Inclusion of cool roofs in nonresidential Title 24 prescriptive requirements." *Energy Policy* 33, no. 2 (2005): 151-170.

Liang, Shunlin. "Narrowband to broadband conversions of land surface albedo I: Algorithms." *Remote Sensing of Environment* 76, no. 2 (2001): 213-238.

Liang, Shunlin, Chad J. Shuey, Andrew L. Russ, Hongliang Fang, Mingzhen Chen, Charles L. Walthall, Craig ST Daughtry, and Raymond Hunt. "Narrowband to broadband conversions of land surface albedo: II. Validation." *Remote Sensing of Environment* 84, no. 1 (2003): 25-41.

Liu, Lin, and Yuanzhi Zhang. "Urban Heat Island analysis using the Landsat TM data and ASTER data: A case study in Hong Kong." *Remote Sensing* 3, no. 7 (2011): 1535-1552.

NASA LP DAAC, 2015, MODIS MCD43A1 Version 6 Bidirectional reflectance distribution function and Albedo (BRDF/Albedo) Model Parameters. NASA EOSDIS Land Processes DAAC, USGS Earth Resources Observation and Science (EROS) Center, Sioux Falls, South Dakota (https://lpdaac.usgs.gov), accessed August 11, 2017.

Madronich, Sasha, and Siri Flocke. "The role of solar radiation in atmospheric chemistry." In *Environmental photochemistry*, pp. 1-26. Springer Berlin Heidelberg, 1999.

Menon, Surabi, Hashem Akbari, Sarith Mahanama, Igor Sednev, and Ronnen Levinson. "Radiative forcing and temperature response to changes in urban albedos and associated CO2 offsets." *Environmental Research Letters* 5, no. 1 (2010): 014005.

Morris, C. J. G., I. Simmonds, and N. Plummer. "Quantification of the influences of wind and cloud on the nocturnal Urban Heat Island of a large city." *Journal of Applied Meteorology* 40, no. 2 (2001): 169-182.

Oke, Timothy R. *Boundary layer climates*. Routledge, 2002.

Oke, Tim R. "City size and the Urban Heat Island." *Atmospheric Environment (1967)* 7, no. 8 (1973): 769-779.

Oke, Timothy R. "The energetic basis of the Urban Heat Island." *Quarterly Journal of the Royal Meteorological Society* 108, no. 455 (1982): 1-24.

Oke, Timothy Richard. "Urban climates and global environmental change." *Applied Climatology: Principles & Practices. New York, NY: Routledge* (1997): 273-287.

Olmedo, Guillermo Federico, Samuel Ortega-Farías, and Daniel de la Fuente-Sáiz. "water: Tools and Functions to Estimate Actual Evapotranspiration Using Land Surface Energy Balance Models in R."

Peel, Murray C., Brian L. Finlayson, and Thomas A. McMahon. "Updated world map of the Köppen-Geiger climate classification." *Hydrology and earth system sciences discussions* 4, no. 2 (2007): 439-473.

Pinker, R. T., and I. Laszlo. "Modeling surface solar irradiance for satellite applications on a global scale." *Journal of Applied Meteorology* 31, no. 2 (1992): 194-211.

Pomerantz, Melvin, Brian Pon, Hashem Akbari, and Sheng-Chieh Chang. "The effects of pavements' temperatures on air temperatures in large cities." (2000).

Pu, Ruiliang, Peng Gong, Ryo Michishita, and Todashi Sasagawa. "Assessment of multi-resolution and multi-sensor data for urban surface temperature retrieval." *Remote Sensing of Environment* 104, no. 2 (2006): 211-225.

Robine, Jean-Marie, Siu Lan K. Cheung, Sophie Le Roy, Herman Van Oyen, Clare Griffiths, Jean-Pierre Michel, and François Richard Herrmann. "Death toll exceeded 70,000 in Europe during the summer of 2003." *Comptes rendus biologies* 331, no. 2 (2008): 171-178.

Rosenfeld, Arthur H., Hashem Akbari, Joseph J. Romm, and Melvin Pomerantz. "Cool communities: strategies for heat island mitigation and smog reduction." *Energy and Buildings* 28, no. 1 (1998): 51-62.

Roy, David P., M. A. Wulder, Thomas R. Loveland, C. E. Woodcock, R. G. Allen, M. C. Anderson, D. Helder et al. "Landsat-8: Science and product vision for terrestrial global change research." *Remote sensing of Environment* 145 (2014): 154-172.

Sailor, David J., and A. A. Pavlova. "Air conditioning market saturation and long-term response of residential cooling energy demand to climate change." *Energy* 28, no. 9 (2003): 941-951.

Scherba, Adam, David J. Sailor, Todd N. Rosenstiel, and Carl C. Wamser. "Modeling impacts of roof reflectivity, integrated photovoltaic panels and green roof systems on sensible heat flux into the urban environment." *Building and Environment* 46, no. 12 (2011): 2542-2551.

Silva, Bernardo B. da, Alexandra C. Braga, Célia C. Braga, Leidjane MM de Oliveira, Suzana MGL Montenegro, and Bernardo Barbosa Junior. "Procedures for calculation of the albedo with OLI-Landsat 8 images: Application to the Brazilian semi-arid." *Revista Brasileira de Engenharia Agrícola e Ambiental* 20, no. 1 (2016): 3-8.

Sobrino, José A., Juan C. Jiménez-Muñoz, and Leonardo Paolini. "Land surface temperature retrieval from LANDSAT TM 5." *Remote Sensing of environment* 90, no. 4 (2004): 434-440.

Smith, R. B. "The heat budget of the earth's surface deduced from space." *Yale University Center for Earth Observation: New Haven, CT, USA* (2010).

Snyder, William C., Zhengming Wan, Yulin Zhang, and Y-Z. Feng. "Classification-based emissivity for land surface temperature measurement from space." *International Journal of Remote Sensing* 19, no. 14 (1998): 2753-2774.

Stolwijk, Jan AJ. "Mathematical models of thermal regulation." *Annals of the New York Academy of Sciences* 335, no. 1 (1980): 98-106.

Susca, T., S. R. Gaffin, and G. R. Dell'Osso. "Positive effects of vegetation: Urban Heat Island and green roofs." *Environmental Pollution* 159, no. 8 (2011): 2119-2126.

Synnefa, A., M. Santamouris, and H. Akbari. "Estimating the effect of using cool coatings on energy loads and thermal comfort in residential buildings in various climatic conditions." *Energy and Buildings* 39, no. 11 (2007): 1167-1174.

Taha, Haider, Hashem Akbari, Arthur Rosenfeld, and Joe Huang. "Residential cooling loads and the Urban Heat Island—the effects of albedo." *Building and environment* 23, no. 4 (1988): 271-283.

Takebayashi, Hideki, and Masakazu Moriyama. "Surface heat budget on green roof and high reflection roof for mitigation of urban heat island." *Building and Environment* 42, no. 8 (2007): 2971-2979.

Tasumi, Masahiro, Richard G. Allen, and Ricardo Trezza. "At-surface reflectance and albedo from satellite for operational calculation of land surface energy balance." *Journal of hydrologic engineering* 13, no. 2 (2008): 51-63.

Trenberth, Kevin E., John T. Fasullo, and Jeffrey Kiehl. "Earth's global energy budget." *Bulletin of the American Meteorological Society* 90, no. 3 (2009): 311-323.

USGS "Landsat Surface Reflectance Level-2 Science Data Products." https://landsat.usgs.gov/landsat-surface-reflectance-data-products (2017)

Voogt, James A., and Tim R. Oke. "Thermal remote sensing of urban climates." *Remote sensing of environment* 86, no. 3 (2003): 370-384.

Weier, John, and David Herring. "Measuring Vegetation (NDVI & EVI). NASA Earth Observatory." (2000).

Weng, Qihao, Dengsheng Lu, and Jacquelyn Schubring. "Estimation of land surface temperature–vegetation abundance relationship for Urban Heat Island studies." *Remote sensing of Environment* 89, no. 4 (2004): 467-483.

Wong, Eva, H. Akbari, R. Bell, and D. Cole. "Reducing Urban Heat Islands: a compendium of strategies." *Environmental Protection Agency, retrieved May* 12 (2011): 2011.

Xiao, Rong-bo, Zhi-Yun Ouyang, Hua Zheng, Wei-Feng Li, Erich W. Schienke, and Xiao-Ke Wang. "Spatial pattern of impervious surfaces and their impacts on land surface temperature in Beijing, China." *Journal of Environmental Sciences* 19, no. 2 (2007): 250-256.

Appendix

Appendix 1: Maps of Study Area (site of 97 Buildings)

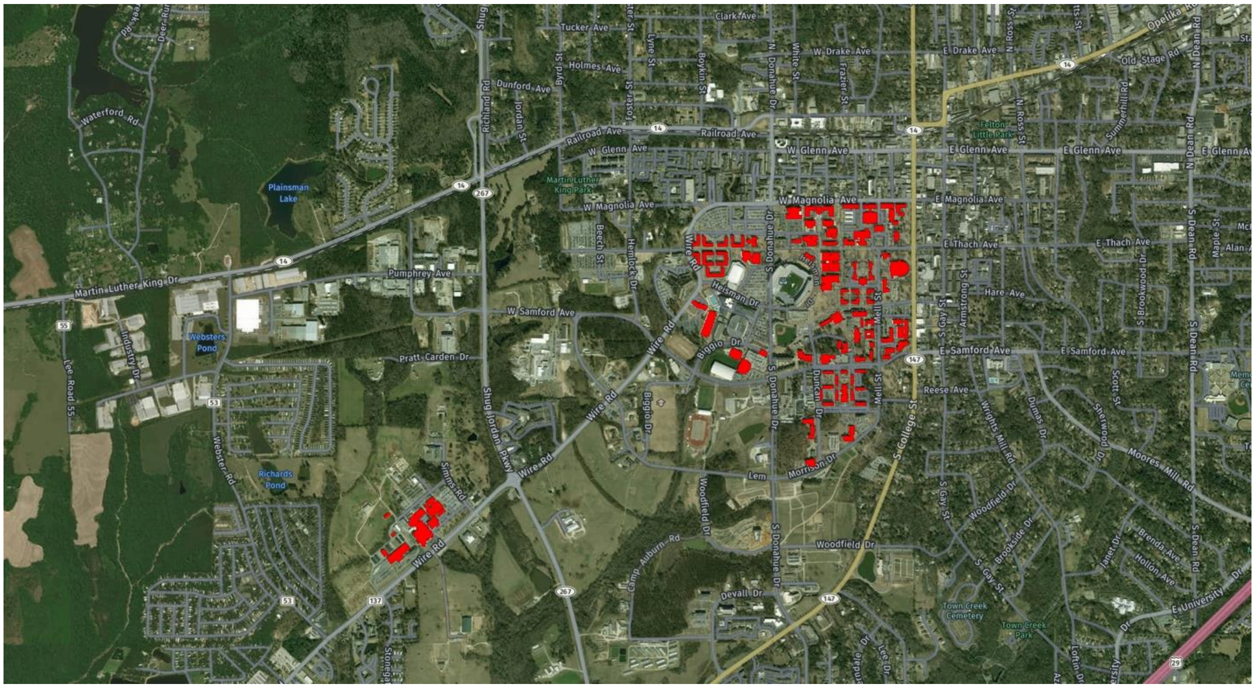

Appendix 2: Earth's Energy Budget (NASA)

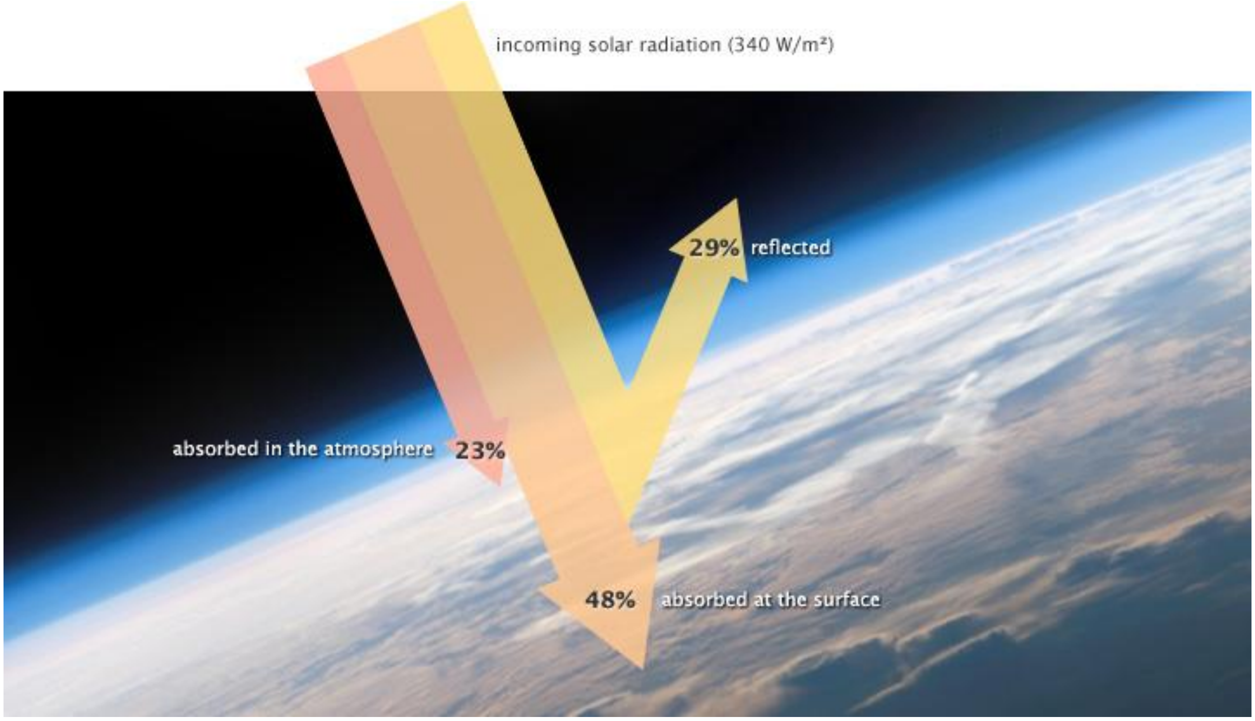

Appendix 3: The angle of the Sun's position to Earth

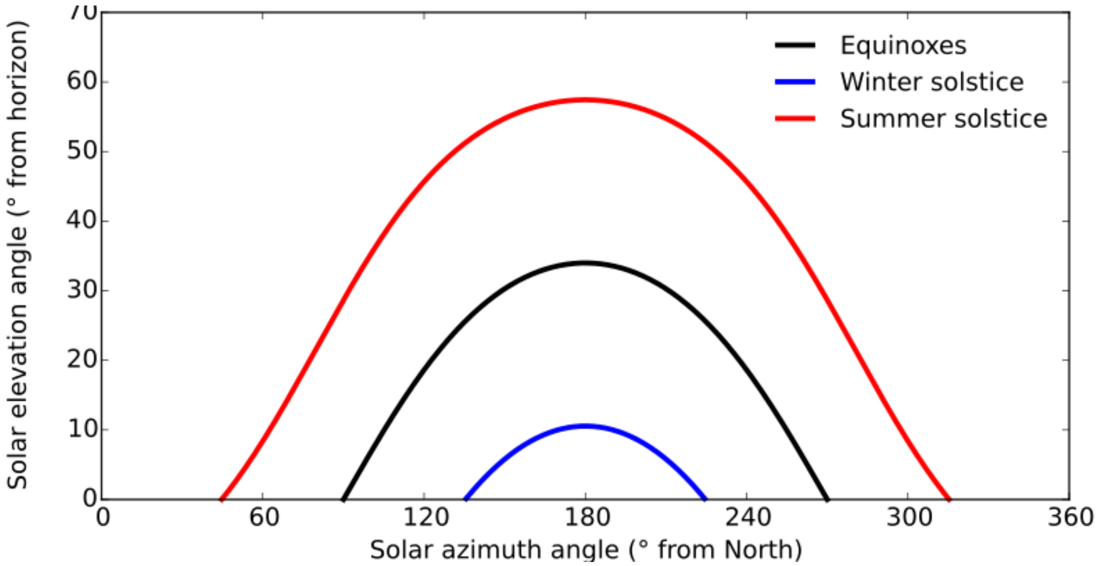

The path of the Sun over the celestial sphere through the course of the day for an observer at 56°N latitude. The Sun's path changes with its declination during the year. The intersections of the lines with the horizontal axis show azimuths in degrees from North where the Sun rises and sets at the summer and winter solstices (Deditos).

Appendix 4: Seasonal Solar Altitude

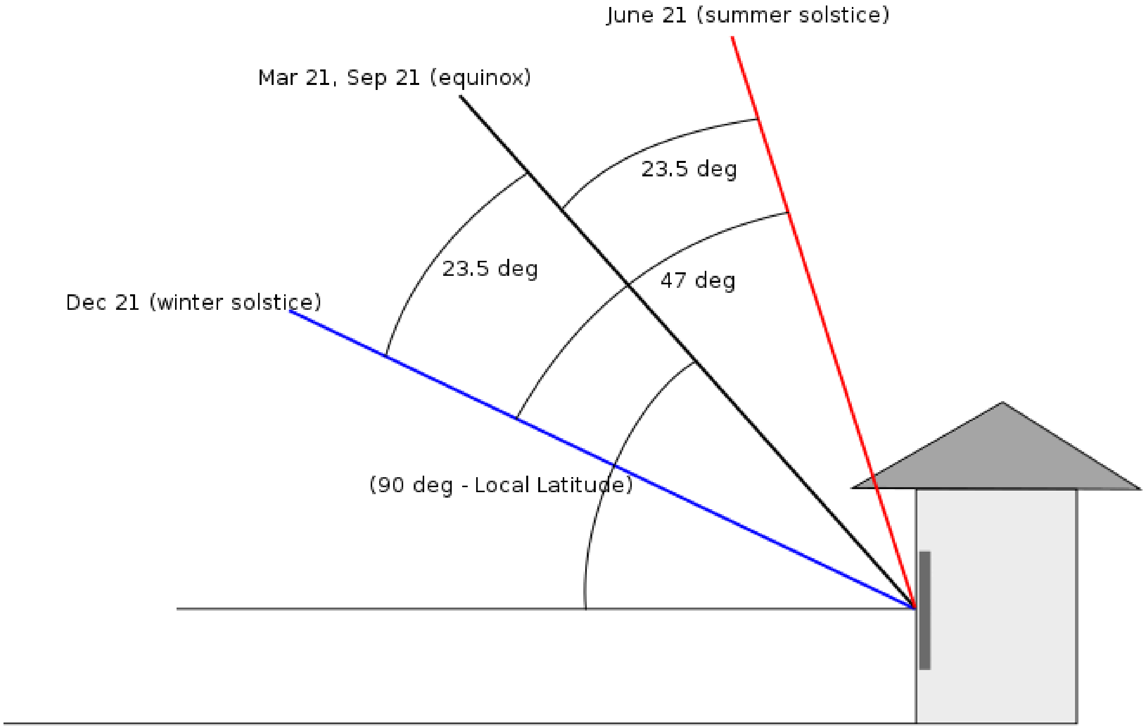

Solar altitude over a year; latitude based on New York, New York (Hartz).

Appendix 5: Spectrum of Solar Radiation on Earth

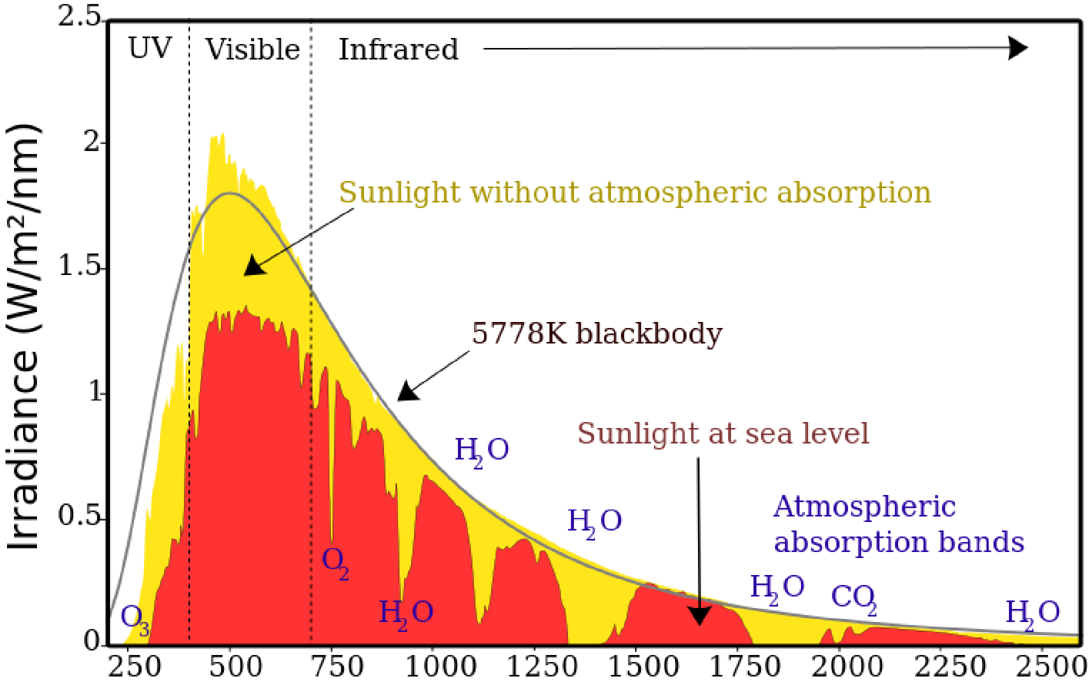

Wavelength (nm) (http://commons.wikimedia.org/wiki/File:Solar_spectrum_ita.svg)

Appendix 6: Radiation spectrum for reflectance and absorption

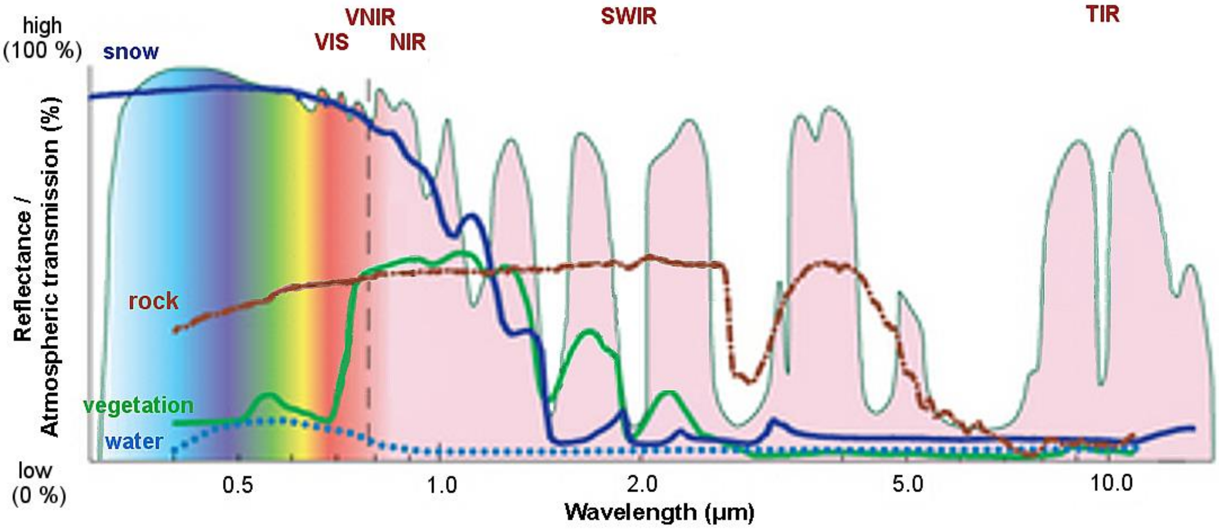

Reflectivity spectra of different surfaces (Andreas Kaab, University of Oslo)

Appendix 7: Sample of Energy Data for Scott-Richie Research Center

Month-CY	FY	Building Code	BUILDING NAME	CONSUMPTION MEASURE	CONSUMPTION (K/GALLONS)	COST PER UNIT	COST THIS PERIOD	SUBTOTAL	COMMENTS	MMBTU	Building Type
Sep-09	FY09	AA_D1401	SCOTT-RITCHEY RESEARCH CENTER & WARE	Metered	12,643.000	$0.50	$6,321.50	$6,321.50			Laboratory
Oct-09	FY10	AA_D1401	SCOTT-RITCHEY RESEARCH CENTER & WARE	Metered	12,558.000	$0.56	$7,032.48	$7,032.48			Laboratory
Nov-09	FY10	AA_D1401	SCOTT-RITCHEY RESEARCH CENTER & WARE	Metered	10,827.000	$0.56	$6,063.12	$6,063.12			Laboratory
Dec-09	FY10	AA_D1401	SCOTT-RITCHEY RESEARCH CENTER & WARE	Metered	5,383.000	$0.56	$3,014.48	$3,014.48			Laboratory
Jan-10	FY10	AA_D1401	SCOTT-RITCHEY RESEARCH CENTER & WARE	Metered	2,367.000	$0.56	$1,325.52	$1,325.52			Laboratory
Feb-10	FY10	AA_D1401	SCOTT-RITCHEY RESEARCH CENTER & WARE	Metered	1,862.000	$0.56	$1,042.72	$1,042.72			Laboratory
Mar-10	FY10	AA_D1401	SCOTT-RITCHEY RESEARCH CENTER & WARE	Metered	3,021.000	$0.56	$1,691.76	$1,691.76			Laboratory
Apr-10	FY10	AA_D1401	SCOTT-RITCHEY RESEARCH CENTER & WARE	Metered	10,765.000	$0.56	$6,028.40	$6,028.40			Laboratory
May-10	FY10	AA_D1401	SCOTT-RITCHEY RESEARCH CENTER & WARE	Metered	11,425.000	$0.56	$6,398.00	$6,398.00			Laboratory
Jun-10	FY10	AA_D1401	SCOTT-RITCHEY RESEARCH CENTER & WARE	Metered	11,980.000	$0.56	$6,708.80	$6,708.80			Laboratory
Jul-10	FY10	AA_D1401	SCOTT-RITCHEY RESEARCH CENTER & WARE	Metered	14,088.000	$0.56	$7,889.28	$7,889.28			Laboratory
Aug-10	FY10	AA_D1401	SCOTT-RITCHEY RESEARCH CENTER & WARE	Metered	14,096.000	$0.56	$7,893.76	$7,893.76			Laboratory
Sep-10	FY10	AA_D1401	SCOTT-RITCHEY RESEARCH CENTER & WARE	Metered	13,560.000	$0.56	$7,593.60	$7,593.60			Laboratory
Oct-10	FY11	AA_D1401	SCOTT-RITCHEY RESEARCH CENTER & WARE	Metered	10,884.000	$0.50	$5,442.00	$5,442.00			Laboratory
Nov-10	FY11	AA_D1401	SCOTT-RITCHEY RESEARCH CENTER & WARE	Metered	11,098.000	$0.50	$5,549.00	$5,549.00			Laboratory
Dec-10	FY11	AA_D1401	SCOTT-RITCHEY RESEARCH CENTER & WARE	Metered	9,201.000	$0.50	$4,600.50	$4,600.50			Laboratory
Jan-11	FY11	AA_D1401	SCOTT-RITCHEY RESEARCH CENTER & WARE	Metered	9,103.000	$0.50	$4,551.50	$4,551.50			Laboratory
Feb-11	FY11	AA_D1401	SCOTT-RITCHEY RESEARCH CENTER & WARE	Metered	8,761.000	$0.50	$4,380.50	$4,380.50			Laboratory
Mar-11	FY11	AA_D1401	SCOTT-RITCHEY RESEARCH CENTER & WARE	Metered	10,169.000	$0.50	$5,084.50	$5,084.50			Laboratory
Apr-11	FY11	AA_D1401	SCOTT-RITCHEY RESEARCH CENTER & WARE	Metered	10,131.000	$0.50	$5,065.50	$5,065.50			Laboratory
May-11	FY11	AA_D1401	SCOTT-RITCHEY RESEARCH CENTER & WARE	Metered	12,048.000	$0.50	$6,024.00	$6,024.00			Laboratory
Jun-11	FY11	AA_D1401	SCOTT-RITCHEY RESEARCH CENTER & WARE	Metered	13,651.000	$0.50	$6,825.50	$6,825.50			Laboratory
Jul-11	FY11	AA_D1401	SCOTT-RITCHEY RESEARCH CENTER & WARE	Metered	14,123.000	$0.50	$7,061.50	$7,061.50			Laboratory
Aug-11	FY11	AA_D1401	SCOTT-RITCHEY RESEARCH CENTER & WARE	Metered	14,018.000	$0.50	$7,009.00	$7,009.00			Laboratory
Sep-11	FY11	AA_D1401	SCOTT-RITCHEY RESEARCH CENTER & WARE	Metered	7,885.000	$0.50	$3,942.50	$3,942.50			Laboratory
Oct-11	FY12	AA_D1401	SCOTT-RITCHEY RESEARCH CENTER & WARE	Metered	6,666.310	$0.47	$3,133.17	$3,133.17			Laboratory
Nov-11	FY12	AA_D1401	SCOTT-RITCHEY RESEARCH CENTER & WARE	Metered	12,253.000	$0.47	$5,758.91	$5,758.91			Laboratory
Dec-11	FY12	AA_D1401	SCOTT-RITCHEY RESEARCH CENTER & WARE	Metered	10,645.000	$0.47	$5,003.15	$5,003.15			Laboratory
Jan-12	FY12	AA_D1401	SCOTT-RITCHEY RESEARCH CENTER & WARE	Metered	9,996.000	$0.47	$4,698.12	$4,698.12		892	Laboratory
Feb-12	FY12	AA_D1401	SCOTT-RITCHEY RESEARCH CENTER & WARE	Metered	10,058.000	$0.47	$4,727.26	$4,727.26		858	Laboratory
Mar-12	FY12	AA_D1401	SCOTT-RITCHEY RESEARCH CENTER & WARE	Metered	13,183.807	$0.47	$6,196.39	$6,196.39		1236	Laboratory
Apr-12	FY12	AA_D1401	SCOTT-RITCHEY RESEARCH CENTER & WARE	Metered	12,564.928	$0.47	$5,905.52	$5,905.52		1234	Laboratory
May-12	FY12	AA_D1401	SCOTT-RITCHEY RESEARCH CENTER & WARE	Metered	14,114.239	$0.47	$6,633.69	$6,633.69		1828	Laboratory
Jun-12	FY12	AA_D1401	SCOTT-RITCHEY RESEARCH CENTER & WARE	Metered	13,657.369	$0.47	$6,418.96	$6,418.96		2375	Laboratory
Jul-12	FY12	AA_D1401	SCOTT-RITCHEY RESEARCH CENTER & WARE	Metered	14,098.056	$0.47	$6,626.09	$6,626.09		2320	Laboratory
Aug-12	FY12	AA_D1401	SCOTT-RITCHEY RESEARCH CENTER & WARE	Metered	14,114.119	$0.47	$6,633.64	$6,633.64		2283	Laboratory
Sep-12	FY12	AA_D1401	SCOTT-RITCHEY RESEARCH CENTER & WARE	Metered	12,529.511	$0.47	$5,888.87	$5,888.87		1784	Laboratory
Oct-12	FY13	AA_D1401	SCOTT-RITCHEY RESEARCH CENTER & WARE	Metered	12,009.453	$0.54	$6,485.10	$6,485.10		1268	Laboratory
Nov-12	FY13	AA_D1401	SCOTT-RITCHEY RESEARCH CENTER & WARE	Metered	9,515.705	$0.54	$5,138.48	$5,138.48		755	Laboratory
Dec-12	FY13	AA_D1401	SCOTT-RITCHEY RESEARCH CENTER & WARE	Metered	10,482.427	$0.54	$5,660.51	$5,660.51		822	Laboratory
Jan-13	FY13	AA_D1401	SCOTT-RITCHEY RESEARCH CENTER & WARE	Metered	10,959.423	$0.54	$5,918.09	$5,918.09		954	Laboratory
Feb-13	FY13	AA_D1401	SCOTT-RITCHEY RESEARCH CENTER & WARE	Metered	9,730.633	$0.54	$5,254.54	$5,254.54		648	Laboratory
Mar-13	FY13	AA_D1401	SCOTT-RITCHEY RESEARCH CENTER & WARE	Metered	10,561.356	$0.54	$5,703.13	$5,703.13		886	Laboratory
Apr-13	FY13	AA_D1401	SCOTT-RITCHEY RESEARCH CENTER & WARE	Metered	10,088.809	$0.54	$5,447.96	$5,447.96		1076	Laboratory
May-13	FY13	AA_D1401	SCOTT-RITCHEY RESEARCH CENTER & WARE	Metered	16,958.167	$0.54	$9,157.41	$9,157.41	Averaged: NIE/NAE Upgrade	1633	Laboratory
Jun-13	FY13	AA_D1401	SCOTT-RITCHEY RESEARCH CENTER & WARE	Metered	19,278.662	$0.54	$10,410.48	$10,410.48		2135	Laboratory
Jul-13	FY13	AA_D1401	SCOTT-RITCHEY RESEARCH CENTER & WARE	Metered	19,574.558	$0.54	$10,570.26	$10,570.26		2203	Laboratory
Aug-13	FY13	AA_D1401	SCOTT-RITCHEY RESEARCH CENTER & WARE	Metered	25,715.011	$0.54	$13,886.11	$13,886.11		2475	Laboratory
Sep-13	FY13	AA_D1401	SCOTT-RITCHEY RESEARCH CENTER & WARE	Metered	20,645.007	$0.54	$11,148.30	$11,148.30		2026	Laboratory
Oct-13	FY14	AA_D1401	SCOTT-RITCHEY RESEARCH CENTER & WARE	Metered	17,147.070	$0.55	$9,430.89	$9,430.89		1454	Laboratory
Nov-13	FY14	AA_D1401	SCOTT-RITCHEY RESEARCH CENTER & WARE	Metered	10,991.570	$0.55	$6,045.36	$6,045.36		789	Laboratory
Dec-13	FY14	AA_D1401	SCOTT-RITCHEY RESEARCH CENTER & WARE	Metered	10,549.144	$0.55	$5,802.03	$5,802.03		767	Laboratory
Jan-14	FY14	AA_D1401	SCOTT-RITCHEY RESEARCH CENTER & WARE	Metered	8,164.514	$0.55	$4,490.48	$4,490.48		438	Laboratory
Feb-14	FY14	AA_D1401	SCOTT-RITCHEY RESEARCH CENTER & WARE	Metered	9,095.056	$0.55	$5,002.28	$5,002.28		610	Laboratory
Mar-14	FY14	AA_D1401	SCOTT-RITCHEY RESEARCH CENTER & WARE	Metered	9,308.316	$0.55	$5,119.57	$5,119.57		660	Laboratory
Apr-14	FY14	AA_D1401	SCOTT-RITCHEY RESEARCH CENTER & WARE	Metered	12,154.612	$0.55	$6,685.04	$6,685.04		1041	Laboratory
May-14	FY14	AA_D1401	SCOTT-RITCHEY RESEARCH CENTER & WARE	Metered	15,691.173	$0.55	$8,630.15	$8,630.15		1473	Laboratory
Jun-14	FY14	AA_D1401	SCOTT-RITCHEY RESEARCH CENTER & WARE	Metered	19,165.316	$0.55	$10,540.92	$10,540.92		1878	Laboratory
Jul-14	FY14	AA_D1401	SCOTT-RITCHEY RESEARCH CENTER & WARE	Metered	22,918.444	$0.55	$12,605.14	$12,605.14		2231	Laboratory
Aug-14	FY14	AA_D1401	SCOTT-RITCHEY RESEARCH CENTER & WARE	Metered	24,184.856	$0.55	$13,301.67	$13,301.67		2378	Laboratory
Sep-14	FY14	AA_D1401	SCOTT-RITCHEY RESEARCH CENTER & WARE	Metered	14,884.043	$0.55	$8,186.22	$8,186.22		689	Laboratory
Oct-14	FY15	AA_D1401	SCOTT-RITCHEY RESEARCH CENTER & WARE	Metered	13,294.682	$0.56	$7,445.02	$7,445.02	Averaged days 2-3 for day 1	1199	Laboratory
Nov-14	FY15	AA_D1401	SCOTT-RITCHEY RESEARCH CENTER & WARE	Metered	8,641.903	$0.56	$4,839.47	$4,839.47		649	Laboratory
Dec-14	FY15	AA_D1401	SCOTT-RITCHEY RESEARCH CENTER & WARE	Metered	9,102.515	$0.56	$5,097.41	$5,097.41		756	Laboratory
Jan-15	FY15	AA_D1401	SCOTT-RITCHEY RESEARCH CENTER & WARE	Metered	7,676.624	$0.56	$4,298.91	$4,298.91		609	Laboratory
Feb-15	FY15	AA_D1401	SCOTT-RITCHEY RESEARCH CENTER & WARE	Metered	7,115.752	$0.56	$3,984.82	$3,984.82		546	Laboratory
Mar-15	FY15	AA_D1401	SCOTT-RITCHEY RESEARCH CENTER & WARE	Metered	11,007.471	$0.56	$6,164.18	$6,164.18		626	Laboratory
Apr-15	FY15	AA_D1401	SCOTT-RITCHEY RESEARCH CENTER & WARE	Metered	13,848.665	$0.56	$7,755.25	$7,755.25		1210	Laboratory
May-15	FY15	AA_D1401	SCOTT-RITCHEY RESEARCH CENTER & WARE	Metered	15,731.489	$0.56	$8,809.63	$8,809.63		1631	Laboratory
Jun-15	FY15	AA_D1401	SCOTT-RITCHEY RESEARCH CENTER & WARE	Metered	14,166.786	$0.56	$7,933.40	$7,933.40		1900	Laboratory
Jul-15	FY15	AA_D1401	SCOTT-RITCHEY RESEARCH CENTER & WARE	Metered	16,155.738	$0.56	$9,047.21	$9,047.21		2103	Laboratory
Aug-15	FY15	AA_D1401	SCOTT-RITCHEY RESEARCH CENTER & WARE	Metered	15,477.766	$0.56	$8,667.55	$8,667.55		1944	Laboratory
Sep-15	FY15	AA_D1401	SCOTT-RITCHEY RESEARCH CENTER & WARE	Metered	13,114.824	$0.56	$7,344.30	$7,344.30		1674	Laboratory
Oct-15	FY16	AA_D1401	SCOTT-RITCHEY RESEARCH CENTER & WARE	Metered	14,150.402	$0.60	$8,490.24	$8,490.24		1886	Laboratory
Nov-15	FY16	AA_D1401	SCOTT-RITCHEY RESEARCH CENTER & WARE	Metered	9,716.393	$0.60	$5,829.84	$5,829.84		213	Laboratory
Dec-15	FY16	AA_D1401	SCOTT-RITCHEY RESEARCH CENTER & WARE	Metered	7,740.078	$0.60	$4,644.05	$4,644.05	Programming error: Averaged days 18-31 for days 1-8	567	Laboratory
Jan-16	FY16	AA_D1401	SCOTT-RITCHEY RESEARCH CENTER & WARE	Metered	3,681.212	$0.60	$2,208.73	$2,208.73		228	Laboratory
Feb-16	FY16	AA_D1401	SCOTT-RITCHEY RESEARCH CENTER & WARE	Metered	4,771.888	$0.60	$2,863.13	$2,863.13		361	Laboratory
Mar-16	FY16	AA_D1401	SCOTT-RITCHEY RESEARCH CENTER & WARE	Metered	7,305.114	$0.60	$4,383.07	$4,383.07		665	Laboratory
Apr-16	FY16	AA_D1401	SCOTT-RITCHEY RESEARCH CENTER & WARE	Metered	7,965.570	$0.60	$4,779.34	$4,779.34		776	Laboratory
May-16	FY16	AA_D1401	SCOTT-RITCHEY RESEARCH CENTER & WARE	Metered	11,280.646	$0.60	$6,768.39	$6,768.39		1198	Laboratory
Jun-16	FY16	AA_D1401	SCOTT-RITCHEY RESEARCH CENTER & WARE	Metered	14,858.996	$0.60	$8,915.40	$8,915.40		1710	Laboratory

Appendix 8: Shapefile Data Sample

OBJECTID	BLDG_NAME	BLDG_NASF	ORIG_YEAR_	Age_year_	GROSS_AREA	Shape_Leng	Shape_Area	Ener_Cool	Ene_Use_Gross_Area	LST_mean	NDVI_mean	LSE_mean	Lian_mean	Log_Lian	LN_Lian	Exp_Lian	Exp_2_Lian	Log_2_Lian	Log_Lian_2	Inverse_Li	Ele_mean	DIR_Solar	DIFF_Solar	Solar_Tota
1	Wellness Kitchen	7682	2014	3	13856	490.65646	11972.65036	141050	10.17970554	93.59229	0.27687	0.95986	0.234859886	-0.629191155	-1.448766173	1.26473155	0.055159166	-2.090127773	0.395881509	0.484623447	196.75566	5.922736088	1.057762021	6.980498108
2	South Donahue Residence Hall	156381	2013	4	272056	2232.79555	53195.59454	580544	2.133913606	93.41065	0.36628	0.95997	0.130716935	-0.883668145	-2.034721099	1.139645142	0.017086917	-2.935482038	0.780869391	0.36154797	217.10298	4.969937571	0.974466723	5.944404293
3	Bailey Small Animal Teaching Hos	118211	2014	3	216943	1838.13631	95692.51164	1017254	4.689038134	98.39188	0.45063	0.97261	0.200021564	-0.698923181	-1.609330099	1.221429097	0.040008626	-2.321772552	0.488493614	0.447237704	200.80683	5.864276551	1.055340978	6.919617529
4	Kinesiology Building	36289	2013	4	63259	866.63725	22293.96699	204602	3.234354005	94.79594	0.32612	0.956	0.192313014	-0.715991325	-1.648630952	1.212049846	0.036984295	-2.378471699	0.512643578	0.438535078	211.49598	6.003005336	1.056374314	7.05937965
5	Recreation & Wellness Center	180612	2013	4	289759	2610.06203	110484.9632	566405	1.95474515	99.1335	0.19182	0.95686	0.148973907	-0.826889791	-1.903984106	1.160642705	0.022193225	-2.746868428	0.683746726	0.385971382	209.95751	6.231766035	1.079832335	7.31159837
6	Equine Research Lab Building	3179	2011	6	5810	335.49028	6004.00362	30577	5.262822719	86.4675	0.63329	0.98716	0.168457783	-0.77350892	-1.781070109	1.183478262	0.028378025	-2.569541014	0.59831605	0.410436088	193.55388	5.752784709	1.0458575	6.798642209
7	Woltosz Engineering Research Lab	42284	2011	6	84315	655.75001	18431.71632	988768	11.7270711	101.10975	0.23274	0.94357	0.152431593	-0.816925011	-1.881039353	1.164662788	0.023235391	-2.713766146	0.667366474	0.390424888	224.75585	5.716841236	1.026890537	6.743731774
8	Wiggins Hall	44155	2011	6	75695	708.70833	21009.02069	510674	6.746469384	99.97133	0.21219	0.94841	0.156768774	-0.804740437	-1.852983335	1.169725112	0.024576449	-2.673289868	0.647607172	0.395940367	222.81505	5.796998027	1.034199178	6.831197205
9	Information Technology Building	34833	2011	6	63948	1152.59844	32203.40357	236217	3.693891912	93.27932	0.40834	0.96562	0.137946742	-0.860288552	-1.980887596	1.147914413	0.019029304	-2.857816711	0.740096393	0.371411823	224.42549	6.057325987	1.049019671	7.106345658
10	Auburn Arena	148512	2010	7	276513	2083.30698	134174.3426	917120	3.316733752	95.83902	0.13741	0.97128	0.300194154	-0.52259777	-1.203325835	1.350120913	0.09011653	-1.736032215	0.273108429	0.547899766	213.07036	6.169906718	1.072428659	7.242335377
11	Village View Dining Facility	19675	2009	8	40245	821.93714	26695.20552	269035	6.684929805	96.20444	0.15663	0.96838	0.196785531	-0.706006837	-1.625640819	1.2174829	0.038724545	-2.345303947	0.498445654	0.443605152	210.70767	6.220694583	1.075638671	7.296333254
12	Aubie Residence Hall	76331	2009	8	107930	1357.27913	26859.50207	345116	3.197591031	94.71168	0.39597	0.96515	0.13853309	-0.858446477	-1.976646062	1.148587688	0.019191417	-2.851697471	0.736930354	0.372200336	217.97042	5.74958475	1.025896285	6.775481035
13	Eagle Residence Hall	37851	2009	8	58215	804.95724	14988.08493	203132	3.489341235	94.99756	0.3778	0.96315	0.145922676	-0.835877214	-1.924678412	1.157106713	0.021293427	-2.776724	0.698690716	0.381998267	214.3761	5.53238969	1.012599372	6.544989062
14	Tiger Residence Hall	38097	2009	8	58213	804.95724	14988.08493	214610	3.68663357	94.48387	0.3777	0.96313	0.138402478	-0.858856134	-1.977589331	1.148437678	0.019155246	-2.853058321	0.737633859	0.372024835	211.61812	5.528789481	1.012577364	6.541366845
15	Talon Residence Hall	41671	2009	8	60772	833.71649	15072.28395	99338	1.634601461	93.05251	0.39991	0.96564	0.144095192	-0.841350511	-1.937281145	1.154994049	0.020763424	-2.794905901	0.707870683	0.379598724	209.79763	5.66944936	1.02265713	6.69210649
16	Plainsman Residence Hall	41678	2009	8	60779	833.71649	15072.28395	219570	3.612596456	93.29993	0.4082	0.96685	0.142187437	-0.847138773	-1.950609111	1.152792705	0.020217267	-2.814134091	0.717644101	0.377077495	209.75544	5.685581848	1.021725612	6.707307459
17	Willow Residence Hall	76821	2009	8	108827	1368.32745	27420.66578	143674	1.320205464	94.34306	0.39434	0.96521	0.136930526	-0.863499724	-1.988281593	1.146748476	0.018749969	-2.868483994	0.745631774	0.370041249	212.62668	5.625944883	1.022034028	6.64797891
18	Oak Residence Hall	76870	2009	8	108868	1368.32745	27420.66578	108868	1	94.71083	0.42963	0.96903	0.142460476	-0.846305609	-1.948690679	1.153107505	0.020294987	-2.811366378	0.716233183	0.377439367	215.06471	5.626797532	1.020681875	6.647479407
19	Magnolia Residence Hall	74365	2009	8	107088	1337.50421	26921.11403	120384	1.12415957	94.85277	0.39071	0.96405	0.140517398	-0.852269901	-1.962423968	1.150869102	0.019745139	-2.831179327	0.726363983	0.374856503	212.34739	5.805140613	1.034406676	6.839547288
20	Hoerlein Hall	25047	1970	47	39412	1155.81779	49335.71495	355215	9.012864102	99.6211	0.2094	0.94859	0.158919654	-0.79882239	-1.839356528	1.172243757	0.025255456	-2.653630541	0.638117211	0.39864728	194.67373	6.195198585	1.085349029	7.280547614
21	Duncan Hall	22191	1928	89	37730	706.36105	12138.27205	171067	4.533978267	93.88405	0.34654	0.95827	0.151048314	-0.820884118	-1.890155533	1.163052848	0.022815593	-2.726918015	0.673850735	0.388649346	215.82046	5.728321175	1.031663315	6.75998449
22	BERL - Biological Eng Rsrch Lab	12380	1949	68	21415	690.467	10533.252	235226	10.98416997	96.67688	0.21279	0.93573	0.14439312	-0.8404535	-1.9352157	1.155338206	0.020849373	-2.791926093	0.706362085	0.379990947	210.69977	5.479026275	1.025902589	6.504928863
23	Dudley Hall	36318	1977	40	56285	677.99298	14539.29389	151466	2.691054455	91.4633	0.25039	0.96721	0.151726248	-0.818939282	-1.885677382	1.163841589	0.023020854	-2.720457407	0.670661547	0.389520536	221.01007	5.961961071	1.043185195	7.005146267
24	Sciences Center Laboratory Bldg	53935	2005	12	106609	727.17283	21335.99193	1128520	10.58559784	93.62516	0.41218	0.96708	0.112024194	-0.950688173	-2.189040415	1.118539922	0.01254942	-3.158117751	0.903808002	0.334700155	223.42382	5.150449762	1.000275074	6.150724836
25	Haley Center	244491	1969	48	429797	2612.01168	95292.79885	1833654	4.266325731	93.53508	0.17037	0.96603	0.290359963	-0.537063268	-1.236633875	1.336908639	0.084308908	-1.784085559	0.288436954	0.538850594	217.50854	5.21908271	1.034265476	6.253348186
26	Beard-Eaves-Memorial Coliseum	196120	1969	48	372165	2142.62037	132227.3737	1028844	2.764483495	104.35729	0.21931	0.94147	0.109338637	-0.961226345	-2.213305452	1.115540049	0.011954938	-3.1931248	0.923956086	0.330663933	213.51927	6.262154304	1.08459518	7.346749484
27	Watson Fieldhouse	29176	1997	20	31860	780.13177	32810.5548	46673	1.464940364	92.68084	0.25747	0.97584	0.231261445	-0.635896765	-1.464206412	1.260188666	0.053481856	-2.112403329	0.404364696	0.480896501	195.83348	6.191968871	1.075981478	7.267950349
28	Dudley Commons	13976	1977	40	23873	582.45962	9661.86558	34294	1.436518242	91.05654	0.38872	0.9631	0.145125609	-0.838255944	-1.93015564	1.156184789	0.021061442	-2.784625971	0.702673027	0.380953553	213.15311	5.265536547	1.03220751	6.297744056
29	Shelby Center for Engineering	98238	2007	10	198765	2091.95379	58504.79789	544323	2.738525394	97.22531	0.39366	0.96339	0.131067002	-0.882506634	-2.03204662	1.140044164	0.017178559	-2.931623581	0.778817959	0.36203177	225.90426	5.647476639	1.017141702	6.664618341
30	Duncan Residence Hall	18285	1962	55	34341	512.58513	8613.9439	123322	3.591101016	91.53704	0.46153	0.97227	0.142358162	-0.846617628	-1.94940913	1.152989532	0.020265846	-2.812402884	0.716761408	0.377303806	219.45623	5.283793254	0.974356982	6.258150237
31	Vaughan Large Animal Hospital	46760	2003	14	82353	1299.6113	67935.88955	644685	7.828312265	98.74887	0.33363	0.95724	0.096443157	-1.015728584	-2.338801495	1.101246981	0.009301282	-3.374177319	1.031704556	0.310552985	195.44307	6.018894708	1.065697085	7.084591794
32	Carson Barn - Beef Receiving	8370	2005	12	9708	394.39411	9132.70827	90199	9.291203131	92.51687	0.45041	0.96771	0.126392479	-0.898278769	-2.068363302	1.134727437	0.015975059	-2.984017478	0.806904746	0.355517199	192.78717	5.930311954	1.059150195	6.989462149
33	Greene Hall	79003	1971	46	124200	2115.77684	73627.07381	916460	7.378904992	98.70535	0.2716	0.95497	0.162231942	-0.789863633	-1.818728228	1.176133004	0.026319203	-2.623870195	0.623884559	0.402780265	199.1213	6.071074185	1.075750366	7.146824551
34	Large Animal Isolation Facility	1600	1997	20	2766	257.85424	3293.08035	42554	15.38467101	92.14633	0.47032	0.96706	0.172010475	-0.764445105	-1.760199903	1.187690274	0.029587603	-2.539431672	0.584376319	0.414741455	191.51259	5.857352742	1.049885189	6.907237931
35	Veterinary Education Center	27964	1987	30	55744	808.70466	28089.15097	65000	1.166044776	100.1482	0.35209	0.95845	0.113497655	-0.945013112	-2.175973104	1.120189262	0.012881718	-3.139265606	0.893049782	0.33689413	202.81246	6.307467452	1.077645676	7.385113129
36	Medical Clinic	25042	2004	13	42861	650.66847	19262.27299	122961	2.868831805	90.51546	0.42665	0.9682	0.135824552	-0.867021717	-1.996391282	1.145480904	0.018448309	-2.880183802	0.751726658	0.368543827	219.10566	6.054001355	1.0531752	7.107176555
37	Forestry and Wildlife Sciences	60368	2005	12	112066	1386.53592	35982.16675	424803	3.790650153	87.41857	0.60181	0.98292	0.115156741	-0.938710633	-2.161461109	1.122049295	0.013261075	-3.118329223	0.881177652	0.339347523	216.02486	5.670077232	1.027895358	6.69797259
38	Sasnett Residence Hall	35556	1967	50	61016	542.2937	9204.9584	218681	3.583994362	92.38484	0.37815	0.96295	0.138817438	-0.857555976	-1.974595608	1.148914332	0.019270281	-2.848739291	0.735402253	0.372582122	224.11872	4.494931335	0.942282967	5.437214302
39	Boyd Residence Hall	35503	1967	50	60598	544.34462	9041.02215	115531	1.906515067	90.97942	0.43654	0.96995	0.127624589	-0.894065645	-2.058662226	1.136126408	0.016288036	-2.970021784	0.799353377	0.357245838	226.85229	4.539401043	0.941247705	5.480648748
40	Dowell Residence Hall	21367	1967	50	34036	496.28137	8724.49605	50676	1.488894112	92.30604	0.44375	0.97064	0.130399223	-0.884724997	-2.037154588	1.139283121	0.017003957	-2.938992822	0.782738319	0.361108326	218.20842	5.262432452	0.970518002	6.232950454
41	Knapp Residence Hall	21234	1967	50	34533	545.12634	8689.4272	44218	1.280456375	91.81858	0.43453	0.96945	0.163668936	-0.78603374	-1.809909573	1.177824316	0.026787521	-2.611147565	0.617849041	0.404560176	219.43025	5.310940746	0.979726648	6.290667394
42	Leischuck Residence Hall	18542	1994	23	31192	471.43039	8127.5877	131342	4.210759169	90.93383	0.469	0.97338	0.134529201	-0.871183438	-2.005973998	1.143998064	0.018098106	-2.894008739	0.758960583	0.366782225	218.34973	5.325208562	0.97752537	6.302733932
43	Terrell Dining Hall	25184	1962	55	32862	1080.33536	31421.747	61882	1.883086848	93.52155	0.3823	0.96233	0.168561852	-0.773240706	-1.780452522	1.183601433	0.028413098	-2.568650024	0.597901189	0.410562848	212.77443	6.14297024	1.07130728	7.21427752
44	M Residence Hall	18096	1994	23	31180	476.31257	8017.6612	154925	4.968729955	90.28585	0.43659	0.96968	0.130238096	-0.88526196	-2.038390993	1.139099567	0.016961962	-2.940776576	0.783688738	0.360885157	219.69685	4.815524042	0.96113202	5.776656061
45	Graves Residence Hall	18159	1965	52	30147	487.57723	8410.34025	84153	2.791422032	92.90484	0.40319	0.96623	0.123532489	-0.908218809	-2.09125109	1.131486765	0.015260276	-3.017037577	0.824861404	0.351471889	219.5157	4.865212277	0.965108126	5.830320403
46	Student Center	91221	2008	9	200425	1637.01751	63006.7057	675403	3.36985406	96.16223	0.15975	0.95302	0.146696014	-0.833581687	-1.919392766	1.158001893	0.02151972	-2.769098425	0.694858429	0.383009156	219.25282	5.927029979	1.04580333	6.972833309
47	Gorrie Center	20676	2006	11	37278	569.89498	12990.79045	64841	1.739390525	92.43205	0.40026	0.96485	0.130553753	-0.88421064	-2.035970239	1.139459187	0.017044282	-2.937284167	0.781828456	0.361322228	224.18252	5.206520727	0.995066163	6.20158689
48	Swingle Hall	16552	1972	45	30243	663.6336	8741.4865	190444	6.297126608	89.33033	0.51984	0.97827	0.146380708	-0.834516156	-1.921544461	1.157636826	0.021427312	-2.772202665	0.696417215	0.382597318	215.28623	5.943549128	1.048661183	6.992210311
49	Chemistry Building	35770	1989	28	72244	741.53207	22310.41107	632123	8.749833896	91.5943	0.43902	0.96983	0.146858044	-0.833102259	-1.918288843	1.15818954	0.021567285	-2.767505801	0.694059375	0.383220621	216.60467	4.815862771	0.981770647	5.797633418
50	Toomer Residence Hall	18730	1962	55	30508	525.2297	8646.1004	57562	1.886783794	94.44923	0.35093	0.9591	0.131081089	-0.88245996	-2.031939149	1.140060224	0.017182252	-2.931468534	0.778735581	0.362051224	219.37894	5.247013452	0.971388231	6.218401682
51	Dobbs Residence Hall	18071	1965	52	30530	534.00631	8797.8889	63810	2.090075336	94.49265	0.31336	0.9536	0.126448783	-0.898085348	-2.067917934	1.134791329	0.015989295	-2.983374949	0.806557292	0.355596376	219.50415	4.824684197	0.961902395	5.786586593
52	Burton Hall	7695	1967	50	14655	428.03907	5990.98745	50463	3.443398158	92.8067	0.41876	0.9681	0.148724264	-0.82761817	-1.905661262	1.160352994	0.022118907	-2.749288052	0.684951836	0.38564785	217.82305	4.881490513	0.966264282	5.847754795
53	Hollifield Residence Hall	18332	1962	55	30479	537.77352	8657.51435	62125	2.038288658	90.84062	0.41163	0.96705	0.11917404	-0.923818338	-2.127170334	1.126565969	0.014202452	-3.068858092	0.853440322	0.345215932	218.74214	4.87674479	0.966238083	5.842982873
54	Peet Theatre	33187	1972	45	61209	1000.2123	31077.51297	152798	2.496332239	90.01722	0.27132	0.97305	0.27085981	-0.567255431	-1.306153898	1.311091256	0.073365037	-1.884381752	0.321778724	0.520441937	216.62038	4.984861723	1.008278765	5.993140488
55	Smith Hall, M.W.	29928	1948	69	50269	1042.74203	22562.39296	326465	6.494360341	90.48971	0.49347	0.97399	0.133883865	-0.873271757	-2.01078253	1.14326004	0.017924889	-2.900945985	0.762603562	0.365901442	213.55219	5.735558401	1.048885662	6.784444063
56	Leach Science Center	35118	1960	57	65773	893.36244	28351.31385	656244	9.977407143	92.47648	0.34962	0.95792	0.160166431	-0.795428501	-1.831541809	1.173706196	0.025653286	-2.642356285	0.6327065	0.400207985	209.89161	6.055363542	1.067583518	7.12294706
57	Rouse Life Sciences Bldg	42236	1992	25	83279	745.68659	22288.087	886320	10.64277909	92.74897	0.35997	0.95856	0.151145603	-0.820604483	-1.889511649	1.163166006	0.022844993	-2.725989086	0.673391717	0.388774489	221.8676	4.78813679	0.988260793	5.776397583
58	Biological Research Facility	6888	1988	29	17427	333.23906	5969.52875	97846	5.61462099	93.9835	0.29325	0.94952	0.141505281	-0.849227351	-1.95541824	1.152006588	0.020023745	-2.821072197	0.721187094	0.376171877	215.99078	5.167831173	0.986653989	6.154485161
59	Upchurch Hall	44448	1930	87	70794	1009.29096	24255.20025	275919	3.897491313	92.33408	0.38988	0.96367	0.1270874	-0.895897506	-2.062880242	1.135516257	0.016151207	-2.976107095	0.802632341	0.356493197	218.71337	5.742849319	1.024028738	6.766878056
60	Corley Building	13453	1939	78	23265	414.38256	7809.13568	62322	2.678787879	96.02146	0.22374	0.93797	0.1276557	-0.893959788	-2.058418482	1.136161755	0.016295978	-2.969670136	0.799164103	0.357289379	215.84692	5.377505471	0.99761081	6.375116281
61	Funchess Hall	86882	1961	56	147343	1582.97955	46346.03507	895420	6.077112588	90.80135	0.14845	0.96669	0.309320811	-0.50959086	-1.173376318	1.362499405	0.095679364	-1.692824195	0.259682845	0.556166172	220.33034	6.231730637	1.070259257	7.301989894
62	Extension Hall	11998	1938	79	19148	392.17995	6392.4689	84015	4.387664508	90.53616	0.69865	0.98979	0.159140351	-0.798219688	-1.837968754	1.172502497	0.025325651	-2.651628407	0.63715467	0.398923992	211.22548	5.690285499	1.018131186	6.708416685
63	Allison Laboratory	24438	1963	54	37510	624.74525	12397.54341	108839	2.901599573	88.82642	0.54397	0.9799	0.163494383	-0.786497164	-1.810976645	1.17761874	0.026730413	-2.612687024	0.618577788	0.404344387	206.08629	6.032134322	1.062194158	7.09432848
64	Parker Hall	55037	1963	54	90251	755.58268	29952.9495	337567	3.740313127	93.79132	0.3622	0.95914	0.141998248	-0.847717014	-1.951940561	1.152574629	0.020163502	-2.816054967	0.718624137	0.376826549	207.25615	6.505437002	1.093873629	7.599310632
65	Comer Hall	26990	1910	107	45625	544.042	11701.17478	213159	4.671978082	92.79554	0.29644	0.95135	0.240919214	-0.618128563	-1.423293614	1.272418237	0.058042068	-2.053378638	0.38208292	0.490835221	226.00132	6.168523808	1.060515046	7.229038854
66	Owen Residence Hall	14402	1956	61	23832	504.99136	8232.73025	234795	9.852089627	89.74337	0.62545	0.98692	0.146116358	-0.835301163	-1.923352005	1.157330844	0.02134999	-2.7748104	0.697728032	0.382251694	210.95993	5.344627086	1.000369848	6.344996934
67	Lupton Residence Hall	14629	1952	65	30510	506.12772	8226.12525	215919	7.07699115	89.98688	0.63612	0.98646	0.133378811	-0.874913158	-2.014561995	1.142682777	0.017789907	-2.9063986	0.765473034	0.365210639	210.84971	5.275865361	0.99975604	6.275621402
68	Glenn Residence Hall	14373	1952	65	25397	500.68296	8314.383	159333	6.273693743	89.55523	0.63448	0.98757	0.146332182	-0.834660152	-1.921876024	1.157580651	0.021413107	-2.772681008	0.696657569	0.382533896	212.26527	5.301992549	0.998287552	6.300280101
69	Lane Residence Hall	14350	1952	65	30461	508.2336	8309.3464	192945	6.334164998	92.78827	0.44086	0.96933	0.126798096	-0.896887267	-2.06515925	1.135187796	0.016077757	-2.979395009	0.804406769	0.356087203	212.39047	5.252906657	0.995110668	6.248017325
70	Keller Residence Hall	14133	1952	65	23896	504.27033	8187.92345	128912	5.394710412	92.62831	0.48359	0.97454	0.145876685	-0.836014114	-1.924993636	1.157053498	0.021280007	-2.777178772	0.698919598	0.381938065	212.4402	5.296394675	0.995214259	6.291608934
71	Dowdell Residence Hall	14249	1952	65	24986	507.23317	8248.5088	131776	5.273993436	90.79662	0.56006	0.98095	0.138817015	-0.857557299	-1.974598653	1.148913847	0.019270164	-2.848743684	0.735404521	0.372581555	213.89352	5.348057289	0.99787381	6.345931099
72	Spidle Hall	34413	1962	55	50843	742.71358	17520.2176	670646	13.1905277	93.10454	0.38389	0.96366	0.173596319	-0.760459487	-1.751022678	1.189575261	0.030135682	-2.526191734	0.578298631	0.416648916	215.78308	6.342740342	1.073927122	7.416667464
73	Quad Center	14006	1939	78	28357	541.62821	14235.67438	120688	4.256021441	93.47416	0.37274	0.96202	0.140327855	-0.852856114	-1.963773773	1.150650984	0.019691907	-2.833126684	0.72736355	0.374603597	214.50114	5.905105081	1.045204977	6.950310058
74	Broun Residence Hall	16216	1938	79	29697	664.87299	8922.43568	66644	2.244132404	91.0169	0.49823	0.97598	0.15578541	-0.807473219	-1.859275798	1.168575411	0.024269094	-2.682367973	0.652013	0.394696605	217.89351	5.265306464	0.987537639	6.252844103
75	Martin Aquatics Center	59317	1969	48	88505	1302.61934	65459.14883	109324	1.235229648	101.28449	0.18863	0.94206	0.172405344	-0.763449277	-1.757906925	1.188159349	0.029723603	-2.536123603	0.582854799	0.415217225	201.84538	6.023666723	1.062184318	7.085851041
76	Student Activities Center	61330	1984	33	101572	1280.84371	73138.30089	389974	3.83938487	93.67188	0.21275	0.97575	0.317726537	-0.497946511	-1.146564214	1.374000471	0.100950152	-1.654142505	0.247950728	0.563672366	199.42757	6.492537985	1.098348653	7.590886639
77	Athletics Complex	60048	1989	28	100190	970.40012	46160.72017	607471	6.063189939	98.4844	0.32988	0.95198	0.1484076	-0.828543857	-1.907792735	1.159985611	0.022024816	-2.752363117	0.686484923	0.38523707	201.45157	5.816134824	1.063088284	6.879223108
78	Walker Building	67854	1975	42	123892	1134.98415	39504.18806	703636	5.679430472	97.71904	0.23913	0.95371	0.145878487	-0.836008749	-1.924981283	1.157055582	0.021280533	-2.777160951	0.698910628	0.381940424	214.3608	5.243379141	1.012778108	6.256157249
79	Gavin Engineering Research Laboratory	34205	1930	87	48950	800.87189	19614.6313	261061	5.333217569	95.66219	0.38714	0.96439	0.125851666	-0.900141031	-2.07265132	1.134113928	0.015838642	-2.990203781	0.810253876	0.354755784	218.28222	5.418045786	1.005910046	6.423955832
80	Harbert Center	28569	1986	31	46445	675.42112	18411.42765	246973	5.317536872	97.1543	0.33109	0.95666	0.14009155	-0.853588059	-1.965459139	1.150379112	0.019625642	-2.835558153	0.728612574	0.374288058	227.08524	5.371829933	0.997586122	6.369416054
81	Foy Hall	70188	1953	64	131929	1803.62691	51697.44825	926894	7.025703219	89.21375	0.10935	0.9772	0.332498659	-0.478210102	-1.101119452	1.394448029	0.110555358	-1.588579573	0.228684902	0.576626967	217.3406	5.96584626	1.055325771	7.02117203
82	Draughon Library	277395	1962	55	395503	1299.23507	82914.69525	1150864	2.909874261	92.76371	0.24507	0.9696	0.150426017	-0.822677044	-1.894283899	1.162329309	0.022627987	-2.732873987	0.676797519	0.38784793	227.57669	6.119664175	1.062164902	7.181829077
83	Teague Residence Hall	14563	1938	79	24036	667.76277	8416.79117	73434	3.055167249	91.68939	0.49323	0.97545	0.142856271	-0.84510069	-1.945916251	1.153563989	0.020407914	-2.807363725	0.714195176	0.37796332	217.73054	5.35485163	0.992840833	6.347692464
84	Harper Residence Hall	11391	1938	79	21813	633.35435	7787.95495	48052	2.202906524	90.03286	0.48987	0.97525	0.156505114	-0.805471467	-1.854666593	1.169416743	0.024493851	-2.675718297	0.648784285	0.395607272	220.92816	5.113804811	0.983110665	6.096915476
85	Little Residence Hall	16835	1938	79	27296	633.44243	8270.03695	49494	1.813232708	89.87088	0.5594	0.98163	0.134846428	-0.870160554	-2.003618719	1.144361029	0.018183559	-2.89061079	0.757179389	0.367214417	221.11899	5.209627978	0.982589739	6.192217716
86	Hotel/Dixon Conference Center	111502	1988	29	172536	1340.64954	59196.7879	337928	1.958594148	95.18195	0.16768	0.95939	0.173075537	-0.761764313	-1.754027152	1.188955911	0.029955141	-2.530526274	0.580284869	0.416023481	219.92728	5.795379439	1.061410774	6.856790213
87	Martin Hall	23864	1910	107	40698	535.79021	10922.05715	106356	2.613297951	92.78137	0.32318	0.95589	0.201904246	-0.694854549	-1.599961726	1.223730825	0.040765324	-2.308256847	0.482822844	0.449337563	225.35253	6.191926016	1.064098913	7.256024929
88	Petrie Hall	13239	1939	78	21697	613.93689	11317.4947	107558	4.957275199	92.12261	0.45436	0.97107	0.127186499	-0.895558986	-2.06210077	1.135628792	0.016176406	-2.974982555	0.802025897	0.356632163	206.25733	5.345891897	1.005358123	6.351250021
89	Tichenor Hall	22223	1940	77	41757	597.93524	14130.61155	103008	2.466843882	92.27968	0.42801	0.96852	0.118509015	-0.926248613	-2.132766248	1.125817023	0.014044387	-3.076931289	0.857936492	0.344251383	219.12326	5.444958812	1.005270646	6.450229458
90	Thach Hall	25218	1951	66	42871	746.38206	14528.81435	120131	2.802150638	94.85946	0.39985	0.96584	0.143634165	-0.842742247	-1.940485736	1.154461688	0.020630773	-2.799529148	0.710214495	0.378990982	211.93117	5.657079126	1.029429727	6.686508853
91	Miller Hall	14067	1952	65	25240	511.66448	11107.5815	90798	3.597385103	91.9165	0.55993	0.98188	0.141511727	-0.849207569	-1.95537269	1.152014014	0.020025569	-2.821006482	0.721153496	0.376180445	213.49037	5.726893272	1.034522034	6.761415306
92	Broun Hall	60742	1983	34	101458	1030.15158	28967.9003	627582	6.185633464	99.26911	0.22354	0.94983	0.114500451	-0.941192801	-2.167176514	1.121313147	0.013110353	-3.12657481	0.885843889	0.338379153	214.53487	5.975985537	1.062767534	7.038753071
93	Samford Hall	40925	1888	129	63973	538.50973	13320.72785	587547	9.1842965	90.69337	0.42742	0.96912	0.134406759	-0.871578893	-2.006884566	1.143857999	0.018065177	-2.895322411	0.759649766	0.366615273	237.07881	4.560990492	0.94270697	5.503697462
94	Ross Hall	31403	1930	87	62212	576.69491	17830.49843	139273	2.238683855	95.68438	0.29125	0.95016	0.159818826	-0.796372064	-1.833714443	1.17329828	0.025542057	-2.645490734	0.634208465	0.399773468	224.44617	5.805445903	1.033482852	6.838928755
95	Wilmore Laboratories	46054	1949	68	83094	1112.21513	52863.03322	1292204	15.55111079	100.05541	0.2292	0.93804	0.140176794	-0.853323876	-1.964850836	1.150477179	0.019649534	-2.834680557	0.728161637	0.374401916	216.19128	5.367124631	1.026898103	6.394022734
96	Langdon Hall	7565	1846	171	12159	356.10028	6265.40295	26832	2.206760424	98.65654	0.19166	0.92957	0.153883172	-0.812808869	-1.871561585	1.166354616	0.023680031	-2.700092617	0.660658257	0.392279457	224.78387	4.714235282	0.957278026	5.671513308
97	Davis Hall	36011	1992	25	73190	634.42809	19861.56165	123991	1.694097554	99.18773	0.21889	0.93673	0.158755733	-0.799270581	-1.840388526	1.172051619	0.025203383	-2.6551194	0.638833462	0.398441631	225.98435	4.797303893	0.973234376	5.770538269
98	Hargis Hall	4928	1888	129	11203	347.80011	5321.32985	32602	2.910113362	92.8626	0.46372	0.9726	0.156485317	-0.805526405	-1.854793092	1.169393592	0.024487655	-2.675900796	0.648872789	0.395582251	226.68205	4.348083915	0.930293408	5.278377322
99	Biggin Hall	33643	1951	66	53596	662.42391	15796.6378	192380	3.589446974	95.12201	0.395	0.96421	0.144032057	-0.841540836	-1.937719384	1.154921132	0.020745234	-2.795538145	0.708190978	0.379515556	226.75068	6.072241259	1.045407336	7.117648595
100	Lowder Hall	106203	1992	25	160566	1192.088	51005.9902	554780	3.455152398	97.5786	0.29641	0.96179	0.129326486	-0.888312523	-2.045415174	1.138061625	0.01672534	-2.950910327	0.789099139	0.359619919	223.22165	5.829063461	1.036912519	6.86597598
101	Ramsay Hall	29828	1925	92	47964	682.98799	14961.5121	190804	3.978066884	95.10681	0.46008	0.97248	0.109704702	-0.959774758	-2.209963049	1.115948485	0.012035122	-3.188302732	0.921167585	0.331217002	226.75029	5.290144321	0.992495328	6.282639649
102	Wallace Hall	27753	1984	33	47012	660.50803	25928.6791	81033	1.723666298	94.62066	0.20647	0.97366	0.179606214	-0.745678642	-1.716988524	1.196746009	0.032258392	-2.477090829	0.556036637	0.423799733	207.50902	6.274248411	1.084209165	7.358457576
103	Nichols Center	21757	1986	31	33709	891.31788	18069.79445	123079	3.651220742	94.24308	0.40943	0.96684	0.15086209	-0.82141988	-1.891389171	1.16283628	0.02275937	-2.728697778	0.67473062	0.388409693	210.65263	6.086489538	1.065858715	7.152348253